RWR-501-66-92094-ek
UNCLASSIFIED REPORT 013/92

E.J.A. Konings

Modelling of Three Phase Brushless DC Motors
A Survey of Literature

Supervised by: ir. H. Huisman
Delft University of Technology
Department of Mechanical Engineering and Marine Technology
Systems and Control Group

dr. ir. M. Steinbuch
Philips Research Laboratories
Eindhoven

© *Philips Electronics N.V. 1992*
All rights are reserved. Reproduction in whole or in part is prohibited without the written consent of the copyright owner.

NAT. LAB. Unclassified Report 013/92

E.J.A. Konings

Modelling of Three Phase Brushless DC Motors

ABSTRACT

In permanent magnet brushless DC motors (PM BDCM) the classical mechanical commutator is replaced by electronic components. Brushless DC motors are available in many different designs. The output range of these motors reaches from a few μW up to motors with a mechanical power of several kW. The speed of a PM BDCM varies from several rpm up to more than 100,000 rpm.

In general a PM BDCM consists of a rotor containing permanent magnets and a stator with wound coils. A phase is the connection of one or more coils in series. The motor is controlled by an inverter that converts a direct voltage into an alternating voltage which is fed to the phases. The torque produced by a PM BDCM can be calculated as the product of the stator phase currents and induced phase voltages divided by the rotor angular speed. This results in a static description of the torque production. The dynamic behavior of a PM BDCM can be modelled with the help of state-space models. Although the models proposed in literature look very attractive, a major problem is the determination of the motor parameters.

This literature survey tries to give a view on the modelling of a PM BDCM. The modelling of parasitic effects like magnetic saturation and iron losses will be discussed extensively. Also the effects of changes in mechanical, electrical and magnetic parameters will be treated.

Keywords:
brushless DC motors, commutation, iron losses, saturation, asymmetry

Contents

1 Introduction **1**
- 1.1 The Permanent Magnet Brushless DC Motor 1
- 1.2 Scope of Report 2
- 1.3 Problem Formulation 2
- 1.4 Report Outline 2

2 Introduction into the Modelling of Brushless DC Motors **3**
- 2.1 Classification of Brushless DC Motors 3
- 2.2 Mathematical Model of the BDCM with Uniform Airgap 6
- 2.3 Waveforms and Torque Production in Permanent Magnet Motors 9
- 2.4 Phase Circuits 14
- 2.5 Commutation Strategies 20
- 2.6 The Back–EMF Sensing Principle 22

3 Accurate Modelling of Brushless DC Motors **25**
- 3.1 Modelling of a BDCM with Non–Uniform Airgaps 25
- 3.2 Modelling of a BDCM with Magnetic Saturation 28
- 3.3 A BDCM Model with Saturation in Rotating Frame 29
- 3.4 Modelling of a BDCM with Iron Losses 30

4 Damping Circuits **33**
- 4.1 What are Snubbers? 33
- 4.2 Snubber Circuits, assuming Snap–off 33
- 4.3 Snubber Circuits, assuming Soft Recovery 37

5 Influence of Changes in Parameters on Performance **39**
- 5.1 Summary of Steps in Performance Determination 39
- 5.2 The Spindle DC Motor with a Radial Airgap. 42
  - 5.2.1 Influence of the Axial Dimension and Motor Asymmetrics 42
  - 5.2.2 The Symmetric Motor 42
  - 5.2.3 The Real Motor 44
  - 5.2.4 Important Magnetic Changes 50
- 5.3 The Spindle DC Motor with an Axial Airgap. 53
  - 5.3.1 The Symmetric Motor 53
  - 5.3.2 The Real Motor 56

6 Conclusions **65**
6.1 Conclusions 65

A Torque and Inductance Determination **67**
A.1 A summary of steps in performance determination 68
A.2 The equivalent magnetic circuit 69
A.2.1 The permeance of the saturable parts 70
A.2.2 The permeance of the airgap 71
A.2.3 The permanent magnet equivalent scheme 74
A.3 Equations of flux 78
A.4 Determination of the motor torque 78
A.5 Determination of the inductances 79

B Spindle DC motor **81**
B.1 Spindle DC motor with radial gap 81
B.2 Spindle DC motor with axial gap 82

Lab. for Measurement and Control
Mekelweg 2
2628 CD Delft

013/92

Assignment for: E.J.A. Konings
Emmastraat 124
3134 CN Vlaardingen

Title: Modeling of three-phase brushless motor drive systems.
Type: Final year literature survey
Supervisor: ir. H. Huisman
dr. ir. M. Steinbuch (Philips research)
Period: sept 1 - dec 1, 1991

The rapidly growing market for brushless drives for applications such as machine tools, computer disc drives and video cassette recorders is dominated by three-phase, trapezoidal-emf permanent magnet motors.
In many consumer electronic applications these motors are used for very precise position (servo) control. However, due to fabrication tolerances of several components of the drive systems, the position accuracy which can be obtained with a brushless-dc drive system often falls short of its theoretical value.

Therefore, the present assignment is directed towards the analysis of the dynamic behaviour of this class of drive systems, and in particular towards an assessment of the importance of various production tolerances for the attainable precision of position control.

The following issues deserve particular attention:

- (i) Modeling of the influence of geometrical asymmetry of the motor poles and magnets;
- (ii) Modeling of the internal operation of the integrated circuits used for motor-control;
- (iii) Modeling of the influence of external snubber circuits.

In view of the limited duration of this assignment it must be recommended to restrict the results to a number of well-chosen issues in the above field. The references [1, 2] cover some recent research in this area.

prof.ir.O.H.Bosgra

References

[1] T.M. Hijazi and N.A. Demerdash. Computer-aided modeling and experimental verification of the performance of power conditioner operated permanent magnet brushless DC motors including rotor damping effects. *IEEE Trans. Energy Convers. (USA) vol.3, no.3 714-21*, 1988.

[2] P. Pillay and R. Krishnan. Modeling, simulation, and analysis of permanent-magnet motor drives. II. The brushless DC motor drive. In *IEEE Trans. Ind. Appl. (USA) vol.25, no.2 274-9*, 1987.

List of Figures

1.1 The elements of a PM BDCM [15] 1

2.1 Three phase motor power circuits and resulting torque [19] 4
2.2 A star–connected BDCM 6
2.3 Back–EMF and currents of a brushless DC motor [20] 9
2.4 A trapezoidal shaped phase current $i_j(t)$. 12
2.5 Flux linkage gradient, current and total torque when the current is rectangular 12
2.6 Flux linkage gradient, current and total torque when the current is trapezoidal 13
2.7 The two phase interconnections 14
2.8 Flux linkage gradient, phase current, phase torque and total torque 15
2.9 Current source 18
2.10 Voltage source 19
2.11 The controller configuration, torque function and the logic sequence for a three phase, full-wave BDCM. 21
2.12 The six states of the power outputs (one cycle) 22
2.13 The **CAP-DC** and **CAP-CD** voltage waveforms in normal running mode 23
2.14 Typical **CAP-TI** and motor voltage waveforms in normal running mode . . 23

3.1 A three phase two pole BDCM with stationary and rotating frames. [11] . 25
3.2 A model of a BDCM with Iron Losses (i_{i1}, i_{i2} and i_{i3} in the figure). 31

4.1 An R_s-C_s snubber in a step down converter 34
4.2 The equivalent circuit for snubber analysis after diode recovery. 34
4.3 The maximum diode voltage as a function of C_s when $R_s = 0$. 35
4.4 The diode voltage waveforms for $C_s = C_{base}$ and a set of R_s. 36
4.5 $-\frac{v_{Dmax}}{V_d}$ as a function of R_s for snap-off and soft recovery with $\tau = 0.5t_{rr}$. . 36
4.6 Recovery of the diode current 37
4.7 For $C_s = C_{base}$ 38
4.8 The simulated waveforms for the diode current {1}, the diode voltage {2}, the snubber current {3} and the current in the leakage inductance {4} . . 38

5.1 Configuration of a spindle DC motor with radial airgap. 39
5.2 Configuration of a spindle DC motor with axial airgap. 40
5.3 The permanent magnet MMF distribution. 43
5.4 The detent torque of the symmetric motor. 44
5.5 Total torque and torque components. 44

5.6 The magnetizer flux line distribution. 45
5.7 The inside permanent magnet surface radial induction after magnetization, curves for two different permanent magnet rings that have been magnetized by different magnetizers. 45
5.8 The detent torque T_d including the effect of the gradient between two consecutive poles. 46
5.9 The total torque including the effect of the gradient between two consecutive poles. 46
5.10 The stator lamination. 47
5.11 The detent torque including the effect of three larger slot openings. 48
5.12 The radial attractive force. 48
5.13 Total torque and torque components with the influence of three larger slot openings. 49
5.14 The detent torque when varying permanent magnet pole pitches are used. . 50
5.15 A typical motor with varying pole pitches. 51
5.16 The detent torque when varying permanent magnet magnetization levels are present. 52
5.17 The motor configuration (top view) of the spindle DC motor with an axial airgap. 53
5.18 The permanent magnet MMF distribution. 54
5.19 The permanent magnet axial induction after magnetization. 54
5.20 Simulated torque (nominal). 55
5.21 Measured torque, two phases on mode, $0.74A/phase$. 55
5.22 Top view several coil surfaces, all coils same total surface. 57
5.23 Simulated results for the torque for several coil surfaces. 57
5.24 Top view motor, one coil with bigger surface ($R_a = 1.17$ [p.u.]). 58
5.25 Simulated torque for a motor with one coil with a bigger surface. 58
5.26 Top view motor, one coil with 5% eccentricity. 59
5.27 Simulated torque for a motor with one coil with 5% eccentricity. 60
5.28 Permanent magnet MMF distribution in case of variation in pole pitches. . 61
5.29 Simulated torque for a motor with a variation in permanent magnet pole pitches 62
5.30 Torque for several levels of magnetisation 63

A.1 The equivalent magnetic scheme for a spindle DC motor 68
A.2 The oriented graph for a spindle DC motor 69
A.3 A spindle DC motor 70
A.4 The MMF in the airgap 71
A.5 The approximation of the permanent magnet MMF function 72
A.6 The permeance function 73
A.7 The equivalent magnetic circuit for the permanent magnet and the airgap. 77

Chapter 1

Introduction

1.1 The Permanent Magnet Brushless DC Motor

In this report the results are presented of a literature survey on the modelling of permanent magnet brushless DC motors (PM BDCM).

In general a PM BDCM consists of a stator with coils and a rotor with permanent magnets, see Fig. 1.1. In a PM BDCM currents flow through the coils on the stator. A group of coils connected in series is called a phase. The phase currents are commutated (switched) by an inverter. The inverter changes the direct current (DC) into an alternating current (AC). The commutation of the phase currents is necessary to produce a more or less constant torque. The torque produced by a PM BDCM can be calculated as the product of the stator phase currents and induced phase voltages divided by the rotor angular speed. The induced phase voltages are due to the presence of the permanent magnets on the rotor and are better known as the back electromotive force (back–EMF).

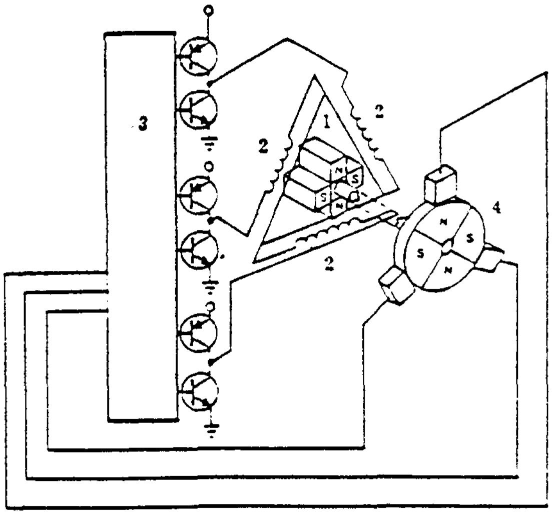

Fig. 1.1: The elements of a PM BDCM [15]
1: rotor with permanent magnets 2: stator phases
3: inverter (logic and transistors) 4: tacho

The lifetime cycle of brushless DC motors as used for instance in hard disk systems has decreased considerably. This means that there is a high pressure on designers to guarantee good design and quality. Therefore, there is an enormous need of computation methods to determine motor performance.

1.2 Scope of Report

In this literature survey the emphasis is put on the dynamic modelling of a PM BDCM including parasitic effects like magnetic saturation and iron losses. Also the influence of asymmetry on motor performance is discussed. It may be important to include the influence of these effects in order to give a detailed description of dynamical characteristics of a certain motor type.

1.3 Problem Formulation

1. What is the working principle of a permanent magnet brushless DC motor?
2. How is a PM BDCM usually modelled in literature?
3. How can a PM BDCM be modelled when parasitic effects like saturation and iron losses are to be included in the model?
4. What are the effects of changes in mechanical, electrical and magnetic parameters on the performance of a PM BDCM?

The first question is answered by giving a very general description of a PM BDCM. The working principle of a PM BDCM will be explained including commutation (switching) strategies and a rotor position sensing method. Extended models for brushless motors are included in this survey. It should be noted that only very little was found on the subject of effects of changes in mechanical, electrical and magnetic parameters on the performance of a PM BDCM.

1.4 Report Outline

Chapter 2 will give a classification by which a PM BCDM can be characterized. A simple model for a PM BDCM will be presented. Also the commutation (switching) of the phases and a position sensing method based on the back electromotive force sensing principle will be discussed.
Chapter 3 presents some accurate methods for modelling PM BDCM. These models are able to describe non–uniformity of the airgap, the presence of magnetic saturation and iron losses.
Chapter 4 describes the design of snubber circuits. Snubbers are needed to protect the diodes of the inverter from overvoltages caused by the switching in the inverter.
Chapter 5 discusses the influence of changes in parameters on the performance of two different types of BDCMs: the BDCM with a radial airgap and the BDCM with an axial airgap. The method used in this chapter to determine the performance is extensively eludicated in the first appendix.
Chapter 6 will give some conclusions, following this literature survey.

Chapter 2

Introduction into the Modelling of Brushless DC Motors

2.1 Classification of Brushless DC Motors

A classification for permanent magnet motor drives can be based on five principal design and performance characteristics [8], namely:

- motor design
- power circuit configuration
- commutation control method
- current regulation
- principal motor control method.

These items will now be described more detailed.

Motor Design
The designer has control over design variables like magnet material and configuration, waveform of the back–EMF, number of poles and presence of dampers on the rotor.

The choice of the magnet material depends on performance and economical considerations. Widely used are ferrites and rare earth/cobalt alloys. Magnet configuration involves the location of magnets, either on the surface or in the interior of the rotor, and the direction of magnetisation.

Usually the stator of a BDCM is wound with three phase windings which can be connected in a delta as well as a star–connection.

An important characteristic of a brushless motor is the waveform of the back–EMF. The possible waveforms will be described in the next section. The number of poles depends on the required airgap flux densities. Higher numbers of poles wil result in a higher airgap flux density. On the other hand a high number of polepairs will also result in higher iron losses, so this is a reason not to apply too many poles. Surface magnet motors, as most BDCMs are, do not have dampers, and the magnets themselves offer negligible paths for the flow of harmonic currents.

Power Circuit

The power circuit can be classified according to the switching device, the duration of gating, the topology of the circuit, and the DC link control methods. The most common power circuit in use is the three phase transistor bridge voltage source inverter. The gating duration is the portion of the electrical cycle during which a particular switch is turned on. The PM drives which employ a trapezoidal back-EMF, see Section 2.2, turn on each device for only 120°. The circuit topology can be a conventional full bridge or a half bridge circuit. According to [19] the full bridge circuit does not only deliver an even torque output but the exploitation of the material used is at its optimum. Both circuits are shown in Fig. 2.1.

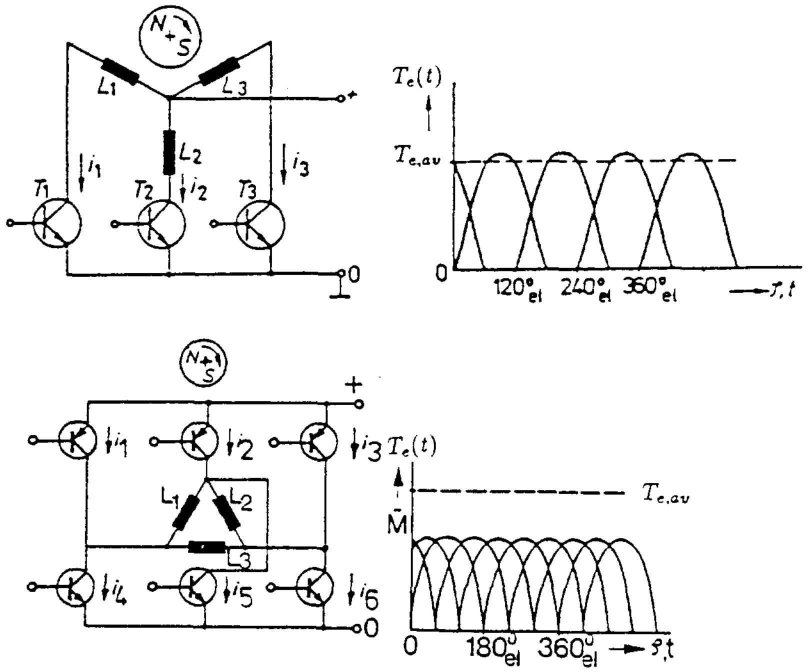

Fig. 2.1: Three phase motor power circuits and resulting torque [19]
a: three pulse, half bridge
b: six pulse, full bridge (delta)

Brushless motors with more than four phases and more than six current pulses hardly offer any technical advantages. The costs of the system increase in a linear manner with the number of pulses, only achieving minor technical improvements.

Commutation Control

The switching (commutation) of the voltage (or current) from one phase to another should be determined for proper functioning by the position of the rotor relative to the conducting phases. This position can be detected either directly or indirectly. If the commutation timing is based on the rotor position then it is a brushless motor. If the commutation is based on external command pulses then it is a **step motor**, see reference [25].

Direct Position Sensing: this sensing method requires the mounting of a position detector on the shaft of the rotor. A high degree of precision can be obtained when a resolver or an incremental optical encoder with a large number of pulses per revolution is used. If

continuous position information is not required an encoder that produces only six pulses per electrical cycle is sufficient for the control of a BDCM.
Indirect Position Sensing: the indirect sensing of the rotor position can be accomplished by measuring the motor voltages. These voltages are used to determine the appropriate commutation signals for the inverter. The principle behind this is that when a phase current is zero, the voltage across the phase is caused solely by the motor back–EMF.

Current Regulation

The current regulation is an essential function in adjustable speed motor drives. Current regulation can be used either to achieve control of the motor torque or just to protect the switching devices from overload. According to [8] there are three categories of current regulation schemes:

- device protection
- DC link current control
- motor current waveform control

Device Protection: in most common three phase transistor bridges the phases are conducting for 120°. A single sensing resistor in the DC link can be used to control all the transistor currents. When a current through this sensing transistor exceeds a threshold value the drive will be briefly removed from the active transistor to prevent overload.
DC Link Current Control: this method is a straightforward way to control the motor current amplitude.
Motor Current Waveform Control: regulation of the current waveform is necessary when a good control of the instantaneous torque is desired. The current regulated pulse width modulation (PWM) inverter is normally used in these cases. The commanded currents are directly derived from the rotor position or from other flux information to ensure a proper phase relation between the current and the back–EMF.

Motor Control Methods

The mechanical performance of a drive, i.e. the shaft speed and torque, is controlled electrically by controlling the voltage and current supplied to the motor. The frequency of the inverter bridge is governed by the motor speed, so the inverter frequency is not a control option. The magnitude of the current and voltage can easily be controlled by the power supply. When the inverter switching signals are derived from the rotor positon, it is possible to control the phase angle between either the voltage or current and the internal back–EMF.

High performance servo drives translate a speed or position into a torque command and control the current directly by PWM of the inverter transistors.

2.2 Mathematical Model of the BDCM with Uniform Airgap

The brushless DC motor has a permanent magnet rotor, a positioning sensor mounted on the rotor, and an inverter to provide three phase signals to the phases of the motor. The signals from the inverter are synchronised with the output of the position sensor to provide the electronic commutation. The phases should be wound such that a trapezoidal back electromotive force (back–EMF) is produced.

In Fig. 2.2 a star–connected three phase BDCM is shown.

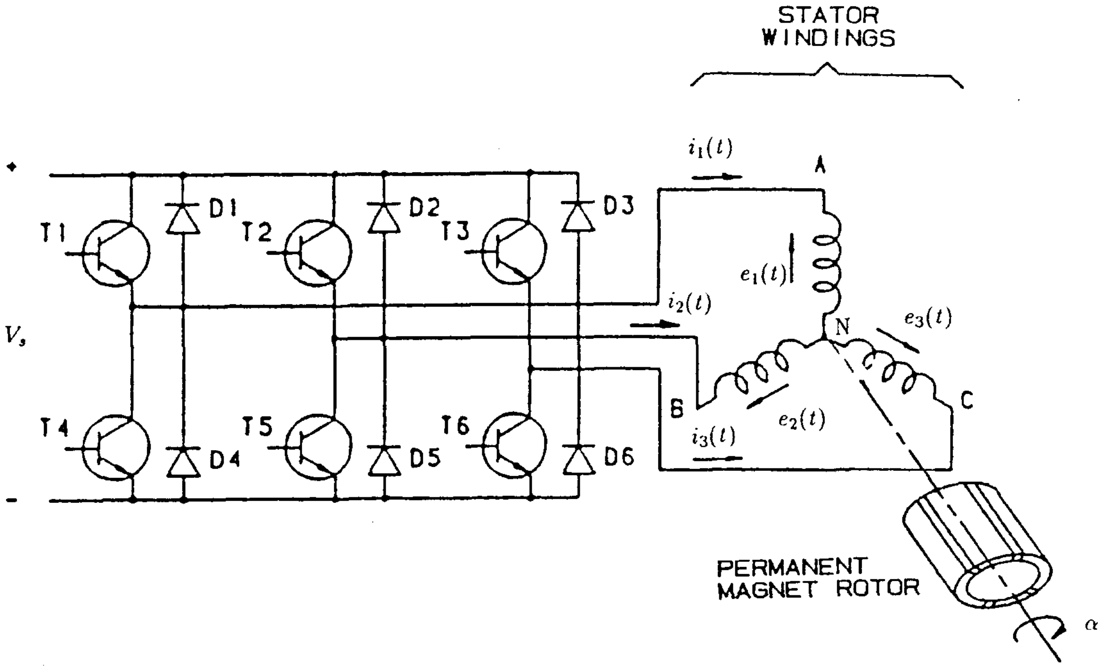
STATOR
WINDINGS
+
-
V_s
T1
T2
T3
T4
T5
T6
D1
D2
D3
D4
D5
D6
$i_1(t)$
A
$e_1(t)$
$i_2(t)$
N
$e_3(t)$
B
C
$i_3(t)$
$e_2(t)$
PERMANENT
MAGNET ROTOR
α

Fig. 2.2: A star–connected BDCM

For $i, j = 1, 2, 3$ and $i \neq j$ the following terminology is used:
$v_j(t)$: the voltage across the phase j
r_j : the resistance of the phase j
$i_j(t)$: the current through the phase j
$e_j(t)$: the back–EMF in phase j
L_{jj} : the self inductance of phase j
L_{ij} : the mutual inductance between phase i and phase j

Based on [20] the circuit equations of the three phases expressed in phase variables are:

$$\begin{pmatrix} v_1(t) \\ v_2(t) \\ v_3(t) \end{pmatrix} = \begin{pmatrix} r_1 & 0 & 0 \\ 0 & r_2 & 0 \\ 0 & 0 & r_3 \end{pmatrix} \begin{pmatrix} i_1(t) \\ i_2(t) \\ i_3(t) \end{pmatrix} + \frac{d}{dt}\left(\begin{pmatrix} L_{11} & L_{12} & L_{13} \\ L_{21} & L_{22} & L_{23} \\ L_{31} & L_{32} & L_{33} \end{pmatrix} \begin{pmatrix} i_1(t) \\ i_2(t) \\ i_3(t) \end{pmatrix} \right) + \begin{pmatrix} e_1(t) \\ e_2(t) \\ e_3(t) \end{pmatrix}. \tag{2.1}$$

The domain of the airgaps is delimited by the rotor yoke (permanent magnet side) and the stator gap surface. When the assumption is made that the BDCM has uniform airgaps, the self inductances L_{jj} and mutual inductances L_{ij} of the phases are independed of the rotor displacement. This implies that the rotor reluctance (the 'magnetic resistance') is independed of the rotor position. It is common to assume that the characteristics of the phases are identical. Hence simplification of the set of equations is possible if it is assumed that all phase resistances, self inductions and mutual inductances are equal.

$$r_1 = r_2 = r_3 = R \tag{2.2}$$

$$L_{11} = L_{22} = L_{33} = L \tag{2.3}$$

$$L_{12} = L_{21} = L_{13} = L_{31} = L_{23} = L_{32} = M \tag{2.4}$$

and

$$\begin{pmatrix} v_1(t) \\ v_2(t) \\ v_3(t) \end{pmatrix} = \begin{pmatrix} R & 0 & 0 \\ 0 & R & 0 \\ 0 & 0 & R \end{pmatrix} \begin{pmatrix} i_1(t) \\ i_2(t) \\ i_3(t) \end{pmatrix} + \begin{pmatrix} L & M & M \\ M & L & M \\ M & M & L \end{pmatrix} \frac{d}{dt} \begin{pmatrix} i_1(t) \\ i_2(t) \\ i_3(t) \end{pmatrix} + \begin{pmatrix} e_1(t) \\ e_2(t) \\ e_3(t) \end{pmatrix}. \tag{2.5}$$

When the windings are star-connected as in Fig. 2.2, the summation of all the winding currents $i_1(t)$, $i_2(t)$ and $i_3(t)$ equals zero:

$$i_1(t) + i_2(t) + i_3(t) = 0$$

and hence

$$M i_2(t) + M i_3(t) = -M i_1(t). \tag{2.6}$$

From equations (2.5) and (2.6) follows

$$\begin{pmatrix} v_1(t) \\ v_2(t) \\ v_3(t) \end{pmatrix} = \begin{pmatrix} R & 0 & 0 \\ 0 & R & 0 \\ 0 & 0 & R \end{pmatrix} \begin{pmatrix} i_1(t) \\ i_2(t) \\ i_3(t) \end{pmatrix} + \begin{pmatrix} L-M & 0 & 0 \\ 0 & L-M & 0 \\ 0 & 0 & L-M \end{pmatrix} \frac{d}{dt} \begin{pmatrix} i_1(t) \\ i_2(t) \\ i_3(t) \end{pmatrix} + \begin{pmatrix} e_1(t) \\ e_2(t) \\ e_3(t) \end{pmatrix}. \tag{2.7}$$

The matrix element $(L-M)$ is often denoted in literature [11, 12, 20] as the synchronous induction L_s.
In state space form we have

$$\frac{d}{dt}\begin{pmatrix} i_1(t) \\ i_2(t) \\ i_3(t) \end{pmatrix} = \begin{pmatrix} \frac{1}{L-M} & 0 & 0 \\ 0 & \frac{1}{L-M} & 0 \\ 0 & 0 & \frac{1}{L-M} \end{pmatrix} \left(\begin{pmatrix} v_1(t) \\ v_2(t) \\ v_3(t) \end{pmatrix} - \begin{pmatrix} R & 0 & 0 \\ 0 & R & 0 \\ 0 & 0 & R \end{pmatrix} \begin{pmatrix} i_1(t) \\ i_2(t) \\ i_3(t) \end{pmatrix} - \begin{pmatrix} e_1(t) \\ e_2(t) \\ e_3(t) \end{pmatrix} \right). \quad (2.8)$$

The electromagnetic torque $T_e(t)$ of the motor is:

$$T_e(t) = (e_1(t)i_1(t) + e_2(t)i_2(t) + e_3(t)i_3(t))/\omega_m(t). \quad (2.9)$$

$\omega_m(t)$: mechanical rotor angle
$T_e(t)$: electrical torque

According to [20] the equation of motion is:

$$\frac{d}{dt}\omega_m(t) = (T_e(t) - T_L(t) - B_{mot}\omega_m(t))/J. \quad (2.10)$$

$T_L(t)$: load torque
B_{mot} : damping constant motor
J : moment of inertia of all rotating masses

2.3 Waveforms and Torque Production in Permanent Magnet Motors

The permanent magnet synchronous motor (PMSM) and the brushless DC motor (BDCM) both have permanent magnets on the rotor and need alternating stator currents to produce a constant torque. The difference is that the PMSM has a sinusoidal back-EMF and requires sinusoidal stator currents to produce constant torque. The BDCM has a trapezoidal back-EMF and requires rectangular stator currents to produce constant torque. In literature [20] it is made clear that a true BDCM should have a trapezoidal shaped back-EMF as in Fig. 2.3. The PMSM can be regarded as a special case of the BDCM where only the fundamental components of currents and flux are present. This can be explained with help of Fourier series.

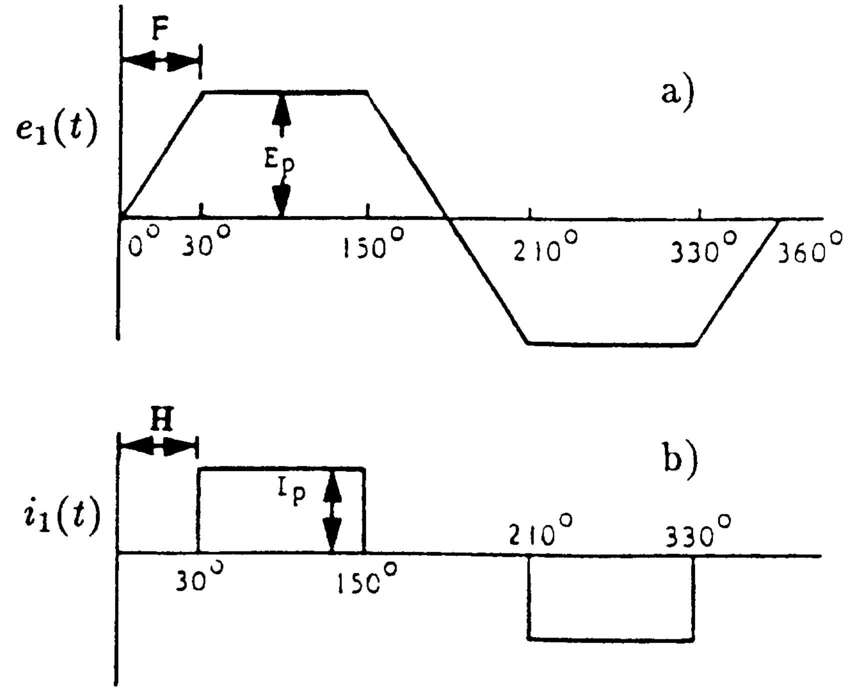

Fig. 2.3: Back-EMF and currents of a brushless DC motor [20].
a: Back-EMF of a brushless DC motor.
b: Current waveform required for a constant torque.

The flux linkage gradient $\kappa_{mj}(t)$ is defined [11] as the back-EMF $e_j(t)$ divided by the mechanical angular speed $\omega_m(t)$ and so has the same waveform as the back-EMF under nominal conditions. When the input current and the flux linkage gradient are perfect no torque pulsations are produced. Imperfections in the currents caused by the finite commutation times and imperfections in the flux linkage gradient due to the phase spread, finite slot numbers and manufacturing tolerances can arise. The effects of these imperfections can be studied by using a harmonic analysis of the torque in a BDCM.

We now consider a BDCM with idealized waveforms. Assume that the phase currents $i_1(t)$, $i_2(t)$ and $i_3(t)$ and the flux linkage gradients $\kappa_{m1}(t)$, $\kappa_{m2}(t)$ and $\kappa_{m3}(t)$ only differ in phase. Any periodic wave can be expressed as a Fourier series.

According to [20] the Fourier series of the flux linkage gradient is given by:

$$\begin{aligned}\kappa_{m1}(t) &= \frac{4E_p}{\pi F\omega_m(t)}\cdot(\sin(F)\sin(\omega_e t)+(\sin(3F)\sin(3\omega_e t))/3^2\\ &+ (\sin(5F)\sin(5\omega_e t))/5^2+\cdots). \qquad (2.11)\end{aligned}$$

Here F and E_p are defined as in Fig. 2.3.a, $\omega_m(t)$ is the mechanical rotor speed and t is the time in seconds. For a rectangular current the Fourier series is given by:

$$\begin{aligned}i_1(t) &= \frac{4I_p}{\pi}(\cos H\sin(\omega_e t)+(\cos 3H\sin 3(\omega_e t))/3\\ &+ (\cos 5H\sin 5(\omega_e t))/5+\cdots). \qquad (2.12)\end{aligned}$$

Here H and I_p are defined as in Fig. 2.3.b.

It is known [20] that current and flux linkage gradient harmonics of the same order interact to produce constant torque. Current and flux linkage gradient harmonics of different order will produce pulsating torques. The idealized waveforms from Fig. 2.3 will produce a constant torque. According to [20] the interaction of the fundamental component of the flux linkage gradient and the fundamental component of the current results in an electrical torque $T_e(t)$ after adding all three phases :

$$\begin{aligned}T_e(t) &= \frac{16E_pI_p}{\pi^2F\omega_m(t)}\{\sin(F)\sin(\omega_e t)\cos(H)\sin(\omega_e t)+\\ &\sin(F)\sin(\omega_e t-\frac{2\pi}{3})\cos(H)\sin(\omega_e t-\frac{2\pi}{3})+\\ &\sin(F)\sin(\omega_e t+\frac{2\pi}{3})\cos(H)\sin(\omega_e t+\frac{2\pi}{3})\Big\}. \qquad (2.13)\end{aligned}$$

Using:

$$\sin(\varphi+\chi)=\sin\varphi\cos\chi+\cos\varphi\sin\chi \qquad (2.14)$$

$$\sin^2\varphi+\cos^2\varphi=1 \qquad (2.15)$$

(2.13) can be rewritten into:

$$T_e(t) = \frac{24E_pI_p}{\pi^2F\omega_m(t)}\sin(F)\cos(H) \qquad (2.16)$$

Let $H = F = 30° = \frac{\pi}{6}$ then:

$$T_e(t) = \frac{144E_pI_p}{\pi^3\omega_m(t)}[\frac{1}{2}\cdot\frac{1}{2}\sqrt{3}] \qquad (2.17)$$

$$T_e(t) \approx 2.011E_pI_p/\omega_m(t).$$

When the back–EMF is trapezoidal it can be shown that the steady state torque is given by the interaction of the fundamental of the flux linkage gradient with the fundamental component of the current plus the interaction between the fifth harmonic of the flux linkage with the fifth harmonic of current etc. The interaction of all 3^n components (3, 9, 27, ...) equals zero so these terms can be excluded from the analysis. The interaction of the fifth harmonic flux linkage gradient with the fifth harmonic of current results in a steady state torque of:

$$\begin{aligned} T_5(t) &= -\frac{144E_pI_p}{(5\pi)^3\omega_m(t)}[\frac{1}{2}\cdot\frac{1}{2}\sqrt{3}] \\ T_5(t) &\approx -0.016088E_pI_p/\omega_m(t). \end{aligned}$$

The interaction of the seventh flux linkage gradient and current harmonics gives a torque of:

$$\begin{aligned} T_7(t) &= \frac{144E_pI_p}{(7\pi)^3\omega_m(t)}[\frac{1}{2}\cdot\frac{1}{2}\sqrt{3}] \\ T_7(t) &\approx 0.005863E_pI_p/\omega_m(t). \end{aligned}$$

The first, fifth and seventh harmonics total contribution is:

$$2.011E_pI_p/\omega_m(t) - 0.016088E_pI_p/\omega_m(t) + 0.005863E_pI_p/\omega_m(t) = 2.00078E_pI_p/\omega_m(t).$$

It is clear that the contribution of the fundamental components of flux linkage gradient and current are essentially responsible for the torque of the motor.

In practice, deviations from the idealized flux linkage gradient and current waveforms will occur. These deviations can be studied with the aid of Fourier series. One example of a deviation will now be discussed.

It will not be possible to force a rectangular current through the phases because the motor inductance limits the rate of change of the currents. The rise of the current is given by [20]:

$$i_1(t) = I_p\left\{1 - e^{-\frac{(L-M)t}{R}}\right\} \tag{2.18}$$

To avoid detailed calculations (2.18) is often approximated by a straight line [20]. This results in a trapezoidal shaped current as shown in Fig. 2.4. The Fourier series for the trapezoid from Fig. 2.4 can be written as:

$$\begin{aligned} i_1(t) &= \frac{4I_p}{\pi(H-h)}\left\{[\sin(H) - \sin(h)]\sin(\omega_e t) + [\sin(3H) - \sin(3h)]\sin(3\omega_e t)/3^2\right. \\ &+ \left.[\sin(5H) - \sin(5h)]\sin(5\omega_e t)/5^2 + \ldots\right\} \end{aligned} \tag{2.19}$$

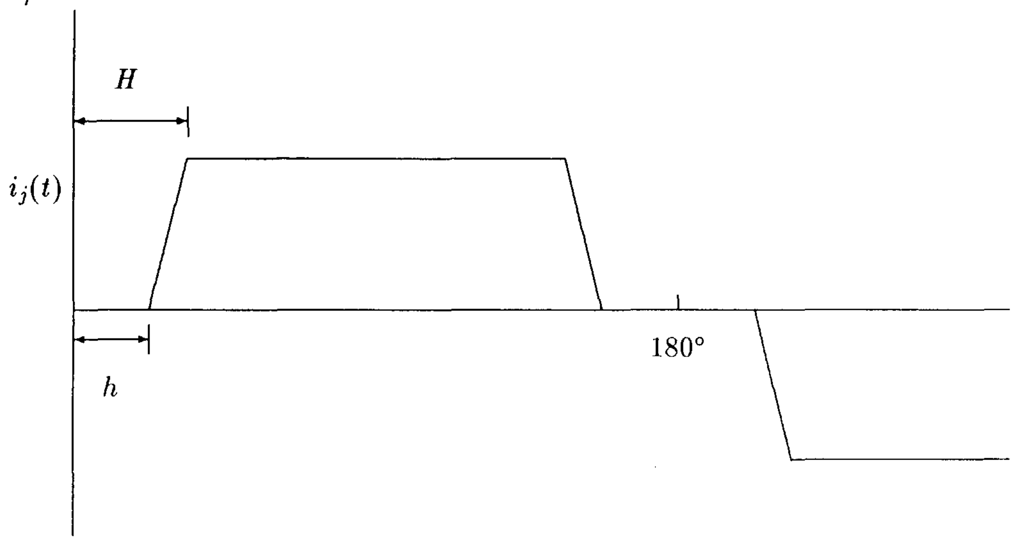

Fig. 2.4: A trapezoidal shaped phase current $i_j(t)$.

By changing the values of H and h in (2.19) the shape of the trapezoid of Fig. 2.4 can be affected. The value of $H - h$ is defined in [20] as the commutation angle. A nonideal flux density can be represented by increasing or decreasing F in (2.11). Similarly nonideal currents can be represented in (2.19) by changing h relatively to H.

To illustrate the effect of a commutation angle of 5° the Fourier series were calculated for a rectangular current (Fig. 2.5) and a trapezoidal current (Fig. 2.6). The flux density is the same for both cases. Fifty Fourier terms were used for this simulation. The effect on the torque when $H = 35°$ and $h = 30°$ can be seen in Fig. 2.5.c and Fig. 2.6.c. In these figures the flux linkage gradient, the current and torque are expressed per unit (p.u.). A unit is the maximum flux linkage gradient, current or torque for one phase.

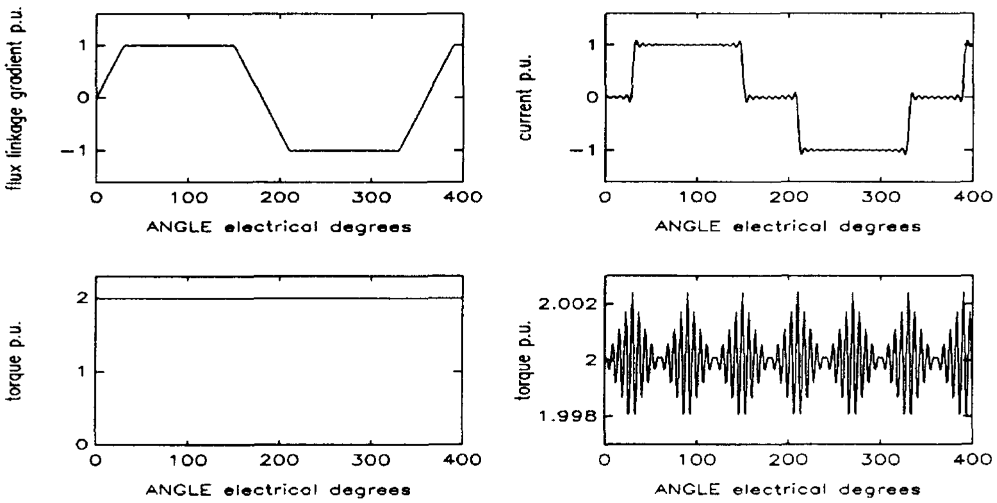

Fig. 2.5: Flux linkage gradient, current and total torque when the current is rectangular

a: the flux linkage gradient	b: rectangular current
c: total torque	d: total torque (zoom)

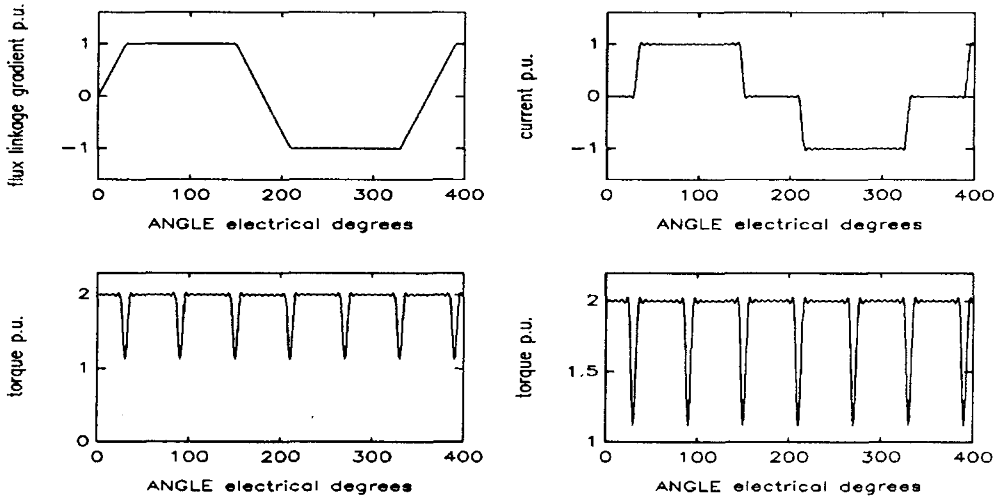

Fig. 2.6: Flux linkage gradient, current and total torque when the current is trapezoidal

a: the flux linkage gradient	b: trapezoidal current
c: total torque	d: total torque (zoom)

With the help of Fourier series a detailed investigation into the torque behavior of a BDCM has been presented. The use of a limited number of harmonics can give an impression of the shape of the produced torque. It is also possible to calculate the torque of a brushless motor by calculating the exact waveforms and then using (2.9).

2.4 Phase Circuits

There are two types of three phase motor interconnections. The phases can be connected in either a Y (wye) or a triangle, see Fig. 2.7. The wye connection is best known by the name star connection, the triangle connection is often called delta connection.

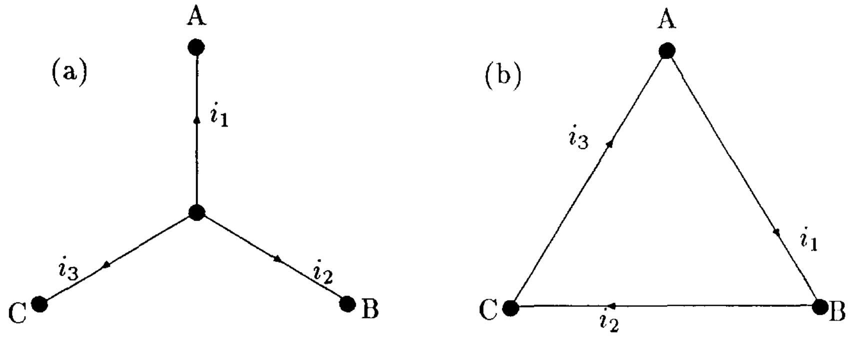

Fig. 2.7: The two phase interconnections
a: star
b: delta

The motor behaviour is mainly determined by how the phases are connected together. In many applications the motor control circuit, often called the inverter or converter, is able to reverse the currents in the phases without having to reverse the supply voltage. This is called full-wave motor control. It can be shown that when commutating a three phase BDCM that, unless one can reverse the current through the phases, it is only possible to produce torque/angle curves that are 120° apart. This results in a large torque ripple. If one can reverse the phase currents it is possible to produce torque/angle curves that are 60° apart, and thereby greatly reduce the torque ripple.

Trade–off between the Star and Delta Connection

In reference [15] it is claimed that the use of the star connection is a natural choice if one is interested to minimize the torque ripple. In Fig. 2.8 the torque production in a trapezoidal flux linkage motor with the two connections, star and delta is compared. For every winding of the star connected motor there are two seperate intervals, each of 120° electrical duration, within one excitation cycle, when the current is constant in the positive or negative sense (Fig. 2.8a). If these intervals coincide with the rotor being positioned on the constant gradient of the flux linkage characteristic, then the total motor torque, the summation over the three phases, is constant. In contrast, the delta connection leads to winding currents which flow throughout the excitation cycle (Fig. 2.8b). A constant total torque can only be produced if the characteristic of the flux linkage has an ideal triangular form. Small departures from this ideal will lead to significant torque ripple effects.

Although it is hard to find any motivation at all in literature why the star connection is so popular, it must be noted that in practice the current through the windings doesn't have to be so perfectly rectangular shaped as shown in Fig. 2.8. It doesn't seem very likely that the gradient of the flux linkage characteristic will also be perfectly constant as in Fig. 2.8. Hence, it is quite well possible that a delta connection sometimes is a better choice.

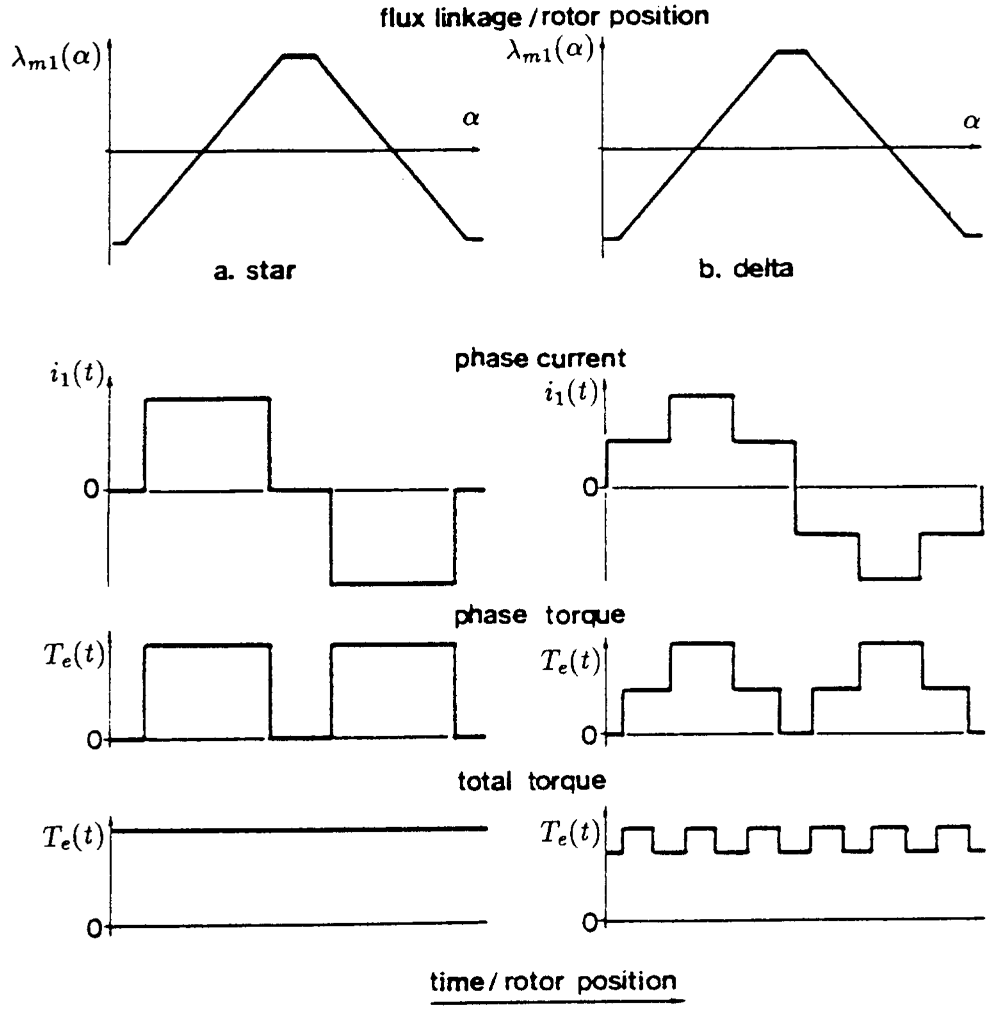
flux linkage / rotor position
$\lambda_{m1}(\alpha)$
α
a. star
$\lambda_{m1}(\alpha)$
α
b. delta
phase current
$i_1(t)$
0
$i_1(t)$
0
phase torque
$T_e(t)$
0
$T_e(t)$
0
total torque
$T_e(t)$
0
$T_e(t)$
0
time / rotor position

Fig. 2.8: Flux linkage gradient, phase current, phase torque and total torque
a: star connection
b: delta connection

The driving circuit of a three phase brushless DC motor may be connected in either a delta or a star (Fig. 2.7). The transistors may be conducting either 120° or 180° of one electrical period. The power supply may either be voltage source (voltage driven) or current source (current driven). Reference [25] contains a description of the eight possible combinations and compares the advantages and disadvantages of each case. The eight combinations are:

1. voltage driven, star connected, 120° conduction angle
2. voltage driven, star connected, 180° conduction angle
3. voltage driven, delta connected, 120° conduction angle
4. voltage driven, delta connected, 180° conduction angle
5. current driven, star connected, 120° conduction angle
6. current driven, star connected, 180° conduction angle
7. current driven, delta connected, 120° conduction angle
8. current driven, delta connected, 180° conduction angle.

Some terminology used in this section:

$i_{line}(t)$: the current applied to the inverter
$I_{line,av}$: the average line current (for one commutation interval)
$i_{Tindex}(t)$: the transistor current, $index = 1, 2, \ldots, 6$
I_{Trms} : root mean square value of the transistor current
KE : average back-EMF constant of the whole motor
ke : average back-EMF constant of each phase winding, 0 to peak value
KT : average torque constant of the motor
KT_t : the ratio of the average torque $T_{e,av}$ to the rms value of a transistor current I_{Trms}
R_m : the motor resistance when looking from the outside (the equivalent DC motor resistance)
R : resistance of each phase winding, all winding resistances are equal
$T_{e,av}$: the average torque developed by the motor
T_{rpl} : the torque ripple
V_s : supply voltage
$V_m(t)$: the voltage applied to the motor when looking from the outside
α : rotor position relatively to the stator
η : efficiency

In [25] a comparison of the eight cases in a static condition is made. The following assumptions were made to simplify the analysis:

- The voltage and current source are ideal. No source ripple is considered.
- The self induction L and the mutual induction M of the windings are ignored. The windings are considered to be pure resistances.

- The current is in phase with the back–EMF.
- The back–EMF is sinusoidal.
- The three phases are symmetrical with 120° phase shift.
- Voltage drops across the transistors are ignored.
- Some performance indices are speed dependent. A normal operating speed $\omega_m(t)$ is chosen where the motor has an efficiency η of about 55 to 65%. Efficiency η can be defined e.g. for the voltage driven circuit as:

$$\eta = \frac{\omega_m \cdot T_{e,av}}{V_s \cdot I_{line,av}} \cdot 100\% \tag{2.20}$$

The basic equation for a typical brushless DC motor given in [25] as:

$$V_m(t) = i_{line}(t) \cdot R_m + KE \cdot \omega_e(t). \tag{2.21}$$

The back–EMF for the different phases can be calculated:

$$\begin{aligned} e_1(t) &= ke \cdot \omega_e(t) \cdot \sin \alpha && (2.22)\\ e_2(t) &= ke \cdot \omega_e(t) \cdot \sin (\alpha - \frac{2\pi}{3}) && (2.23)\\ e_3(t) &= ke \cdot \omega_e(t) \cdot \sin (\alpha - \frac{4\pi}{3}) && (2.24) \end{aligned}$$

The torque ripple is defined in [25] as:

$$T_{rpl} = \frac{\max T_e(t) - \min T_e(t)}{T_{e,av}} \cdot 100\% \tag{2.25}$$

Where:

$\max T_e(t)$: maximum value of $T_e(t)$
$\min T_e(t)$: minimum value of $T_e(t)$

The ratio of the average torque $T_{e,av}$ to the rms value of a transistor current, e.g. i_{T1}:

$$KT_t = \frac{T_{e,av}}{i_{Trms}} \tag{2.26}$$

Some of the performance indices from Table 2.1 can be used to get some conclusions about the configuration that is preferable. The torque ripple T_{rpl} and the ratio of average torque to the rms value of the transistor current KT_t are very important indices. If T_{rpl} is too high the system will not work well. A high value of KT_t means an effective use of the transistors. From [25] can be concluded that all the cases of 180° conduction are not recommended. The transistor currents have bad waveforms and will therefore limit the motor speed. At high speeds it is possible that the transistor current is negative and a current will flow through the diodes. In all the cases of 180° conduction the torque ripples are very high. To illustrate this the torque ripples are plotted (bottom figures) for the

V–mode case [unit]	KE $[ke]$	R_m $[R]$	$\omega_e(t)$ $[\frac{v}{ke}]$	at speed $\omega_e(t)$ CT	 $Trpl$ [%]	 KT_t $[ke]$
Star 120°	1.65	2.0	0.36	0.99	6.0	3.85
Star 180°	1.43	1.5	0.3	0.93	26.5	3.48
Delta 120°	0.95	0.67	0.63	0.99	6.0	2.21
Delta 180°	0.83	0.5	0.57	0.91	29.0	2.1
I–mode case [unit]	KE $[ke]$	R_m $[R]$	$\omega_e(t)$ $[\frac{v}{ke}]$	CT	$Trpl$ [%]	KT_t $[ke]$
Star 120°	1.65	2.0	any	1.00	14.0	3.87
Star 180°	1.43	1.5	0.57	0.95	30.5	3.62
Delta 120°	0.95	0.67	any	1.00	14.0	2.24
Delta 180°	0.83	0.5	0.3	0.95	28.9	2.1

Table 2.1: Comparison between the star and delta connection

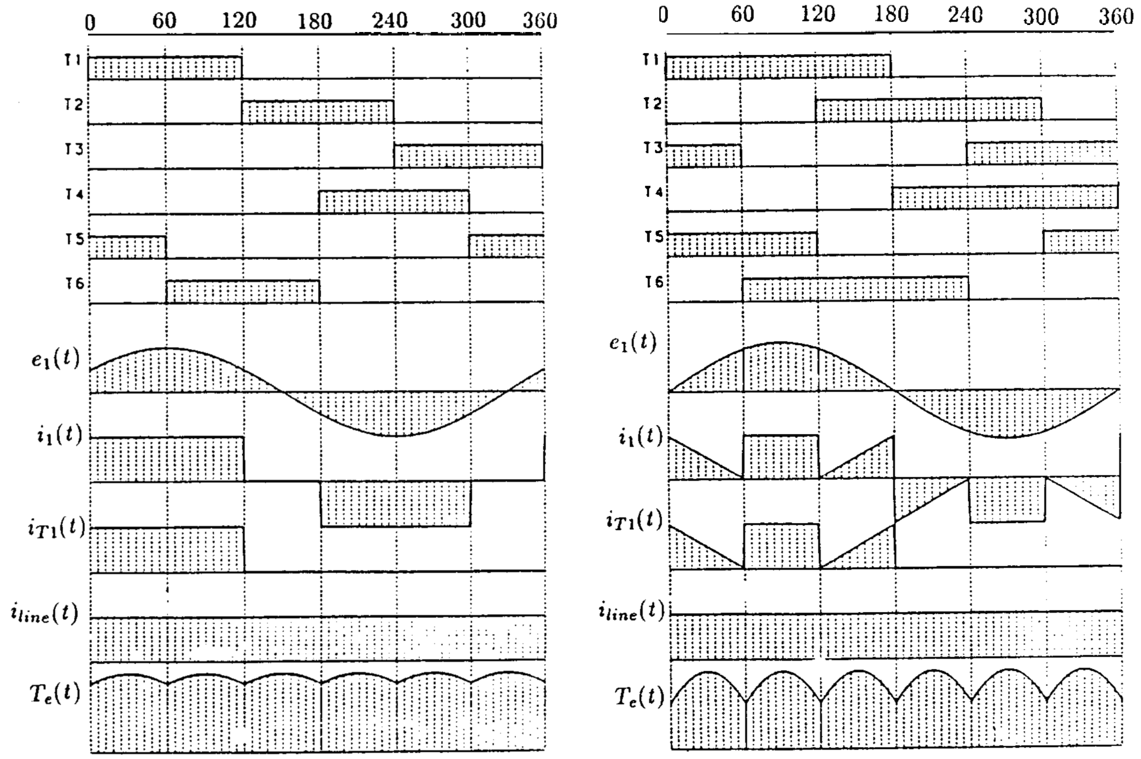

Fig. 2.9: Current source
a: star 120°
b: star 180°

current source case for conducting angles of 120° (Fig. 2.9.a) and 180° (Fig. 2.9.b). For

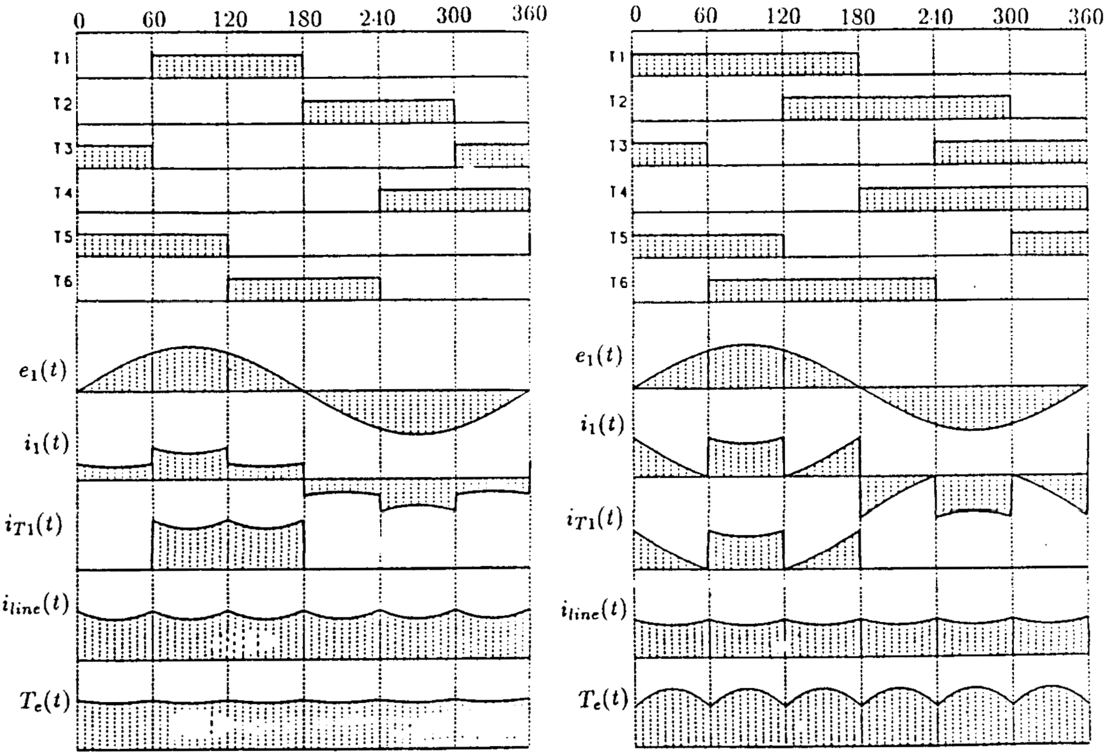

Fig. 2.10: Voltage source
a: delta 120°
b: star 180°

the voltage source and current source case the star 120° conduction angle is recommended because it has a higher KT_t for both cases (Table 2.1). When comparing KT_t for the star and delta (Table 2.1) 120° cases, the current source case is recommended. The current source case needs less devices than the voltage source case. Another advantage is that the current source has a speed independent torque ripple T_{rpl} and torque constant KT. In other words this means that if the system is working under the range of the power source voltage capability, KT is independent of the rotor speed.

2.5 Commutation Strategies

A commutation (switching) strategy is a sequence of voltages that can be applied to the nodes **A**, **B** and **C** of the motor in Fig. 2.7. There are three possible states at a node. One can apply to a node the supply voltage (V_s), ground (**g**), or leave the node open circuited (**o**). Since there are three nodes this means that there are 3^3 possible states for a circuit in the delta or star connection. Out of these 27 possible node combinations there are only 12 that will produce torque from a supply voltage at zero speed. According to [21] there is one group of six states which results from putting supply voltage or ground at each of the nodes. This is called the **node closed strategy**. The node closed strategy will produce torque/angle curves of equal magnitude separated by 60° intervals. There is a second set of six states which will also produce torque/angle curves of equal magnitude separated by 60°. This set results from applying supply voltage, ground or leaving one node open. This is called the **node open strategy**. The first set would be commutated at electrical angles 60°, 120° and so on. The second set would be commutated at angles 30°, 90°, 150° etc. So for both motor connection schemes there are two useful driver schemes. It should be noted, that the other states which do not produce any torque from an applied supply voltage can be used as dynamic braking states. They would cause currents to flow due to the back–EMF when the motor is operating at a given speed.

In table 2.2 the star node open states are tabulated in order of increasing angle.

Interval	Node			Constraints	
	A	B	C		
330° → 30°	o	V_s	g	$v_3 - v_2 = V_s$,	$i_1 = 0, i_2 = -i_3$
30° → 90°	g	V_s	o	$v_1 - v_2 = V_s$,	$i_3 = 0, i_1 = -i_2$
90° → 150°	g	o	V_s	$v_1 - v_3 = V_s$,	$i_2 = 0, i_1 = -i_3$
150° → 210°	o	g	V_s	$v_2 - v_3 = V_s$,	$i_1 = 0, i_2 = -i_3$
210° → 270°	V_s	g	o	$v_2 - v_1 = V_s$,	$i_3 = 0, i_1 = -i_2$
270° → 330°	V_s	o	g	$v_3 - v_1 = V_s$,	$i_2 = 0, i_1 = -i_3$

Table 2.2: Star node open phase constraints for each commutation interval

A three phase full-wave brushless motor system is represented in Fig. 2.11. The stator is connected in a star and the windings are positioned 120° from the other. Two transistors are connected to the end points of each stator leg. For every winding there are diodes connected across the transistors. A diode must be present to handle the inductive transient current in each winding as it is commutated.

The diagram of Fig. 2.11 shows the torque function T(index) of each combination of two windings. This function shows for each combination the contribution of torque at various shaft angles, when a constant current is flowing in that combination. The conduction in one leg is always continuous when the other is being commutated. When in Fig. 2.11 transistor **Q1** is energized between 0 and 60°, **Q5** is also conducting and a current is flowing from point **A** to point **B**. During the next sequence (60–120°) **Q6** is energized and a current will flow from point **A** to point **C**. In the meantime the current through leg **B** declines to zero by conducting through **D2**, so the conduction angle per phase is 120°. The circuit requires only a single power supply. At any time 67% of the available windings is being used (67% duty factor).

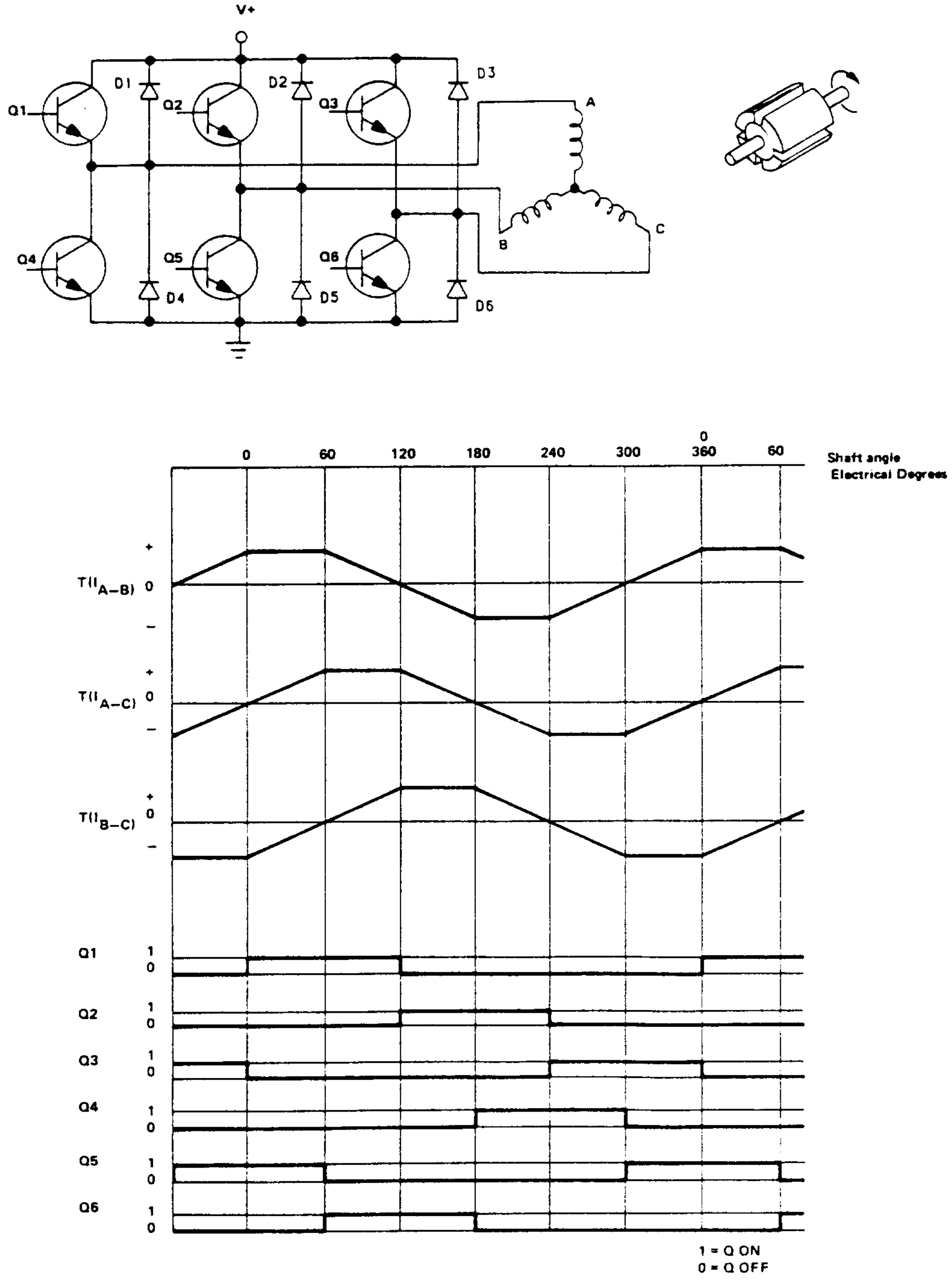
V+
Q1
D1
Q2
D2
Q3
D3
A
B
C
Q4
Q5
D4
Q6
D5
D6
0
60
120
180
240
300
0
360
60
Shaft angle
Electrical Degrees
$T(I)_{A-B}$
$T(I)_{A-C}$
$T(I)_{B-C}$
+
0
-
Q1
Q2
Q3
Q4
Q5
Q6
1
0
1 = Q ON
0 = Q OFF

Fig. 2.11: The controller configuration, torque function and the logic sequence for a three phase, full-wave BDCM.

2.6 The Back–EMF Sensing Principle

In a brushless DC motor the commutation timing is electronically determined by integrated circuits (ICs). These ICs provide the power to the stator windings. With the use of the back–EMF sensing principle the commutation moments can be derived from the zero-crossings of the back–EMF. This means that the need for rotor positioning sensors, like magnetoresistive or Hall-effect sensors, is eliminated. The absence of back–EMF when the motor is starting is a disadvantage, so the IC must include a start-up circuit. The principle of the back–EMF sensing can be illustrated with Fig. 2.12, taken from [1].

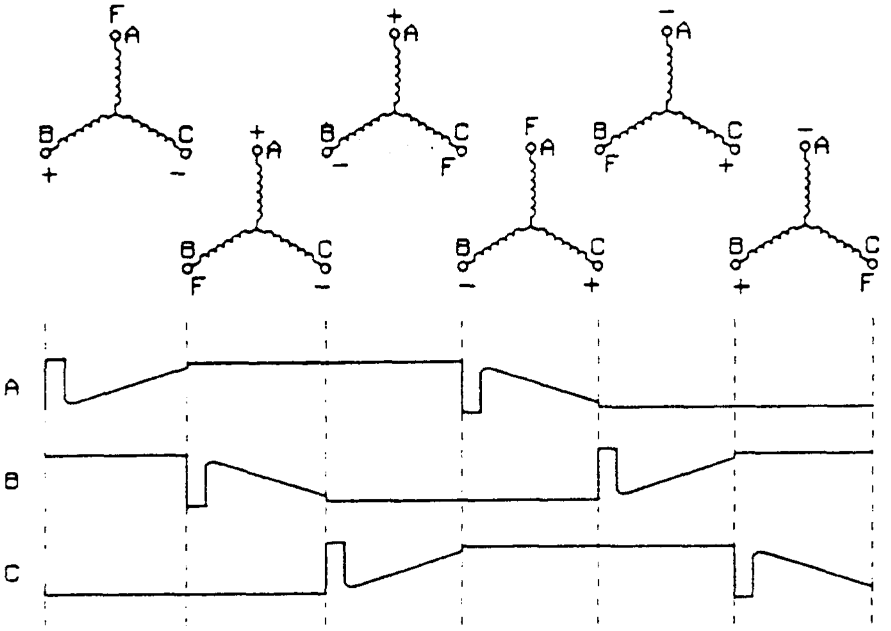

Fig. 2.12: The six states of the power outputs (one cycle)

For a brushless three phase DC motor one electrical cycle can be divided in six states of the power stages. In each state one of the windings is connected to the plus, one to the minus and the third is floating (open) (Fig. 2.12). In the floating state (F) the output stage is switched off, the output impedance is high so the voltage is only determined by the back–EMF. The current is sent through the coils in both directions, so full-wave drive is realized. An back–EMF sensing system is based on detecting the back–EMF when a winding is in the floating stage. The interval between the detection of a zero-crossing of the back–EMF and the next commutation, **the commutation delay**, should not exceed 30° of the energizing cycle (360°) under nominal conditions. The commutation delay is defined on the IC by an adaptive delay block. Each interval between two successive energizing-half cycles (twice the commutation delay) is measured, halved to obtain the commutation delay, and stored by constant-current charging/discharging of two capacitors, named **CAP-DC** and **CAP-CD** in [20]. One capacitor, **CAP-DC**, is charged during one commutation period (60°) with an interruption of the charging current during the diode pulse. During the next commutation period this capacitor is discharged at twice the charging current, see Fig. 2.13 from [20]. The other capacitor **CAP-CD** is used to repeat the same delay (30°) and so determines the timing of the next commutation. To avoid any problems with the flyback pulse which occurs after one of the IC outputs has been switched off, a **watchdog time** is defined by the IC. Without the watchdog a flyback pulse could be detected as a false zero-crossing. During the watchdog time the motor has to recover from a diode pulse to a back–EMF voltage, see Fig. 2.14 from [20]. Under nominal conditions the back–EMF recovers in a short time, $\ll$ 1ms. In [20] a capacitor called **CAP-TI** is used for the timing of the watchdog, see Fig. 2.14.

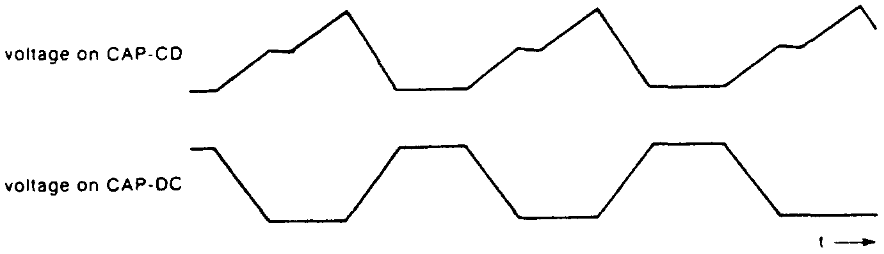

Fig. 2.13: The **CAP-DC** and **CAP-CD** voltage waveforms in normal running mode

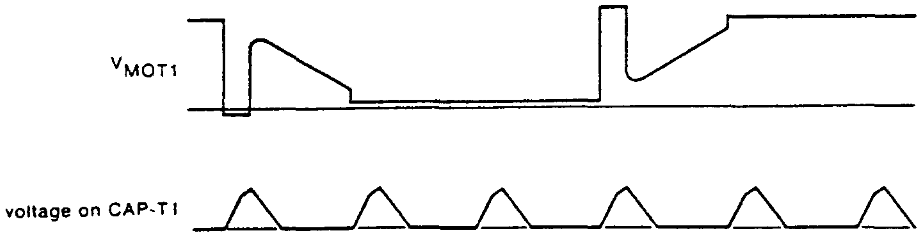

Fig. 2.14: Typical **CAP-TI** and motor voltage waveforms in normal running mode

Though the back–EMF sensing can generate very accurate tacho pulses, some inaccuracies are possible. These inaccuracies can be caused by unequal angles between stator phases. Also back–EMF distortion caused by asymmetry in the electromagnetic circuit of the motor could be a source of disturbances. In Chapter 5 problems concerning asymmetry are looked at more fully.

Chapter 3

Accurate Modelling of Brushless DC Motors

In this chapter some accurate models will be presented for a three phase brushless DC motor. These models include the effects of non–uniformity of the airgap between the stator phases and the rotor poles, saturation and eddy current losses. In Section 3.1 a model will be presented for a BDCM with non–uniform airgaps. A model including the magnetic saturation is discussed in Section 3.2.

3.1 Modelling of a BDCM with Non–Uniform Airgaps

When reluctance variations as a function of the rotor displacement become significant, the uniform airgap model of Section 2.2 will not be accurate enough. In Fig. 3.1 a three phase two pole BDCM is shown. It is clear that as the rotor rotates, the length of the

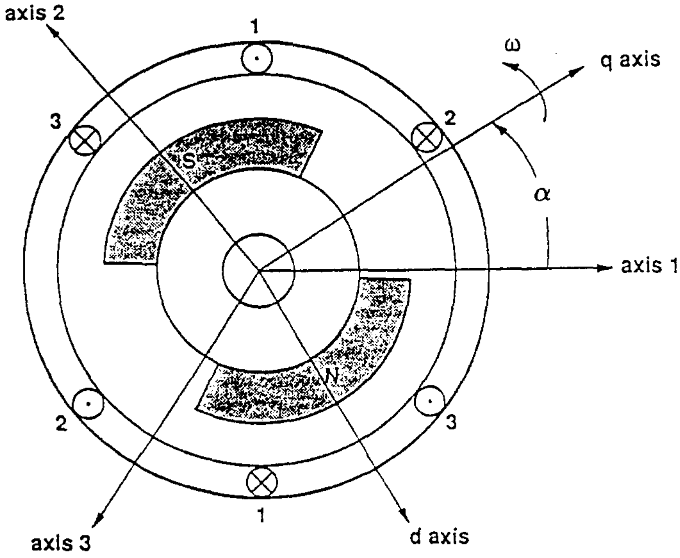

Fig. 3.1: A three phase two pole BDCM with stationary and rotating frames. [11]

airgap varies and as a result the reluctance of the flux path varies. For the three phase two pole BDCM from Fig. 3.1 this means that the variation of the reluctance repeats twice during one complete rotation of the rotor. For the explanation of the rotating frame see Section 3.3.

According to [11] the governing differential equations for a BDCM may be written as:

$$\vec{V}(t) = [R]\,\vec{I}(t) + \frac{d\vec{\Lambda}(\vec{I}(t),\alpha)}{dt} \tag{3.1}$$

where

$$[R] = diag(R) \tag{3.2}$$

$$\vec{V}(t) = \begin{pmatrix} v_1(t) \\ v_2(t) \\ v_3(t) \end{pmatrix} \tag{3.3}$$

$$\vec{I}(t) = \begin{pmatrix} i_1(t) \\ i_2(t) \\ i_3(t) \end{pmatrix} \tag{3.4}$$

$$\vec{\Lambda}(\vec{I}(t),\alpha) = [L(\alpha)]\,\vec{I}(t) + \vec{\Lambda}_m(\alpha) \tag{3.5}$$

$$[L(\alpha)] = \begin{pmatrix} L_{11}(\alpha) & L_{12}(\alpha) & L_{13}(\alpha) \\ L_{21}(\alpha) & L_{22}(\alpha) & L_{23}(\alpha) \\ L_{31}(\alpha) & L_{32}(\alpha) & L_{33}(\alpha) \end{pmatrix} \tag{3.6}$$

$$\vec{\Lambda}(\vec{I}(t),\alpha) = \begin{pmatrix} \lambda_1(\vec{I}(t),\alpha) \\ \lambda_2(\vec{I}(t),\alpha) \\ \lambda_3(\vec{I}(t),\alpha) \end{pmatrix} \tag{3.7}$$

$$\vec{\Lambda}_m(\alpha) = \begin{pmatrix} \lambda_{m1}(\alpha) \\ \lambda_{m2}(\alpha) \\ \lambda_{m3}(\alpha) \end{pmatrix} \tag{3.8}$$

Here $[R]$ is the resistance matrix and $\vec{V}(t)$ represents the voltage inputs across the phase windings. The displacement of the rotor is represented by α. The self inductance of the phase windings is represented by L_{jj} and the mutual inductance between phase i and j is denoted by $L_{ij} = L_{ji}$, see Section 2.2 The flux linkage associated with the permanent magnet and the different phases is represented by the vector $\vec{\Lambda}_m(\alpha)$. Note that this description of the equations is not different from the one presented in Section 2.2. The product of the derivatives of the flux linkages $\vec{\Lambda}_m(\alpha)$ to the mechanical rotor angle α and the mechanical speed $\omega_m(t)$ equals the back electromotive force. For the first phase the back–EMF that is due to the presence of the permanent magnets can be determined as follows:

$$e_1(t) = \frac{d\lambda_{m1}(\alpha)}{dt} = \frac{d\lambda_{m1}(\alpha)}{d\alpha} \cdot \frac{d\alpha}{dt} = \frac{d\lambda_{m1}(\alpha)}{d\alpha}\omega_m(t) \tag{3.9}$$

In [11] the assumption of sinusoidal distribution of the stator windings is made. This means that the back-EMF will be sinusoidal and that the self and mutual inductances for a BDCM can be written as follows:

the self inductances:

$$L_{jj}(\alpha) = L_a - L_g \cdot \cos(2\,n\,\alpha + \frac{2(j-1)\pi}{3}); \quad for \quad j = 1,2,3 \tag{3.10}$$

the mutual inductances:

$$L_{12}(\alpha) = L_{21}(\alpha) = -\frac{L_a}{2} - L_g \cdot \cos(2\,n\,\alpha - \frac{2\pi}{3}) \tag{3.11}$$

$$L_{13}(\alpha) = L_{31}(\alpha) = -\frac{L_a}{2} - L_g \cdot \cos(2\,n\,\alpha - \frac{4\pi}{3}) \tag{3.12}$$

$$L_{23}(\alpha) = L_{32}(\alpha) = -\frac{L_a}{2} - L_g \cdot \cos(2\,n\,\alpha) \tag{3.13}$$

where L_g is the amplitude of variation in induction due to the non-uniform air gap and L_a represents the nominal value of the inductance of the winding. The number of permanent magnet pole pairs is n. The expression for the electromagnetic torque T_e that is generated by the motor can be derived from the coenergy function $W_c(\vec{I}(t),\alpha)$:

$$T_e(\vec{I}(t),\alpha) = \frac{\partial W_c(\vec{I}(t),\alpha)}{\partial \alpha} \tag{3.14}$$

where

$$W_c(\vec{I}(t),\alpha) = \sum_{j=1}^{3} \int \lambda_j \, di_j \tag{3.15}$$

$$\lambda_j(t) = \sum_{i=1}^{3} L_{ij}\, i_i(t) + \lambda_{mj}. \tag{3.16}$$

For a sinusoidal distribution of the stator windings the parameters λ_{mj} can be written as:

$$\lambda_{mj} = ke \cdot \sin(n\,\alpha - \frac{2(j-1)\pi}{3}); \quad for \quad j = 1,2,3. \tag{3.17}$$

Here ke is the electromotive force constant.

Using (3.15) – (3.17) and (3.10) – (3.13) the torque expression (3.14) yields:

$$\begin{aligned} T_e(\vec{I}(t),\alpha) \;=\; & n\,L_g \Big\{ 2[\sin(2\,n\,\alpha - \frac{2\pi}{3})\, i_1(t)\, i_2(t) + \sin(2\,n\,\alpha + \frac{2\pi}{3})\, i_1(t)\, i_3(t) + \\ & \sin(2\,n\,\alpha)\, i_2(t)\, i_3(t)] + \sum_{j=1}^{3} i_j^2(t) \cdot \cos(2\,n\,\alpha + \frac{2(j-1)\pi}{3}) \Big\} + \\ & n \cdot ke \sum_{j=1}^{3} i_j(t) \cdot \cos(2\,n\,\alpha + \frac{2(j-1)\pi}{3}) \end{aligned} \tag{3.18}$$

The result of (3.18) does not look attractive, but one of the phase currents $i_1(t)$, $i_2(t)$ or $i_3(t)$ is always zero during one commutation interval. If e.g. $i_3(t)$ is zero (3.18) can be written as:

$$\begin{aligned} T_e(\vec{I}(t),\alpha) &= n\,L_g\left\{2\,\sin(2\,n\,\alpha-\frac{2\pi}{3})\,i_1(t)\,i_2(t)+\sum_{j=1}^{2} i_j^2(t)\cdot\cos(2\,n\,\alpha+\frac{2(j-1)\pi}{3})\right\} \\ &+ n\cdot ke\sum_{j=1}^{2} i_j(t)\cdot\cos(2\,n\,\alpha+\frac{2(j-1)\pi}{3}) \end{aligned} \tag{3.19}$$

3.2 Modelling of a BDCM with Magnetic Saturation

In this section the modelling of a BDCM in the presence of magnetic saturation will be addressed. The mathematical modelling in absence of magnetic saturation has been presented in the previous section. When large torques have to be produced, large phase currents are needed. These phase currents can lead to magnetic saturation of the flux paths in the motor. The mathematical modelling presented in this section will be based on [11] and [12].

When magnetic saturation is present, the flux linkages can not be written in terms of constant inductances. The only thing one can state about the flux linkage λ_j is:

$$\lambda_j = \lambda_j(i_1, i_2, i_3, \alpha) \tag{3.20}$$

This equation defines a set of 4-dimensional surfaces. Experimental procedures can be used to find approximate descriptions of the flux linkage surfaces.
We now consider equation (3.1):

$$\vec{V}(t) = \vec{R}\,\vec{I}(t) + \frac{d\vec{\Lambda}(\vec{I}(t),\alpha)}{dt}.$$

When the rotor displacement is fixed at $\alpha = \xi$, we write:

$$\lambda_j(i_1, i_2, i_3, \xi) = \int_0^t [v_j(\tau) - R\,i_j(\tau)]d\tau. \tag{3.21}$$

According to [12] this integral should be evaluated at discrete values of the phase currents and ξ in order to obtain a set of points representing λ_j. This can be done by varying the phase current and phase voltage and sampling their values with respect to time. Approximate mathematical models for the flux linkage surfaces can be obtained after having collected enough data points lying on the flux linkage surfaces. The best fitting surfaces through the experimental flux linkage data points can now be computed. It is a small step from the representations for the flux linkages λ_1, λ_2 and λ_3 of the individual phases to the coenergy function W_c from which we can derive an expression for the torque. In [12] this is done as follows:

$$W_c(i_1, i_2, i_3, \alpha) = \int_0^{i_1} \lambda_1(\alpha, \gamma, 0, 0) d\gamma + \int_0^{i_2} \lambda_2(\alpha, i_1, \eta, 0) d\eta + \int_0^{i_3} \lambda_3(\alpha, i_1, i_2, \zeta) d\zeta. \quad (3.22)$$

Now the torque function T_e can be computed from:

$$T_e(i_1, i_2, i_3, \alpha) = \frac{\partial W_c(i_1, i_2, i_3, \alpha)}{\partial \alpha} \quad (3.23)$$

The torque function is an explicit function of time so there is a need for explicit commutation strategies. If the purpose for constructing this accurate model for a BDCM has been to be able to use it for real-time control it looks unattractive because of the complexity of the mathematical relationships. A less complicated model based on the one in this section will be presented in Section 3.3.

3.3 A BDCM Model with Saturation in Rotating Frame

In this section a transformation will be introduced that can be used to obtain a simplified formulation for a BDCM in a rotating frame attached to the rotor. This transformation is known by the name Park transformation, see [11] and [20]. The Park transformation is given below:

$$\begin{pmatrix} \sigma_q \\ \sigma_d \\ \sigma_0 \end{pmatrix} = (\frac{2}{3}) \begin{pmatrix} \cos(n\alpha) & \cos(n\alpha - \frac{2\pi}{3}) & \cos(n\alpha + \frac{2\pi}{3}) \\ \sin(n\alpha) & \sin(n\alpha - \frac{2\pi}{3}) & \sin(n\alpha + \frac{2\pi}{3}) \\ \frac{1}{2} & \frac{1}{2} & \frac{1}{2} \end{pmatrix} \begin{pmatrix} \sigma_1 \\ \sigma_2 \\ \sigma_3 \end{pmatrix} \quad (3.24)$$

The variables $\sigma_q, \sigma_d, \sigma_0, \sigma_1, \sigma_2$ and σ_3 can represent currents, voltages and flux linkages. The subscripts 1, 2, 3 correspond to the stator windings. The subscripts q, d and 0 represent fictitious windings attached to the rotor. When the Park transformation is used the dependence of the inductance parameters on the rotor displacement α will be eliminated. The Park transformation can not directly be used when magnetic saturation is present [11]. First the behaviour of the BDCM model with saturation must be formulated by a piecewise linear model. In this case the flux linkages are modelled by piecewise linear functions of the phase currents. Now a simplified description of the BDCM with saturation can be applied. The parameters that define the flux linkages, such as the electromotive force constant ke and the inductances, are now piecewise constant functions of the phase currents. The BDCM with saturation in rotating frame is represented by:

$$v_q = R\, i_q(t) + n\, \lambda_d(t) \cdot \frac{d\alpha(t)}{dt} + \frac{d\lambda_q(t)}{dt} \quad (3.25)$$

$$v_d = R\, i_d(t) - n\, \lambda_q(t) \cdot \frac{d\alpha(t)}{dt} + \frac{d\lambda_d(t)}{dt} \quad (3.26)$$

where

$$\begin{aligned}
\lambda_q(t) &= L_q(\vec{I}(t))\, i_q(t) && (3.27)\\
\lambda_d(t) &= L_d(\vec{I}(t))\, i_d(t) + ke(\vec{I}(t)) && (3.28)\\
L_q(\vec{I}(t)) &= \frac{3}{2}\left(L_a(\vec{I}(t)) - L_g(\vec{I}(t))\right) && (3.29)\\
L_d(\vec{I}(t)) &= \frac{3}{2}\left(L_a(\vec{I}(t)) + L_g(\vec{I}(t))\right). && (3.30)
\end{aligned}$$

The torque expression after transformation is:

$$T_e(i_q, i_d) = \frac{3n}{2}\left\{\lambda_d(t)\; i_q(t) + \lambda_q(t)\; i_d(t)\right\}. \qquad (3.31)$$

The saturated BDCM can be described by three constant functions of current, $L_a(\vec{I}(t))$, $L_g(\vec{I}(t))$ and $ke(\vec{I}(t))$. The flux linkages corresponding to individual phase windings are functions of these three parameters. The experimental identification process can be performed for each phase winding independent of the rest. So for one phase winding we write:

$$\lambda_j(i_j, i_k = 0, i_m = 0) = \lambda_j(i_j, \alpha); \quad j, k, m = 1, 2, 3. \qquad (3.32)$$

The flux linkage now represents a 2-dimensional surface instead of a 4-dimensional surface. We can now write:

$$\lambda_j(i_j, \alpha) = \int_0^t [v_j(\tau) - R\; i_j(\tau)] d\tau. \qquad (3.33)$$

The flux linkages can be constructed by sampling the phase current i_j and the phase voltage v_j and computing (3.33). When a sufficient number of data points has been collected, a mathematical model for each of the flux linkage surfaces can be obtained by using optimalization techniques.

3.4 Modelling of a BDCM with Iron Losses

Any conductor in an alternating magnetic field will have a back-EMF induced in it, [13]. These EMFs cause currents, the so called eddy currents, and associated power losses. The magnetic fields are due to currents flowing in the conductor in question (e.g. a stator winding) or in other conductors and (moving) permanent magnets. The losses in current-carrying conductors can be represented as an additional resistance above the measured value with DC. It must be noted that this increase of the resistance depends on frequency. The resistance and the losses become larger as frequency increases.

From [3] it can be concluded that as speed increases the dynamic performance decreases due to the eddy current losses. These eddy currents are present in:

- the housing
- the permanent magnet

- the laminated and non-laminated circuits
- mounting elements such as the screws to fix the laminations and the motor.

It should be noted that magnets themselves offer negligible paths for the flow of currents, as ferrite and rare earth magnets have a very low electrical conductivity, see [8]. According to [3] and [17], the eddy current losses present in a three phases brushless DC motor can be modelled by three equivalent short-circuit windings, aligned with the main stator windings. This model is shown in Fig. 3.2.

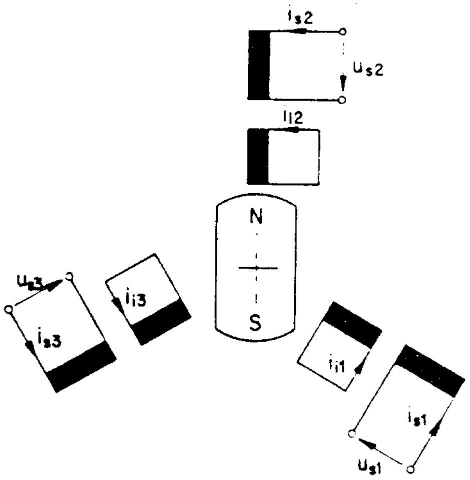

Fig. 3.2: A model of a BDCM with Iron Losses (i_{i1}, i_{i2} and i_{i3} in the figure).

Usually the iron losses are modelled as follows:

The eddy current losses:

$$P_e = C_e\, f^2\, \hat{B}^2\, M_f \tag{3.34}$$

P_e : the eddy current losses
C_e : eddy current losses coefficient
M_f : mass of iron parts
$\hat{B}$: the peak flux density in the iron.

The hysteresis losses in the iron:

$$P_h = C_h\, f^2\, \hat{B}^x\, M_f \tag{3.35}$$

P_h : the hysteresis losses
C_h : hysteresis losses coefficient.

According to [10] the approximate value of x varies from 1.6 to 2 with different grades of iron. When for different frequencies the losses P_e and P_h are known the parameters for the eddy current losses can be determined. These parameters are:

R_f : an equivalent iron phase resistance
$L_{\sigma f}$: an equivalent iron phase leakage inductance.

The expressions for the voltage and torque of one phase j, which include the iron losses, can now be written down.

$$v_j = R\, i_j + (L - M)\,\frac{di_j}{dt} + e_j + L_{sf}\,\frac{di_{fj}}{dt} \tag{3.36}$$

e_j : back–EMF across phase j
i_{fj} : the current in the iron phase j
L : self inductance of a phase
M : mutual inductance between phases
L_{sf} : mutual inductance between a stator phase and the iron.

As already has been mentioned the iron losses are modelled as short-circuit windings, so the voltage equation for one iron phase (index j) is:

$$0 = R_f\, i_{fj} + L_{ff}\,\frac{di_{fj}}{dt} + e_{fj} + L_{sf}\,\frac{di_j}{dt} \tag{3.37}$$

e_{fj} : back–EMF of short–circuit iron winding j
L_{ff} : equivalent iron phase self-inductance
L_{fj} : mutual inductance between the iron and the permanent magnet.

An important feature is that the voltages e_j and e_{fj} are proportional (principle of equivalent iron winding).

$$e_{fj} \;=\; \beta\, e_j. \tag{3.38}$$

β : a constant value between 0 and 1.

It is now possible to compute the total torque of the motor. This total torque is equal to the summation of the torques of the individual phases, so:

$$T_e = \sum_{j=1}^{3}\left(\frac{e_j}{\omega_e}\, i_j + \frac{e_{fj}}{\omega_e}\, i_{fj}\right) + T_d + T_h. \tag{3.39}$$

T_d : the detent torque due to the reluctance effect
T_h : the hysteresis torque due to iron hysteresis losses.

Although the mathematical description of the iron losses is not very complicated, a problem seems to be an accurate determination of the parameters that appear in (3.37) and (3.38). In [17] it is not made clear how this can be done.

Chapter 4

Damping Circuits

In this chapter a brief description will be given about the design of the circuits needed in an inverter to limit overvoltages. The overvoltages can occur due to the inductance of a phase of a BDCM during the commutation (switching) between two intervals of the commutation cycle. In the first section it is explained what snubbers (damping components) are. In the second section an analysis is given of the waveforms that appear when the diode characteristics are simplified. In the last section a more elaborated model of the diode waveform is discussed.

4.1 What are Snubbers?

When a motor winding is switched off a flyback pulse appears. This flyback pulse is an overvoltage which results from the inductance in series with the diode. Flyback pulses may cause high frequency interference and accoustic noise. The overvoltages could damage the diodes and transistors of the inverter.

The flyback pulses can be damped by an R_s-C_s combination in parallel with the motor windings or in parallel with the inverter diodes. This damping component is called a snubber. A snubber reduces the high frequency interference. It can also reduce accoustic noise by several dB, depending on the construction of the motor [27].

Snubbers also have some negative effects. They dissipate energy from the flyback pulses and contribute to the overall power consumption. When the back–EMF sensing principle (see Section 2.5) is used a negative effect is caused by the remainder of the step response due to the snubber. This step response may cause a shifting of zero–crossing , so effects of damping components must be negligible when a zero–crossing is expected.

4.2 Snubber Circuits, assuming Snap–off

The snubber analysis presented here is based on [22]. In Fig. 4.1.a a step-down converter circuit is shown where L_l is a leakage inductance. This leakage inductance can be seen as an equivalent of the induction of a phase of a brushless DC motor. When switch T in Fig. 4.1.a is closed the diode D will stop conducting (step down). For the purposes of snubber analysis this circuit is an equivalent circuit for almost any other inverter where diodes are used [22].

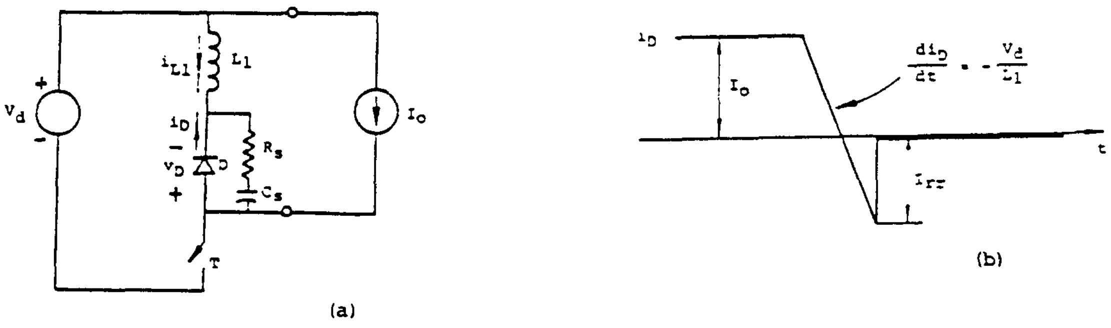

Fig. 4.1: An R_s-C_s snubber in a step down converter
a: Step-down converter
b: the diode recovery current assuming snap-off.

When the current through a diode i_D reaches the value I_{rr} (reverse recovery current) it is assumed that i_D stops conducting instantaneously (**snaps off**) as shown in Fig. 4.1.b.

The load is inductive because of L_l, and it is assumed that the load current I_o in Fig. 4.1.a is constant during the switching transients. In order to obtain an equivalent circuit, the switch T shown in Fig. 4.1.a is assumed to be ideal. This results in a worst case analysis of the diode snubber. The instant of the diode snap-off at the peak reverse recovery current I_{rr} (see Fig. 4.1.b) is treated as the initial time. The initial inductor current in the equivalent circuit is I_{rr}. The equivalent circuit is shown in Fig. 4.2.

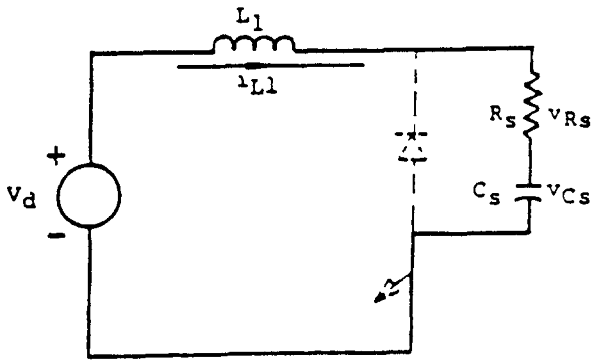

Fig. 4.2: The equivalent circuit for snubber analysis after diode recovery.

As a first approach the snubber resistance R_s is set to be zero. This simplifies the analysis and illustrates the basic ideas of snubber design. The capacitor voltage v_{Cs} in this case can be obtained as:

$$v_{Cs} = V_d - V_d \cos \omega_o t + I_{rr} \sqrt{\frac{L_l}{C_s}} \sin \omega_o t \qquad (4.1)$$

$$\omega_o = \frac{1}{\sqrt{L_l C_s}} \qquad (4.2)$$

A base capacitance will now be introduced,

$$C_{base} = L_l \left[\frac{I_{rr}}{V_d}\right]^2 \tag{4.3}$$

so it is possible to write (4.1) as

$$v_{Cs} = V_d \left[1 - \cos\omega_o t + \sqrt{\frac{C_{base}}{C_s}} \sin\omega_o t\right] \tag{4.4}$$

and the maximum value of V_{Cs} can be calculated as

$$v_{Cs,max} = V_d \left[1 + \sqrt{1 + \frac{C_{base}}{C_s}}\right]. \tag{4.5}$$

Because $R_s = 0$ the maximum reverse diode voltage v_{Dmax} is the same as $v_{Cs,max}$. The maximum diode voltage v_{Dmax}, expressed as the ratio of V_d , is plotted in Fig. 4.3 as a function of $\frac{C_{base}}{C_s}$. For small values of C_s the maximum diode voltage becomes excessive.

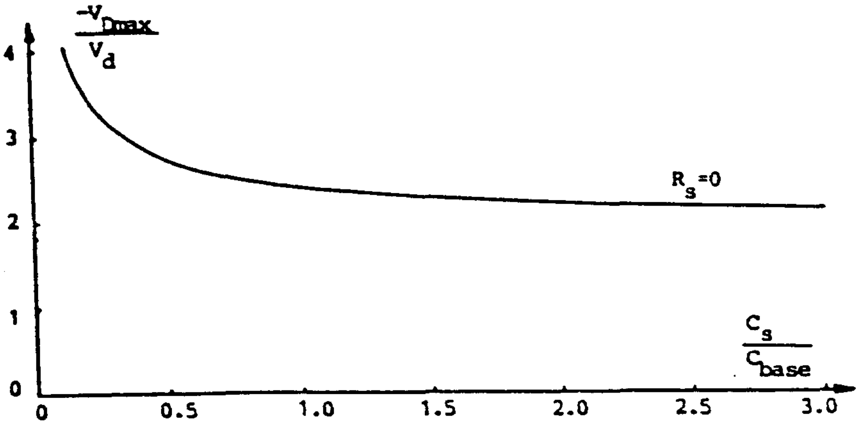

Fig. 4.3: The maximum diode voltage as a function of C_s when $R_s = 0$.

When the diode snubber resistance R_s is included in the analysis, the circuit waveforms can be found by analytical calculations or by computer simulations. The oscillations in these waveforms are damped due to R_s. The maximum diode voltage depends on the values of R_s and C_s. For a selected value of C_s the maximum diode voltage varies with R_s. For $C_s = C_{base}$ some normalized diode voltage waveforms are plotted in Fig. 4.4. The resistor R_s is normalized by:

$$R_{base} = \frac{V_d}{I_{rr}} \tag{4.6}$$

In Fig. 4.4 the time axis is normalized with t_{rr}, the reverse recovery time. This is the time between the start of a negative diode current i_D and the start of reverse recovery as i_D reaches the value I_{rr}. For a given C_s there is an optimum value of $R_s = R_{sopt}$ which minimizes the maximum diode voltage v_{Dmax}, see Fig. 4.5. The energy loss in the resistor R_s at diode reverse recovery is according to [22]

$$W_{Rs} = \frac{1}{2} L_l I_{rr}^2 + \frac{1}{2} C_s V_d^2. \tag{4.7}$$

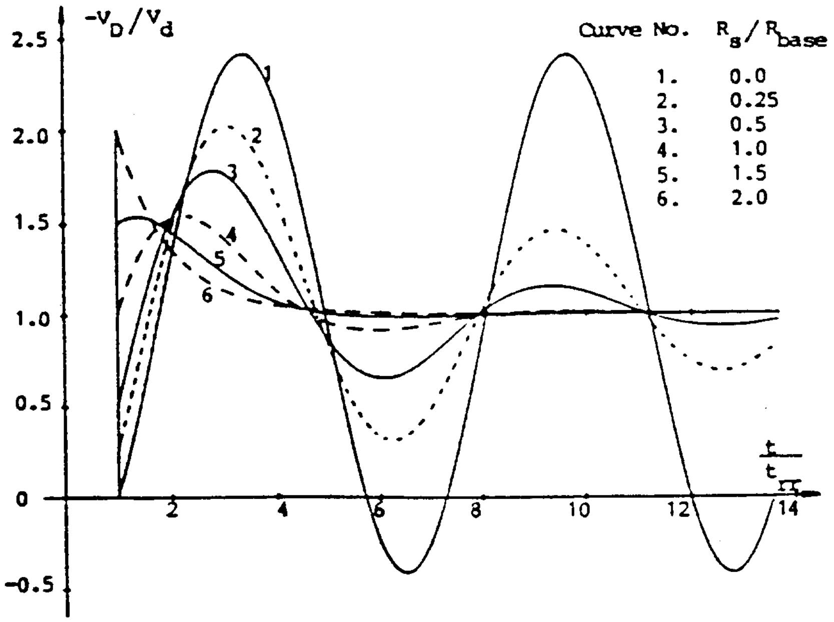

Fig. 4.4: The diode voltage waveforms for $C_s = C_{base}$ and a set of R_s.

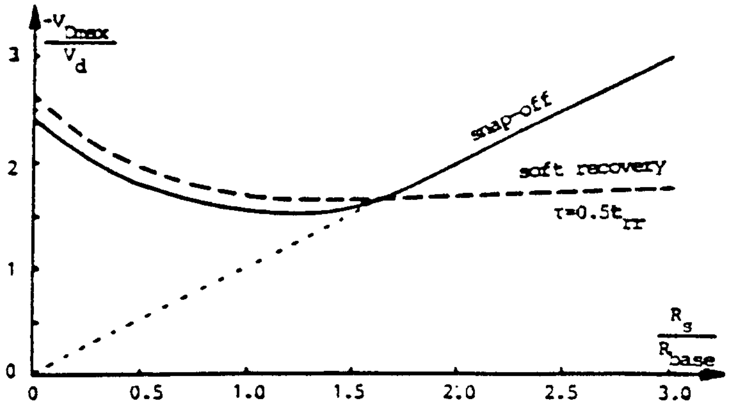

Fig. 4.5: $-\frac{v_{Dmax}}{V_d}$ as a function of R_s for snap-off and soft recovery with $\tau = 0.5t_{rr}$.

At the end of the current oscillations, the energy that is stored in the capacitor C_s equals

$$W_{Cs} = \frac{1}{2}C_s V_d^2 \tag{4.8}$$

which is dissipated in the resistor at the next turn-on of the diode. The total energy loss in the snubber resistance is given in [22] as

$$W_{tot} = W_{Rs} + W_{Cs} = \frac{1}{2}L_l I_{rr}^2 + C_s V_d^2 = \frac{1}{2}L_l I_{rr}^2 + \frac{C_s}{C_{base}} L_l I_{rr}^2. \tag{4.9}$$

4.3 Snubber Circuits, assuming Soft Recovery

In Section 4.2 was assumed that the reverse recovery current I_{rr} of the diode snaps off instantaneously, see Fig. 4.1.b. In practice however the diode current recovers as shown in Fig. 4.6.a. The current waveform after the diode reverse recovery decays exponentially. This is called **soft recovery.** Soft recovery can be accommodated in an equivalent circuit as shown in Fig. 4.6.b. In [22] the reverse recovery charge is defined as $Q_{rr} = Q_1 + Q_2$.

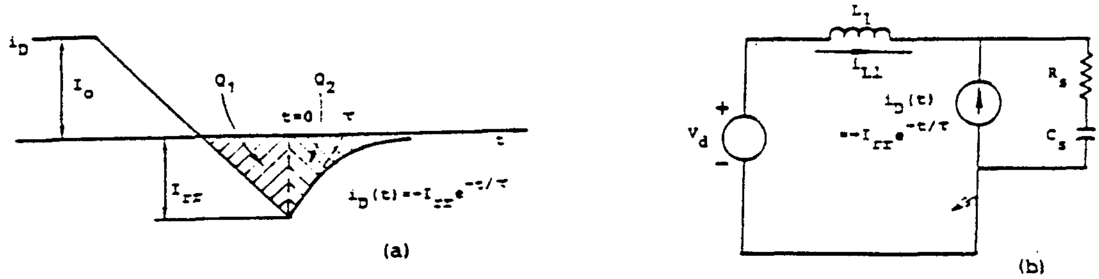

(a)

(b)

Fig. 4.6: Recovery of the diode current
a: The soft reverse recovery
b: The equivalent circuit for soft recovery.

When assuming $Q_1 = \frac{1}{2}Q_{rr}$, τ, the soft recovery time constant, will be $\frac{1}{2}t_{rr}$ and

$$I_{rr} = \sqrt{2Q_1\frac{di}{dt}} = \sqrt{Q_{rr}\frac{di}{dt}} = \sqrt{Q_{rr}\frac{V_d}{L_l}} \tag{4.10}$$

Now an indication can be given of the influence of the soft recovery time constant τ when $C_s = C_{base}$. In Fig. 4.5 the dotted line shows $-\frac{v_{Dmax}}{V_d}$ as a function of R_s with $\tau = \frac{1}{2}t_{rr}$. When $C_s = C_{base}$, the optimal snubber resistance $R_{sopt,\tau}$ increases as τ increases, see Fig. 4.7. Though the increase in $R_{sopt,\tau}$ is significant, the overvoltage when using $R_{sopt,\tau}$ is not much less then when using R_{sopt} (snap-off). This is because the overvoltage is certainly dependent on R_s for soft recovery, as shown in Fig. 4.5. Some physical understanding of the factors affecting the overvoltage may be gained from Fig. 4.8. This figure shows the influence of the soft recovery time constant τ on the turn-off waveforms.

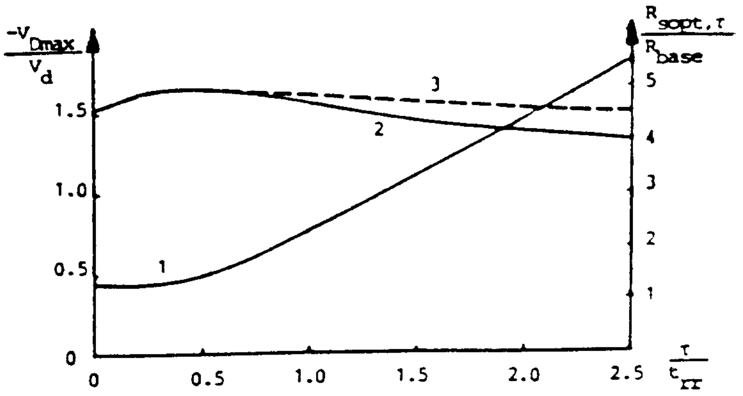

Fig. 4.7: For $C_s = C_{base}$
1: The optimum resistance value $R_{sopt,\tau}$ as function of τ
2: $-\frac{v_{Dmax}}{V_d}$ with $R_s = R_{sopt,\tau}$ as function of τ
3: $-\frac{v_{Dmax}}{V_d}$ with $R_s = 1.3R_{base} = R_{sopt}$ (snap-off) as function of τ

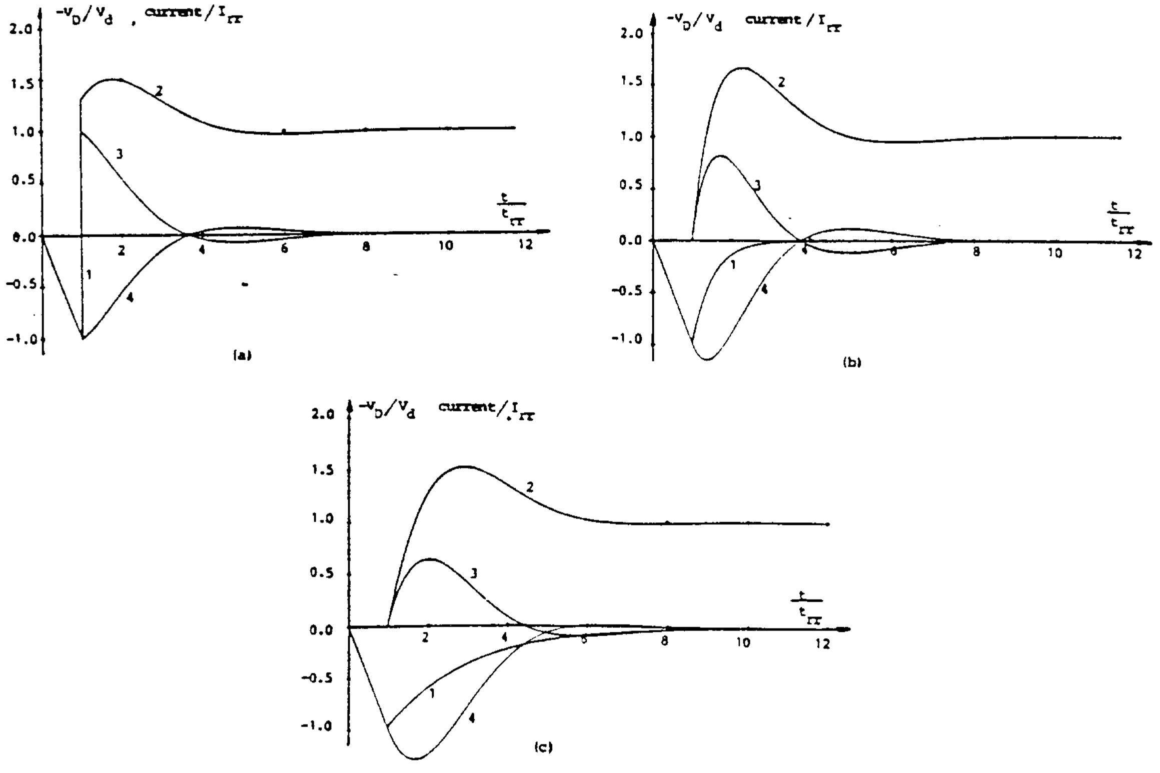

Fig. 4.8: The simulated waveforms for the diode current {1}, the diode voltage {2}, the snubber current {3} and the current in the leakage inductance {4}
a: assuming snap-off b: soft recovery $\tau = \frac{1}{2}t_{rr}$
c: soft recovery $\tau = 2t_{rr}$

Chapter 5

Influence of Changes in Parameters on Performance

In this chapter the influence of changes in mechanical, electrical and magnetic parameters on the motor performance will be discussed. Only very little information on this subject was found in literature. What will be presented in this chapter is mainly based on the references [2, 4, 5, 6]. The considered motor is a BDCM. More particularly a spindle DC motor will be studied. In reference [5] a spindle DC motor with a radial airgap is considered. The motor considered in [6] is a spindle DC motor with an axial airgap. The spindle DC motor configuration with a radial airgap is shown in Fig. 5.1. The spindle DC motor with an axial airgap is shown in Fig. 5.2.

The performance determination is based on a computation method [2] like the one presented in appendix A. The method is based on the division of the electromechanical system into small homogeneous parts where the induction is assumed to be constant.

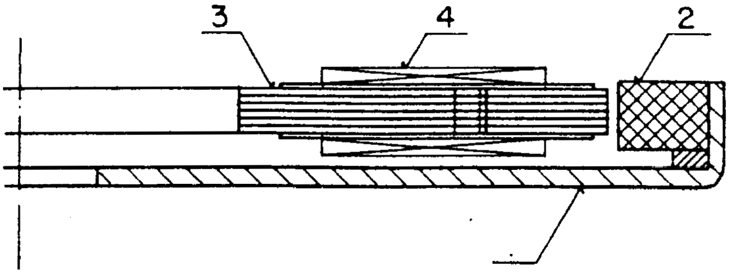

Fig. 5.1: Configuration of a spindle DC motor with radial airgap.
1: Rotor bell 2: Permanent magnet ring
3: Stator stack 4: Winding

5.1 Summary of Steps in Performance Determination

A small summary of the method presented in appendix A will now be given.

The determination of the motor performance can be divided in five main steps:

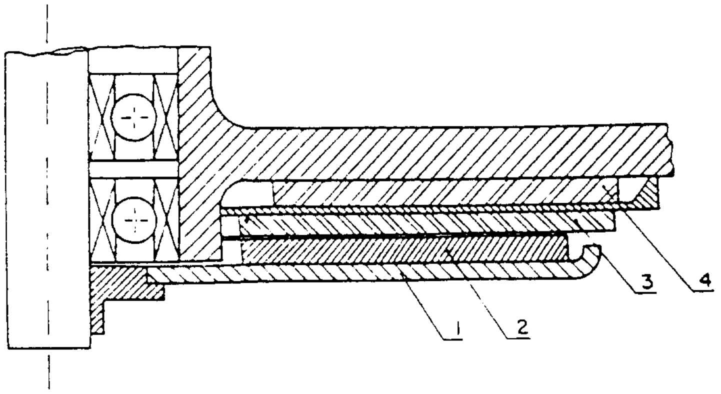

Fig. 5.2: Configuration of a spindle DC motor with axial airgap.
1: Rotor 2: Permanent magnet
3: Coil 4: Return path stator

1. *Determination of the equivalent magnetic circuit*: assumptions permit to define a network of **permeances** which represent various parts of the motor (rotor, stator, airgap, permanent magnets). Permeances are defined in appendix A. Each motor winding is represented by a source of magnetic potential. The permanent magnets are also represented by their magnetic equivalent schemes.

2. *Determination of the oriented graph associated with the equivalent magnetic scheme*: the oriented graph is a scheme in which the direction of flux in each branch of the equivalent magnetic scheme is defined.

3. *Determination of the flux equations*: after determination of the oriented graph, the flux equations for each branch of the magnetic circuit can be expressed. These equations are non-linear. The magnetic field (more specific the permeance) in each branch of the magnetic circuit is chosen as the variable.

4. *Determination of the torque*: the torque developed by the motor is determined taking into account the saturation effects. The equivalent MMF across the permanent magnet is the product of the magnetic field strength of the magnet and the height (direction of magnetisation) of the magnet. The MMF is a function of the position of the rotor relatively to the stator.
   The torque is expressed as

$$T_e = \frac{1}{2}\sum_{j=1}^{n'} \frac{d\Upsilon_{\delta j}}{d\alpha} \cdot \Theta_{\delta j}^2 + \frac{1}{2}\sum_{k=1}^{n''} \frac{d\Upsilon_{\rho k}}{d\alpha} \cdot \Theta_{\rho j}^2 \qquad (5.1)$$

   Here are :

   $\Upsilon_{\delta j}$: airgap permeance j
   $\Theta_{\delta j}$: equivalent MMF across the airgap permeance j
   n' : number of airgap permeances
   $\Upsilon_{\rho k}$: equivalent permanent magnet permeance k
   $\Theta_{\rho k}$: equivalent MMF across the equivalent permanent magnet permeance k
   n'' : number of permanent magnet permeances
   α : rotor position

5. *Determination of the inductances and incremental inductances*: finally the average inductances and incremental (or differential) inductances can be calculated. Average inductance is defined as

$$L_{KP} = \sum_{i=1}^{n} \sum_{j=1}^{n} S_{KP,ij} \cdot C_{ij} \cdot \Upsilon_{ij} \tag{5.2}$$

with:

$K = 1, 2, \ldots, m$
$P = 1, 2, \ldots, m$
m = number of phases
n = number of branches of the equivalent magnetic circuit

where:

$S_{KP,ij}$: coupling factor between phase K and phase P in relation with branch i and branch j of the equivalent magnetic scheme.
C_{ij} : coupling factor between branch i and branch j of the equivalent magnetic scheme (+1 or -1).
Υ_{ij} : permeance between the branches i and j

The incremental inductance is defined as

$$L'_{KP} = L_{KP} + \sum_{y=1}^{m} \frac{\delta L_{Ky}}{\delta i_y} \cdot i_y \tag{5.3}$$

where i_y is the current in phase y.

5.2 The Spindle DC Motor with a Radial Airgap.

5.2.1 Influence of the Axial Dimension and Motor Asymmetries

The static determination as presented in appendix A is complete as far as the motor is symmetric and the axial dimension in not important. In reality the closeness of the rotor bell to the stator has an influence on the distribution of the flux in the axial direction of the motor, see Fig. 5.1. It is possible that an attractive axial force between the stator and the rotor is present.

Asymmetries in stator or rotor dimensions can produce a radial force between the stator and the rotor. This means that the torque equation (5.1) must be completed with:

a radial force F_δ:

$$F_\delta = \frac{1}{2}\sum_{j=1}^{n'} \frac{d\Upsilon_{\delta j}}{d\delta} \cdot \Theta_{\delta j}^2 \tag{5.4}$$

an axial force F_z:

$$F_z = \frac{1}{2}\sum_{j=1}^{n'} \frac{d\Upsilon_{\delta j}}{dz} \cdot \Theta_{\delta j}^2 \tag{5.5}$$

where:

index δ : the radial airgap
index z : the axial airgap
n' : number of airgap permeances

5.2.2 The Symmetric Motor

According to [5] the symmetric motor can be considered as a theoretical motor where the geometry, the electrical parameters and the magnetic parameters are symmetric. For the spindle DC motor with radial airgap considered in [5] only a fourth of the motor geometry has to be considered in order to determine all the parameters and distribution functions. The computing method presented in appendix A was used in [5] to determine:

- *The permanent magnet MMF distribution.* In case of the spindle DC motor from [5] a full magnetisation will be considered. The effects of the gradient of two consecutive pole transitions are included in the analysis. In Fig. 5.3 the distribution of the permanent magnet MMF in the airgap is presented.

- *Inductances.* The calculation of the inductance when no currents are present shows the leakage flux in the motor. In [5] the following values were determined:

self inductances	:	1.23 mH
mutual inductances	:	−0.292 mH
inductance of 2 phases in series, direct current	:	3.44 mH

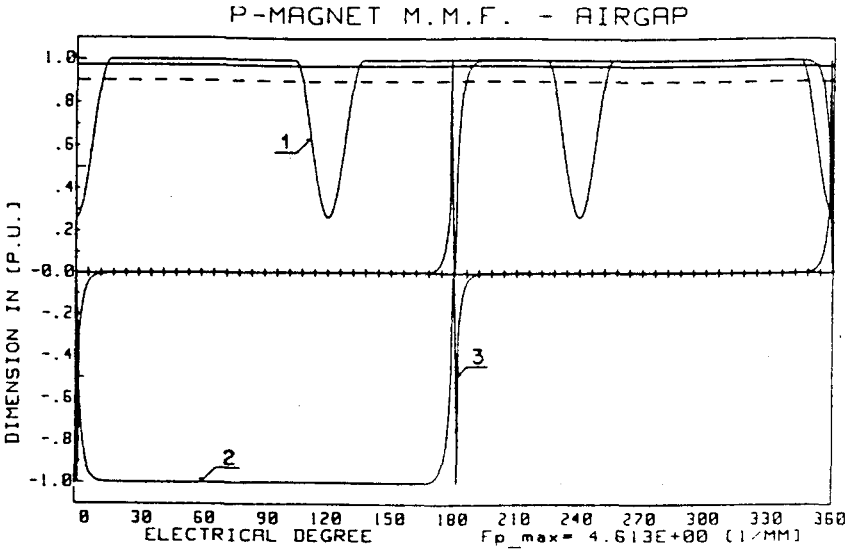

Fig. 5.3: The permanent magnet MMF distribution.
1: Airgap distribution 2: MMF distribution
3: MMF gradient

- *The detent torque.* The detent torque is due to the non-uniformity of the airgap. For a symmetric motor with eight rotor poles (= 4 pole pairs) and twelve stator teeth the detent torque T_d has 24 (lowest common multiple of 8 and 12) cycles in one geometrical turn (= 360°).
  Consequently the detent torque has a $360 \times \frac{\text{number of pole pairs}}{\text{number of cycles per geometrical turn}} = 60^\circ$ (electrical) period. Based on the symmetry of the geometry the detent torque satisfies:

$$T_d(30^\circ + a) = -T_d(30^\circ - a) \tag{5.6}$$

In Fig. 5.4 the calculated detent torque is shown. When the motor is energized in a two-phases-on-mode, the total torque and its components are shown in Fig. 5.5. In a two-phases-on-mode two phases of the brushless motor are conducting a current at any moment of the commutaton cycle.

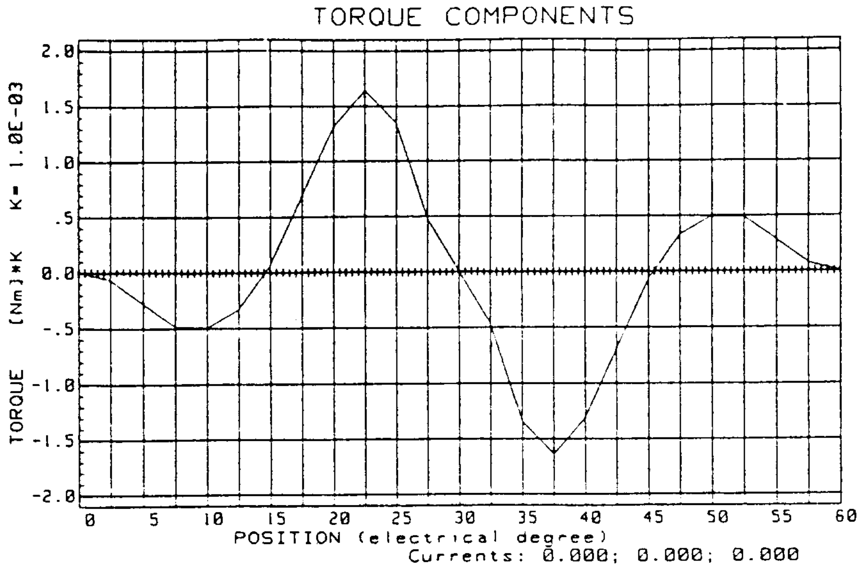

Fig. 5.4: The detent torque of the symmetric motor.

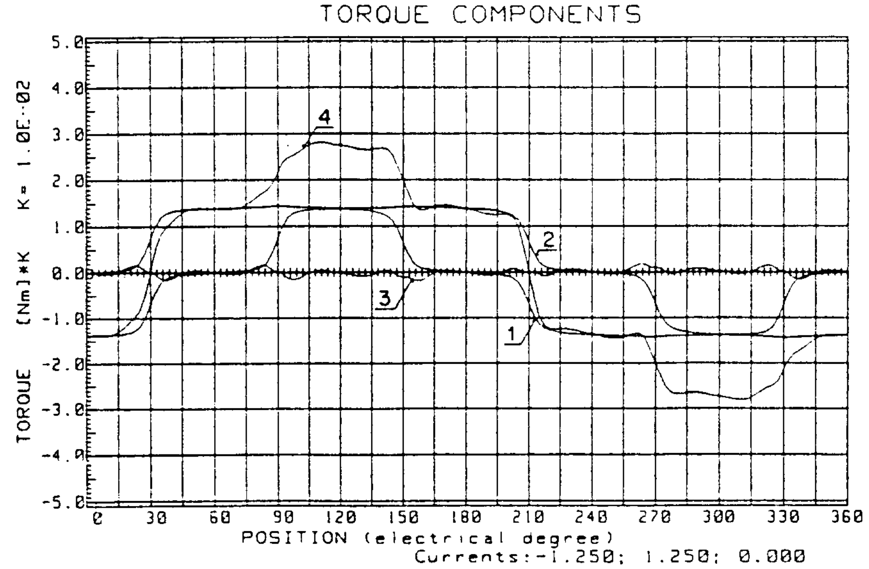

Fig. 5.5: Total torque and torque components.

1: mutual torque between the first phase and the permanent magnet
2: mutual torque between the second phase and the permanent magnet
3: detent torque
4: total torque

5.2.3 The Real Motor

According to [5] and [6] the real motor distinguishes itself from the symmetric motor because of the following changes:

- the distribution of the permanent magnet MMF is non-uniform due to the influence of the magnetizer geometry

- variation in stator slot openings, for example due to presence of Hall-sensors.

The possible configuration of the magnetizer will have an influence on the resulting MMF of the permanent magnet after magnetisation. More particularly the slot opening of the magnetizer has a direct effect on the resulting MMF. The flux line distribution in the magnetizer is shown in Fig. 5.6. It is determined with the help of a finite element method. Fig. 5.7 presents the resulting permanent magnet MMF measured on the inner surface of the permanent magnet ring. For this measurement the ring has been placed in the air. The curves are obtained for different permanent magnet rings that have been magnetized by different magnetizers. It should be noted that once a permanent magnet ring is placed in the motor neither of the two curves from Fig. 5.7 represents the real MMF. Fig. 5.8 represents the detent torque and Fig. 5.9 the total torque due to the change in MMF gradient between two consecutive permanent magnet poles.

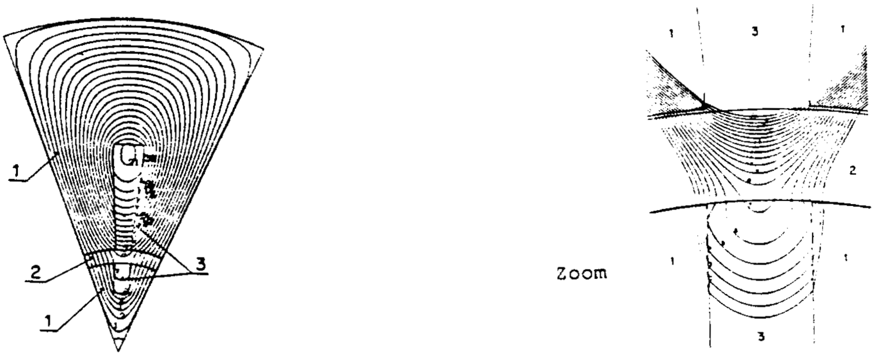

Fig. 5.6: The magnetizer flux line distribution.
1: magnetizer lamination 2: permanent magnet not magnetized
3: winding

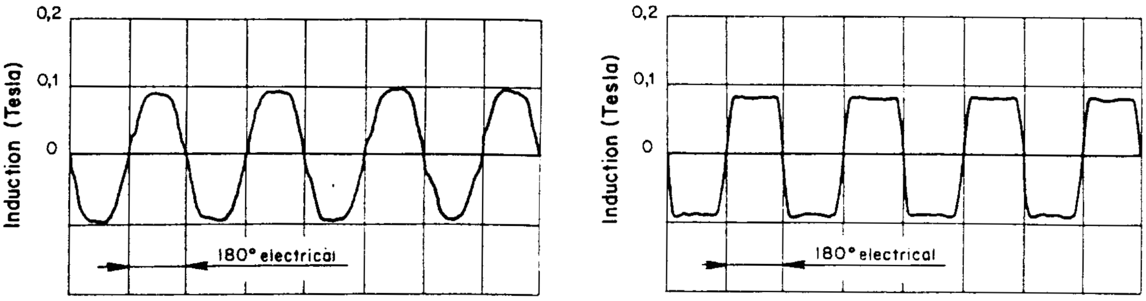

Fig. 5.7: The inside permanent magnet surface radial induction after magnetization, curves for two different permanent magnet rings that have been magnetized by different magnetizers.

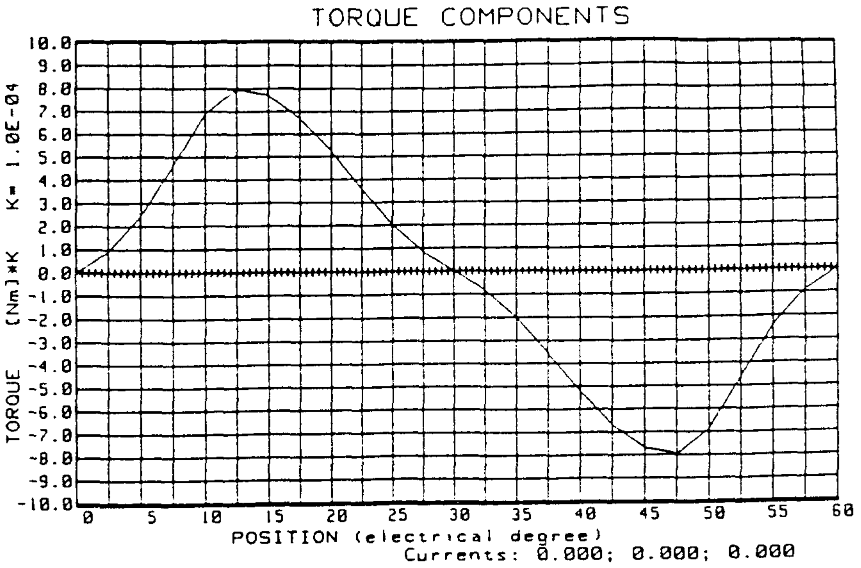

Fig. 5.8: The detent torque T_d including the effect of the gradient between two consecutive poles.

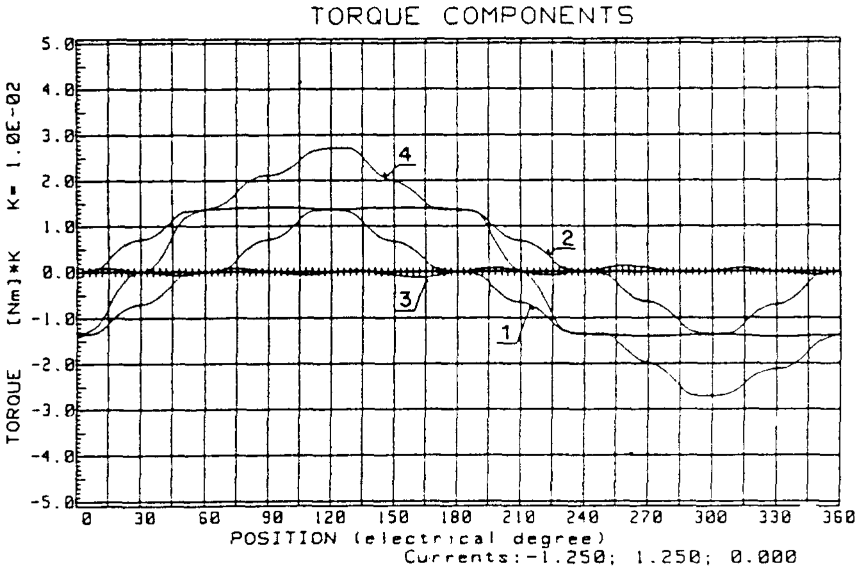

Fig. 5.9: The total torque including the effect of the gradient between two consecutive poles.

1: mutual torque between the first phase and the permanent magnet

2: mutual torque between the second phase and the permanent magnet

3: detent torque

4: total torque

The spindle DC motor treated in [5] has three Hall-sensors placed in the stator slot openings. Now three larger slot openings appear, spaced 120° from each other. The motor no longer possesses a complete symmetry, see Fig. 5.10.
The simulated detent torque when the larger slot openings are taken into account is shown in Fig. 5.11. Although (5.1) is no longer valid, the following equation is still satisfied:

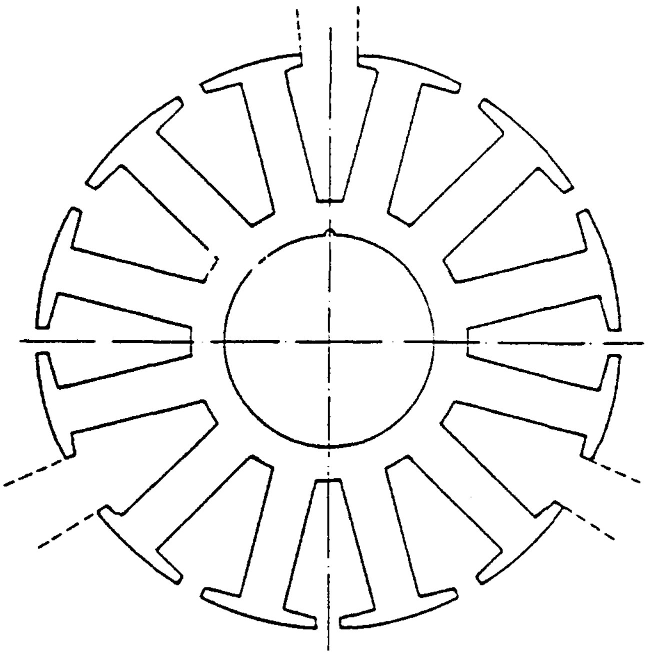

Fig. 5.10: The stator lamination.

$$\int_{0}^{60^\circ} T_d d\alpha = 0 \tag{5.7}$$

As a result of the asymmetry introduced by the larger slot openings, radial forces could appear. Figure 5.12 shows the calculated radial force for the spindle DC motor (not energized) considered in [5]. The total torque for this motor in a two-phases-on-mode is shown in Fig.5.13. When comparing the curves from Fig.5.13 with the curves from Fig.5.5 the influence of the three larger slot openings on the total torque and its components is noticable.

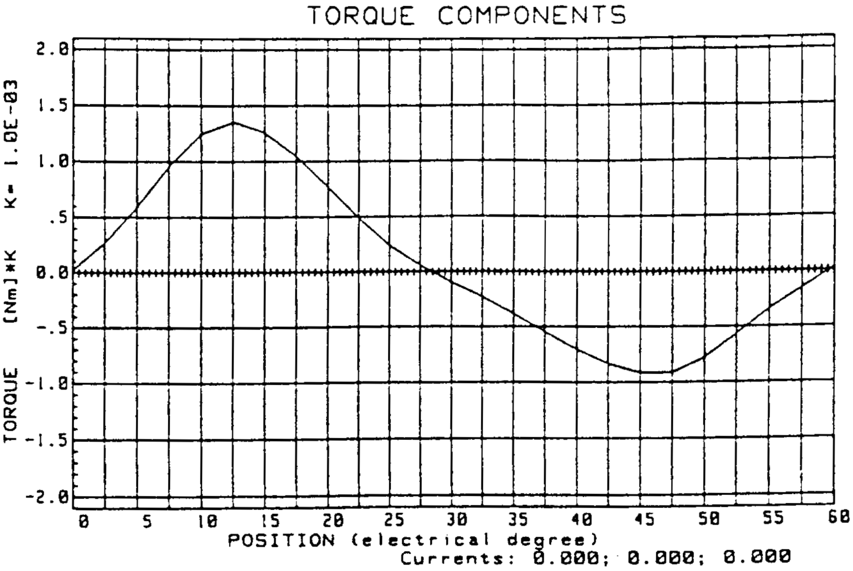

Fig. 5.11: The detent torque including the effect of three larger slot openings.

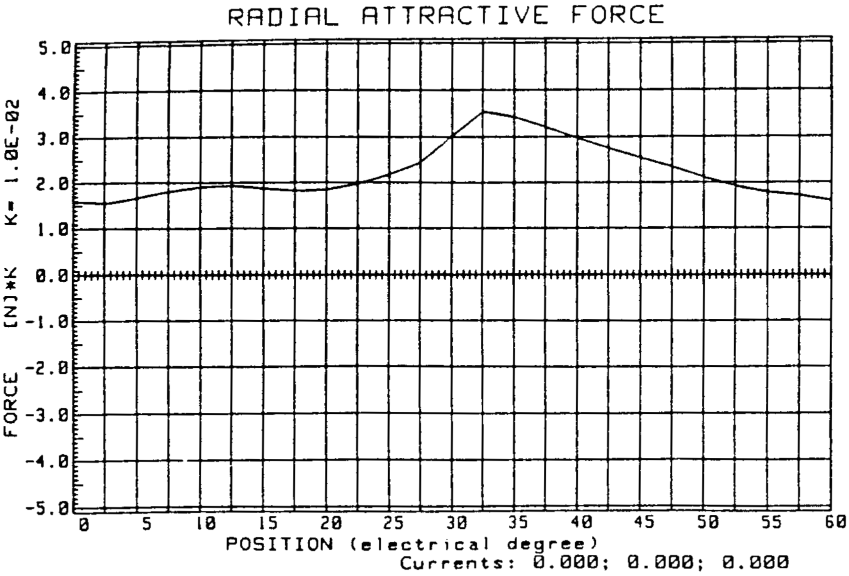

Fig. 5.12: The radial attractive force.

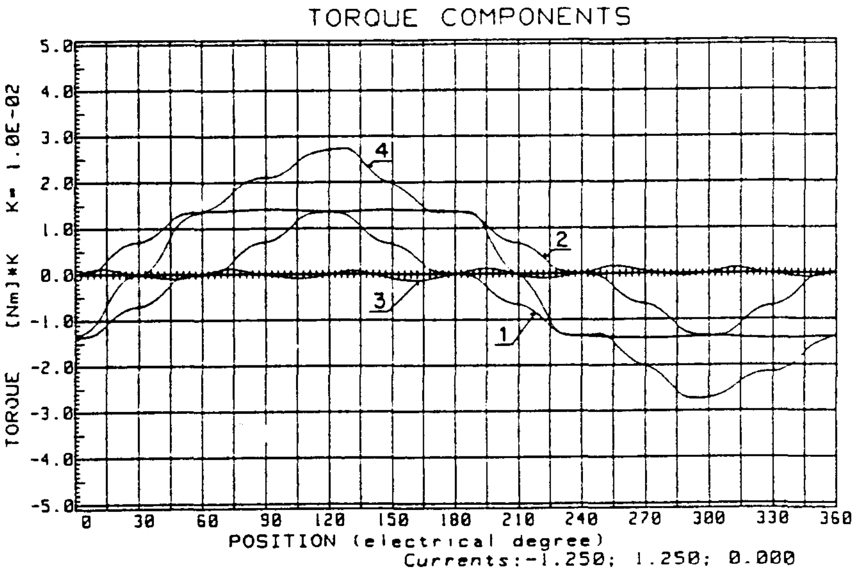

Fig. 5.13: Total torque and torque components with the influence of three larger slot openings.
1: mutual torque between the first phase and the permanent magnet
2: mutual torque between the second phase and the permanent magnet
3: detent torque
4: total torque

5.2.4 Important Magnetic Changes

When considering the permanent magnet MMF distribution in the airgap, it appears that three important changes could occur in:

1. permanent magnet pole pitches
2. level of permanent magnet pole magnetization
3. gradient of the MMF between two consecutive poles.

Variation in permanent magnet pole pitches.
Based on the measurements in [5], it appears that the permanent magnet pole pitch τ_{pp} is not constant. The effect of a variation in pole pitch has been studied in [5]. The pole pitches were defined as follows:

Pole	1	2	3	4	5	6	7	8
τ_{pp}	182°	178°	182°	178°	182°	178°	182°	178°

Table 5.1: The pole pitch distribution

This approach correspondes to a ±1.1% variation of the pole pitch. The detent torque for this table of the pole pitch distribution is shown in Fig. 5.14. According to [5] it can be shown that the period becomes 120 electrical degrees. A typical motor having varying pole pitches is shown in Fig. 5.15. The period of the detent torque is 120° (electrical).

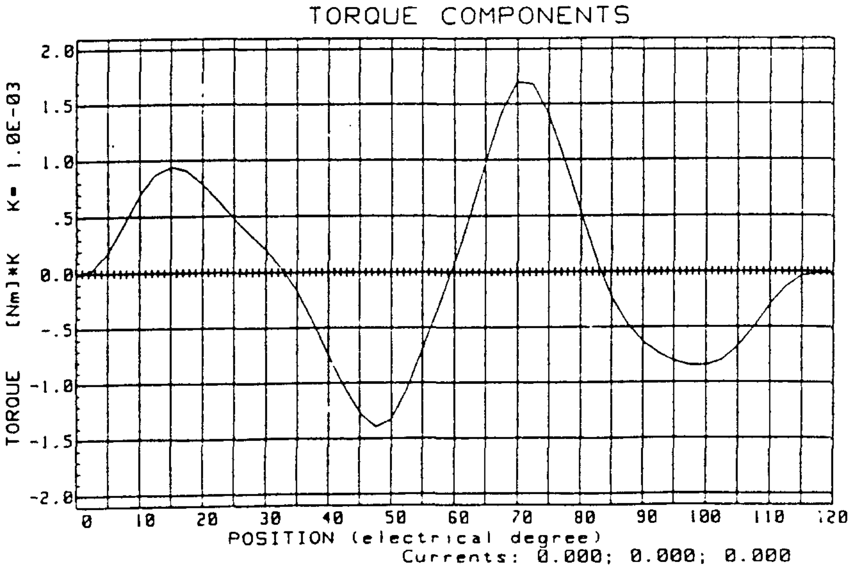

Fig. 5.14: The detent torque when varying permanent magnet pole pitches are used.

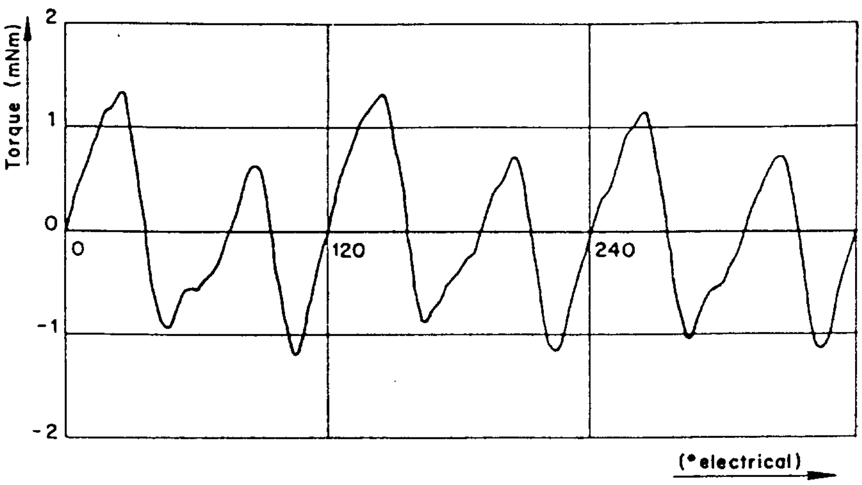

Fig. 5.15: A typical motor with varying pole pitches.

Variation in permanent magnet pole magnetization levels.
It could happen that the level of magnetization is not equal for each pole due to:

- eccentricity of the permanent magnet in the magnetizer
- non-constant airgap in the magnetizer.

These two possibilities were studied in [5] by defining the following situation:

Pole	1	2	3	4	5	6	7	8
Magnetisation factor	1.025	0.975	1.025	0.975	1.025	0.975	1.025	0.975

Table 5.2: The distribution of the level of magnetization

This approach correspondes to a ±2.5% variation of the magnetization level. The detent torque corresponding with this table is shown in Fig. 5.16. As can be seen the period of the detent torque does not change. Only the magnitude of the detent torque changes, see Fig. 5.11.

Variation in stator tooth pitches.
The variation in stator tooth pitches is mainly due to the stator lamination tolerances. These tolerances are usually very low and consequently are not determinant on the changes in motor performances. Varying stator tooth pitches are applied by some manufacturers in order to reduce the detent torque. To achieve this the stator tooth pitches are chosen larger than the permanent magnet tooth pitches. This means that there are big and small stator teeth.

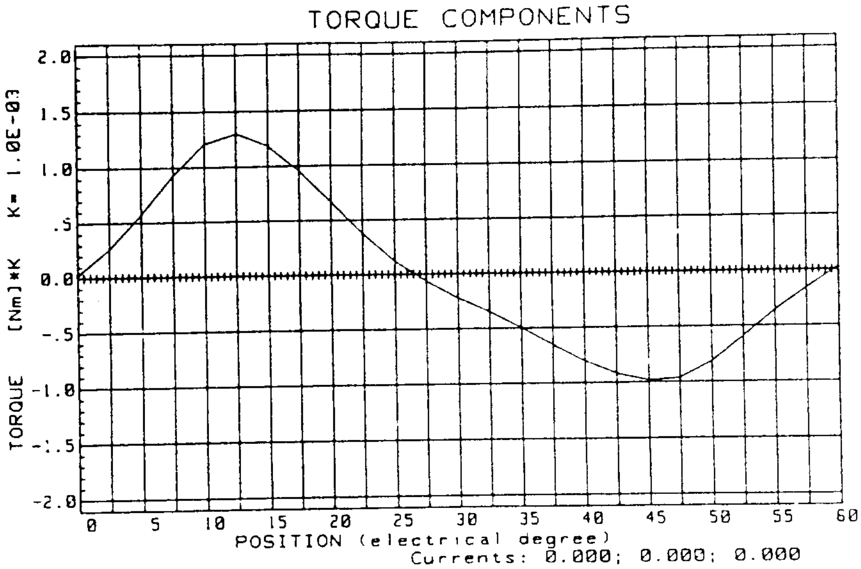

Fig. 5.16: The detent torque when varying permanent magnet magnetization levels are present.

5.3 The Spindle DC Motor with an Axial Airgap.

Because of the design of the spindle DC motor, there is no detent torque. This can be illustrated with Fig. 5.17 which shows the top view of the motor configuration with an axial airgap used in the simulation in [6]. In this figure R_a is defined as the outside radius of a coil.

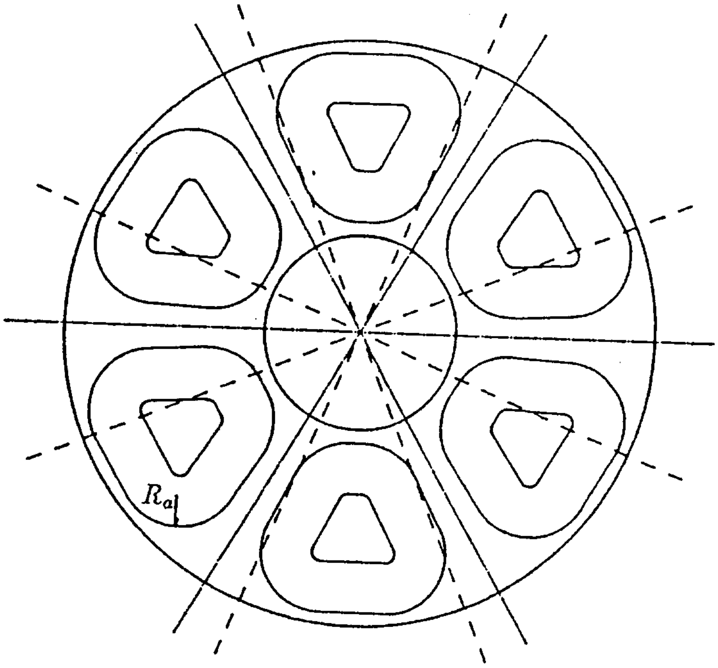

Fig. 5.17: The motor configuration (top view) of the spindle DC motor with an axial airgap.

5.3.1 The Symmetric Motor

In case of the spindle DC motor with axial airgap simulation and analysis in [6] have shown that the distribution of the MMF does not vary significantly along the radius of the motor. Therefore the MMF has been determined for the average radius defined by the outer diameter and the inner diameter of the permanent magnet. The computing method presented in appendix A was used in [6] to determine:

- *The permanent magnet MMF distribution.* The simulated MMF of the permanent magnet is shown in Fig. 5.18. Fig. 5.19 represents the induction of the permanent magnet, measured on the surface of the permanent magnet.
- *Inductances.* The calculation of the inductance without current shows the leakage flux in the motor. In [5] the following values were determined:
  self inductances : 0.642 mH
  mutual inductances : −0.147 mH
  inductance of 2 phases in series, direct current : 1.58 mH
  measured at $1kHz$: 1.7 mH

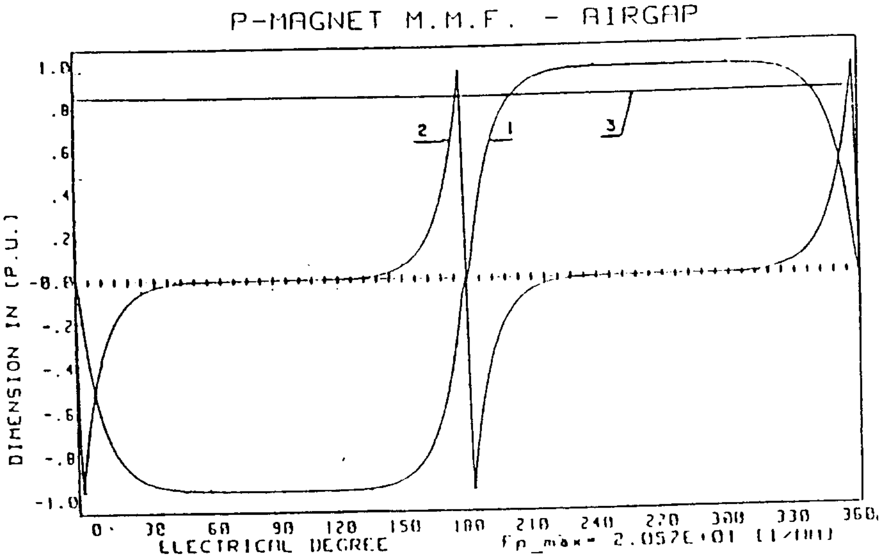

Fig. 5.18: The permanent magnet MMF distribution.
1: MMF 2: gradient of the MMF
3: average value of the abs(MMF)

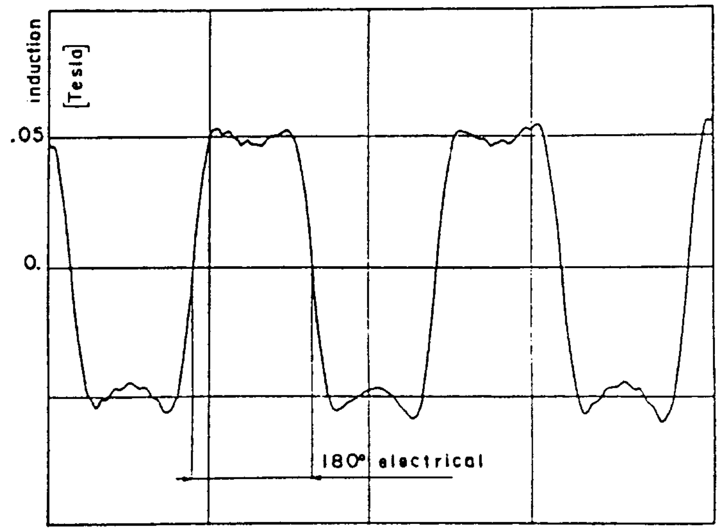

Fig. 5.19: The permanent magnet axial induction after magnetization.

- *The torque components.* As has been said this type of spindle DC motor has no detent torque. The major components of torque are the mutual torques that are produced by a phase and the permanent magnet. The mode used in simulation is a two-phases-on-mode (120° electrical). The simulated torque T_e is shown in Fig. 5.20. The measured torque T_e is shown in Fig. 5.21.

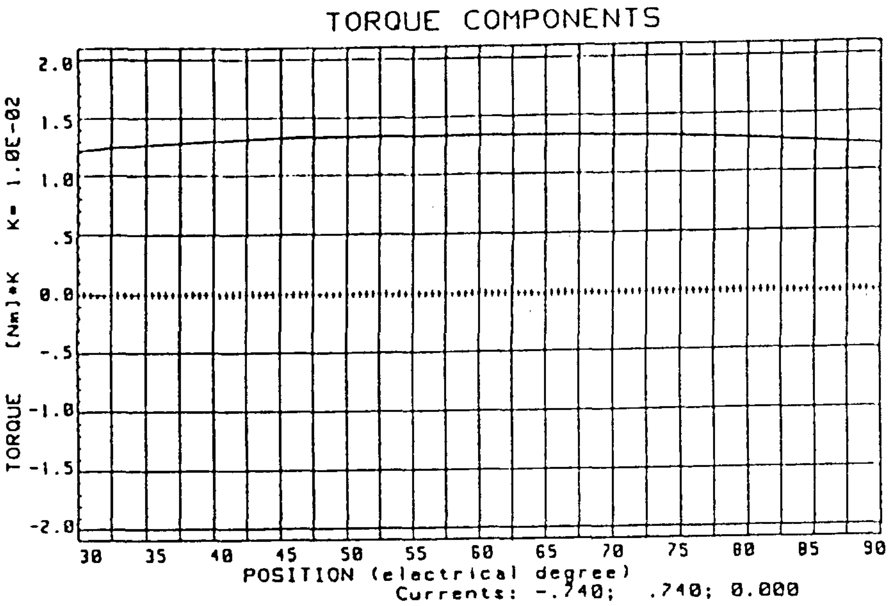

Fig. 5.20: Simulated torque (nominal).
1: torque at 30° and 90° = starting torque
2: torque at 60° = peak torque

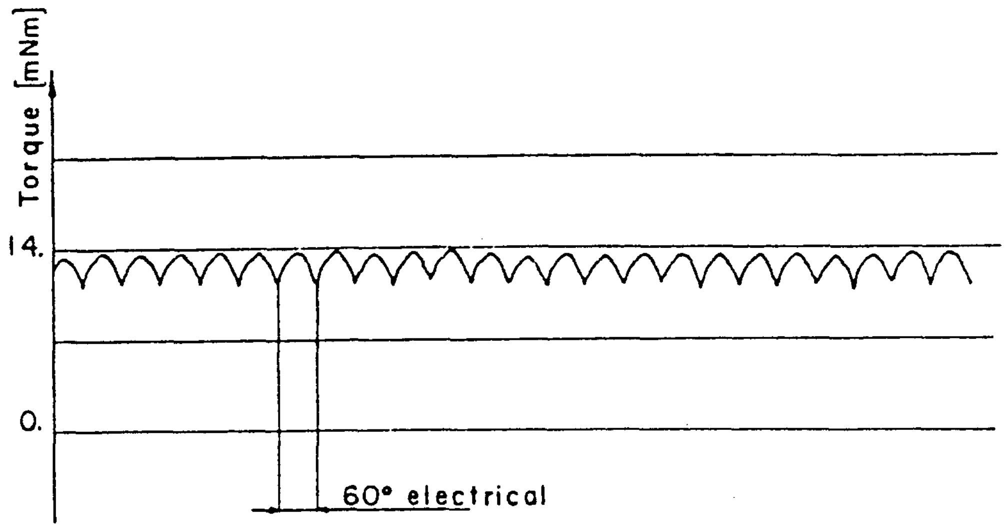

Fig. 5.21: Measured torque, two phases on mode, $0.74A/phase$.

5.3.2 The Real Motor

The real motor will be depending on tolerances and on the admissible variation of electrical and magnetic parameters. The major changes which can occur for a spindle DC motor with an axial airgap are:

- airgap variation
- variation in the total surface of the coil
- eccentricity of coils
- variation in the distribution of the permanent magnet MMF due to the influence of the magnetizer geometry
- varying levels of the permanent magnet pole magnetization.

Airgap variation.
Fig. 5.2 shows that a cummulative effect of the design and assembly tolerances will have a direct effect on the airgap. The possibility of large variations in the airgap value is related to the concept of the motor. This means that the design of the motor must be based on the worst airgap case.

The worst airgap case can be chosen as the reference airgap. Table 5.3 shows some simulated results for various airgaps. The results from Table 5.3 show that the level of saturation is very low.

Airgap	Maximum torque	Starting torque	Inductance
[p.u.]	[p.u.]	[p.u.]	[p.u.]
0.65	1.28	1.28	1.28
0.75	1.17	1.17	1.17
0.89	1.07	1.07	1.07
1	1	1	1

Table 5.3: Simulated results for variation in airgaps.

Total coil surfaces.
The winding geometry for the spindle DC motor with axial airgap can be seen in Fig. 5.17. The internal surface of a coil is given by a tool which has the shape of the internal surface. A winder will wind around this tool and add turns of wire. The outside geometry of the coil will be given by the wire diameter, the number of turns and the tension applied to the wire. It seems reasonable to assume that the total coil surface can consequently vary.

In [6] two cases of variation in coil surfaces are treated. For the first case it is assumed that all the coil surfaces have the same total surface. Variations of the radius R_a, as defined in Fig. 5.17, are studied. The top views of several coil configurations can be seen in Fig. 5.22. Table 5.4 shows some of the results for the configurations of Fig. 5.22.

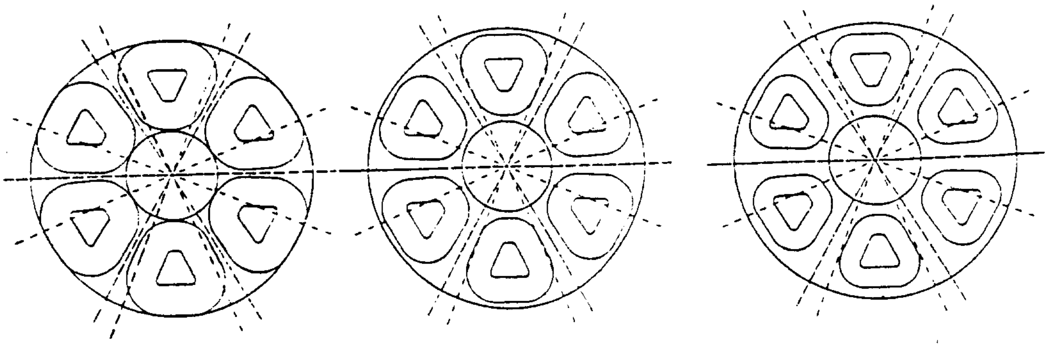

Fig. 5.22: Top view several coil surfaces, all coils same total surface.
1: $R_a = 1.17$ [p.u.] 2: $R_a = 1$ [p.u.], nominal
3: $R_a = 0.85$ [p.u.]

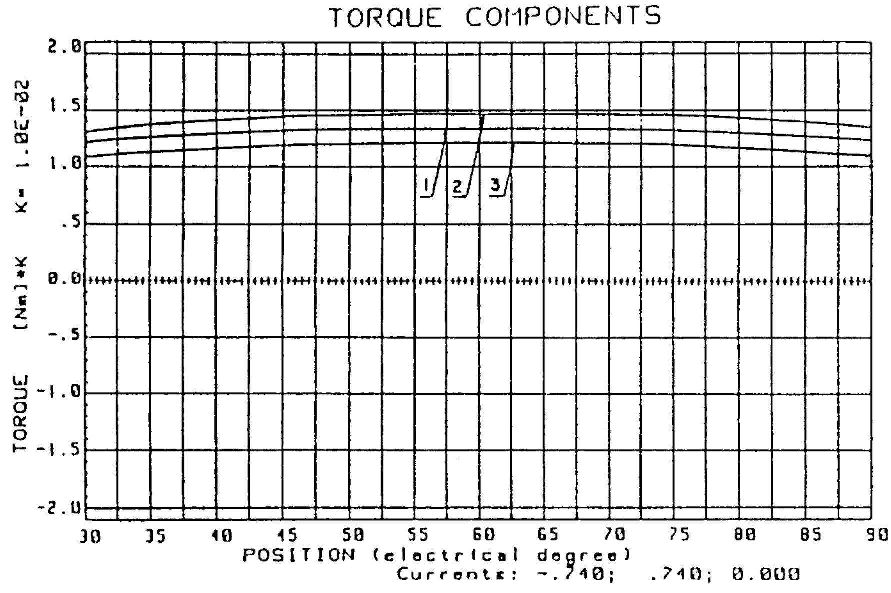

Fig. 5.23: Simulated results for the torque for several coil surfaces.
1: $R_a = 1$ [p.u.], nominal 2: $R_a = 1.17$ [p.u.]
3: $R_a = 0.85$ [p.u.]

Outside radius of the coil	Maximum torque	Starting torque	Inductance
[p.u.]	[p.u.]	[p.u.]	[p.u.]
1.17	1.1	1	1
1	1	1	1
0.85	0.9	0.89	0.86

Table 5.4: Results for several coil surfaces, all coils same total surface.

In the second case one surface coil is assumed to be bigger than the others. This results in asymmetry of the geometry of the motor, as can be seen in Fig. 5.24. The whole motor must be taken into account in order to simulate this configuration. The simulated torque for this case can be seen in Fig. 5.25. Table 5.5 shows the results for the configuration of Fig. 5.24.

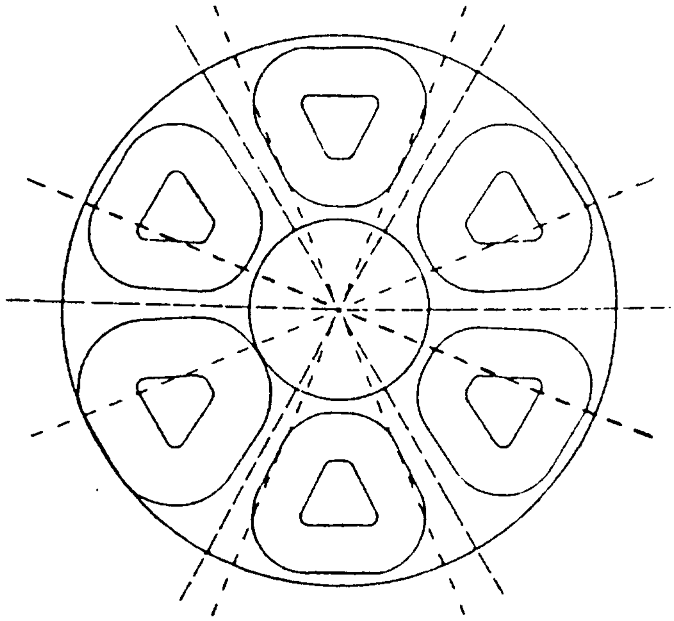

Fig. 5.24: Top view motor, one coil with bigger surface ($R_a = 1.17$ [p.u.]).

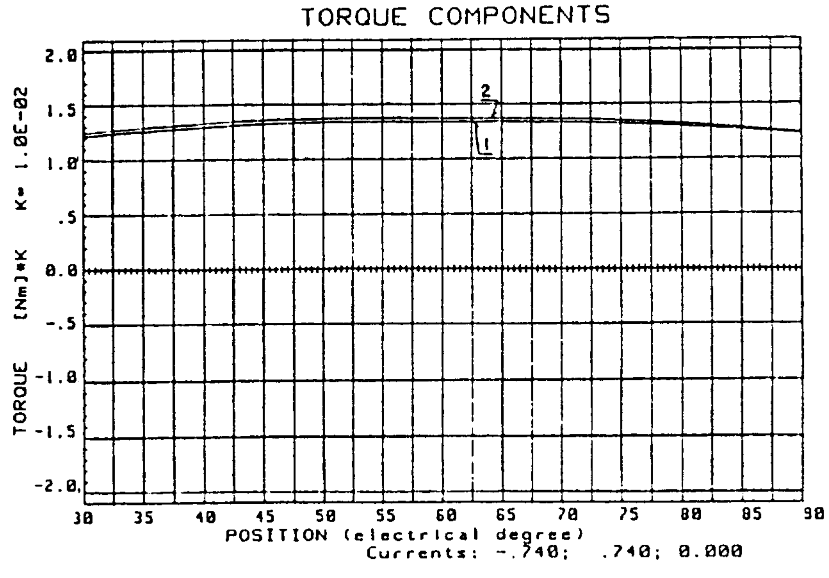

Fig. 5.25: Simulated torque for a motor with one coil with a bigger surface.
1: nominal torque, $R_a = 1$ [p.u.]
2: $R_a = 1.17$ [p.u.]

Outside radius of the coil	Maximum torque	Starting torque	Inductance
[p.u.]	[p.u.]	[p.u.]	[p.u.]
1.17	1.025	1.027	1.02
1	1	1	1

Table 5.5: Results for the simulated torque, one coil with radius (R_a = 1.17 [p.u.]).

Eccentricity of the coil position.

A variation that is also possible during production is the respective position of the coils and the possible eccentricity of this position. The top view from Fig. 5.26 shows one coil with an eccentricity of 5% versus the nominal position. Fig. 5.27 shows the torque obtained from simulation. A small difference occurs between the nominal torque and the torque of this configuration. Table 5.6 shows some results for this configuration.

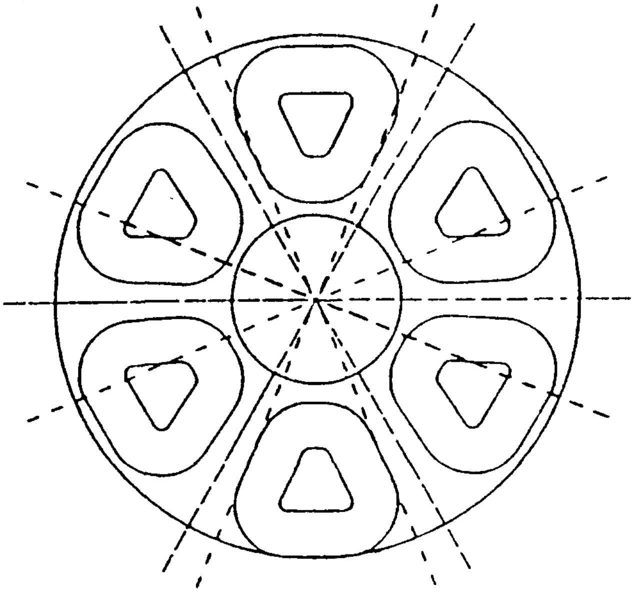

Fig. 5.26: Top view motor, one coil with 5% eccentricity.

Eccentricity	Maximum torque	Starting torque	Inductance
[p.u.]	[p.u.]	[p.u.]	[p.u.]
1.05	1.013	1.007	1
1	1	1	1

Table 5.6: Results for the simulated torque, one coil with an eccentricity of 5%.

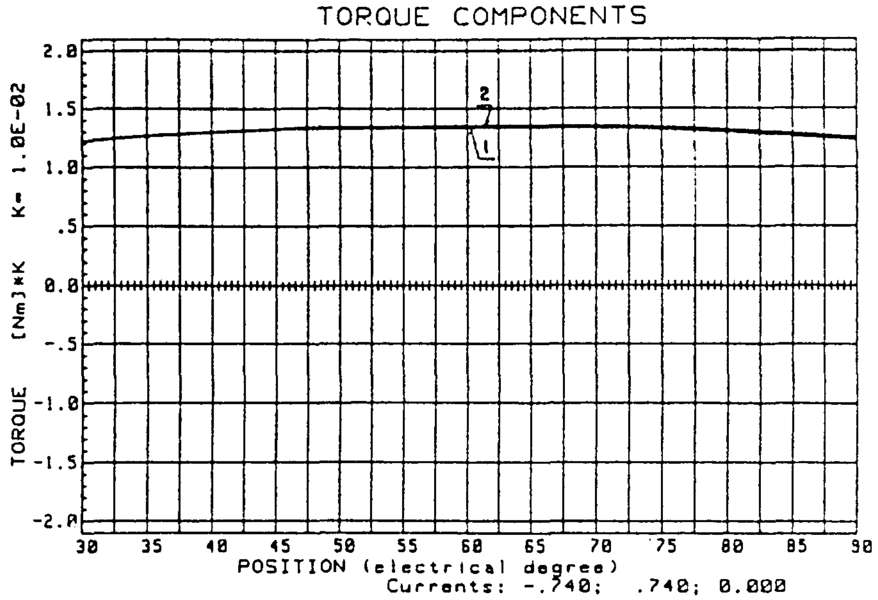

Fig. 5.27: Simulated torque for a motor with one coil with 5% eccentricity.
1: nominal torque eccentricity = 1 [p.u.]
2: eccentricity = 1.05 [p.u.]

Variation in permanent magnet pole pitches.
Based on the measurements in [6] it appears that the permanent magnet pole pitch τ_{pp} is not constant from one pole to the other. For a configuration with eight poles the nominal pole pitch τ_{pp} is 180° electrical. To study the effect of such a variation the situation as defined in Table 5.1 is used . The permanent magnet MMF with a slight difference compared to the nominal distribution shown in Fig. 5.18 is represented in Fig. 5.28. The torque for this configuration is shown in Fig. 5.29. The results for this pole pitch variation can be seen in Table 5.7.

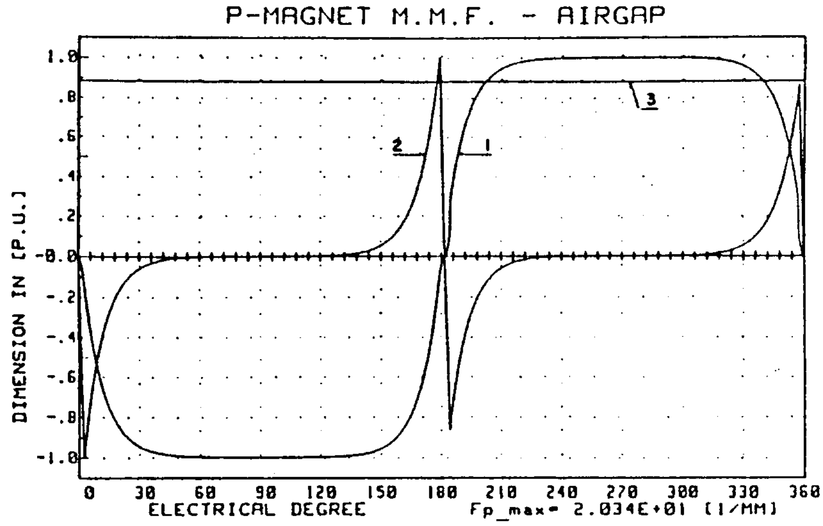

Fig. 5.28: The permanent magnet MMF distribution in case of variation in pole pitches.

1: MMF 2: gradient of the MMF
3: average value of the abs(MMF)

Variable pole pitches	Maximum torque	Starting torque	Inductance
[p.u.]	[p.u.]	[p.u.]	[p.u.]
± 1.1	0.97	0.97	1
1	1	1	1

Table 5.7: Results of a variation in pole pitches.

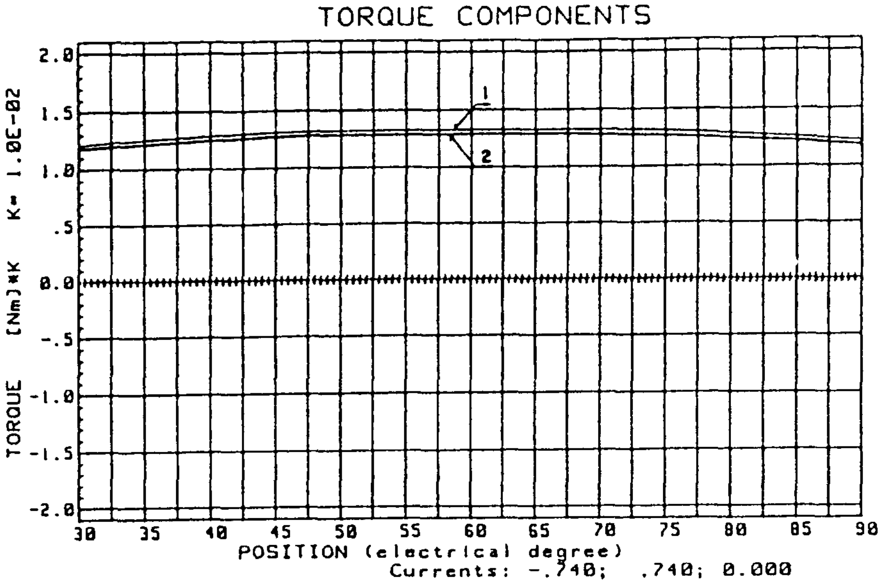

Fig. 5.29: Simulated torque for a motor with a variation in permanent magnet pole pitches
1: nominal torque, $\tau_{pp} = 1$ [p.u.]
2: $\tau_{pp} = 1.1; 0.9$ [p.u.]

Variation in the levels of permanent magnet magnetisation.
It is possible that the permanent magnet magnetisation is not equal for each pole. This possibility the situation as defined in Table 5.2 is used. The simulated torque is represented in Fig. 5.30. The main characteristics of the torque can be seen in Table 5.8.

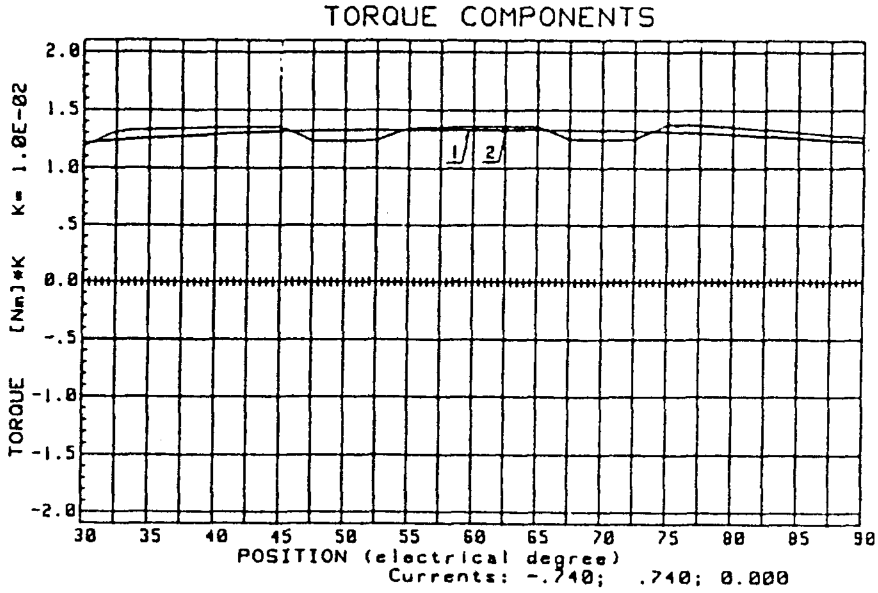

Fig. 5.30: Torque for several levels of magnetisation
1: nominal magnetization level = 1 [p.u.]
2: magnetization level = 1 ± 0.025 [p.u.]

Magnetisation level	Maximum torque	Starting torque	Inductance
[p.u.]	[p.u.]	[p.u.]	[p.u.]
1 ± 0.025	1.024	[0.98, 1.04]	1
1	1	1	1

Table 5.8: Results for the configuration with several permanent magnet pole magnetisation levels.

Chapter 6

Conclusions

6.1 Conclusions

In this report the results are presented of a literature–survey concerning the analysis of the dynamic behaviour of permanent magnet brushless DC motors (PM BDCM). In particular, attention was paid to the influence of various production tolerances on the performance of a PM BDCM.

Several methods for modelling the behaviour of a PM BDCM can be found in literature. Some of these methods include the modelling of parasitic effects like magnetic saturation and iron losses. It is thought that the models found in literature are able to produce accurate simulation results if the motor parameters are known. However, the major problem seems to be how to obtain these model parameters from measurements on the considered motor.

Most models of brushless motors in literature describe nominal models. A nominal motor model can be considered as a theoretical motor where geometry, electrical parameters and magnetic parameters are symmetric. Only a very few articles mention the effects of variations in electrical, magnetic and mechanical parameters on the performance of a brushless motor. In this report a model was presented that offers a lot of freedom in specifying the variation of motor parameters. These variations can have a strong influence on the torque of the motor. According to the literature found on this subject, the most important changes are variations in the level of magnetisation of the permanent magnet poles and variation in coil surfaces.

In literature nothing has been found on any of the following subjects:

- How does the switching in the motor driver circuit affect the shape of the phase currents?
- What is the effect of the presence of parasitic capacitances on the motor performance?
- What is the influence of additional damping circuits like snubbers (a resistance and capacitance combination in parallel with the motor phases) on motor performance?

The final aim of the project will be to obtain a model of a brushless motor that contains all relevant effects needed for the design of a motor controller. In literature no motivation was found if the modelling of switching effects, parasitic capacitances and damping components is useful or not.

Appendix A

Torque and Inductance Determination

The method that will be presented in this appendix is based on the references [2, 4, 5]. This method can support the designer of BDCMs by taking into account the geometrical dimensions, material characteristics, electrical parameters and possible deviations from specifications.

The performance of a BDCM can be determined once the torque and inductance characteristics and the winding resistance are known. The approach presented here is based on dividing the electro-mechanical system into small homogeneous parts where the induction is assumed to be constant. The method permits a simple optimisation of static performances and gives useful parameters that can be used for dynamic analysis. This method can be seen as a 'lumped-parameter' model in contrast to the more detailed approach of the finite element method. The finite element method allows taking into account all parameters of a motor. However, this method is very difficult to apply when the dynamic performance of a motor has to be determined [2].

The following five assumptions were made, [2, 4]:

- The magnetic energy and coenergy (see Section 3.1) of the system are assumed to be state functions of the final values of the phase currents. Hysteresis can not be taken into account.
- The magnetic material is considered homogeneous in all directions.
- The saturable parts of the motor are divided into into small elements where the induction is defined as homogeneous.
- The airgap flux is divided into small tubes of flux of constant area. The permeance (see Section A.2.1) of such a tube in the airgap is considered to be a function of the rotor position only.
- The permanent magnets can be replaced by an equivalent magnetic scheme depending only on the magnets characteristics and geometry.

A.1 A summary of steps in performance determination

The determination of the motor performance is divided into five steps.

1. *Determination of the equivalent magnetic circuit*:
   the previous assumptions allow defining a network of permeances which represent different parts of the motor (rotor, stator, airgap permanent magnets). Each motor winding is represented by a source of magnetic potential. The permanent magnets can also be presented by a magnetic equivalent scheme. The equivalent magnetic scheme for a spindle DC motor is shown in Fig. A.1.

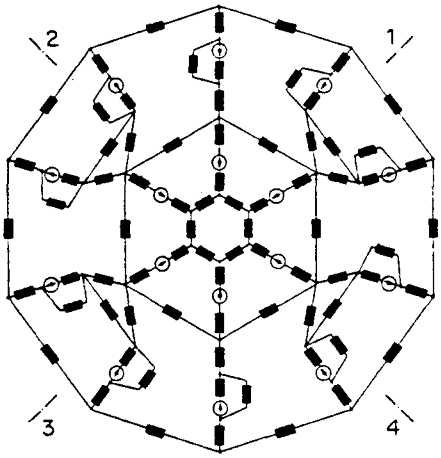

Fig. A.1: The equivalent magnetic scheme for a spindle DC motor

2. *The determination of the oriented graph associated with the equivalent magnetic structure*:
   the oriented graph is determined in order to define the positive direction of the flux in each branch of the equivalent magnetic scheme. The oriented graph for a spindle DC motor is shown in Fig. A.2.

3. *The determination of the flux equations*:
   after the oriented graph has been determined, the flux equations for each branch of the magnetic circuit can be expressed.

4. *The determination of the torque*:
   the torque that is produced by the motor is now determined, taking into account the saturation effects.

5. *The determination of the inductances and the incremental inductances*:
   average inductances and incremental inductances (differential inductances) are calculated. The complete static performance is now determined.

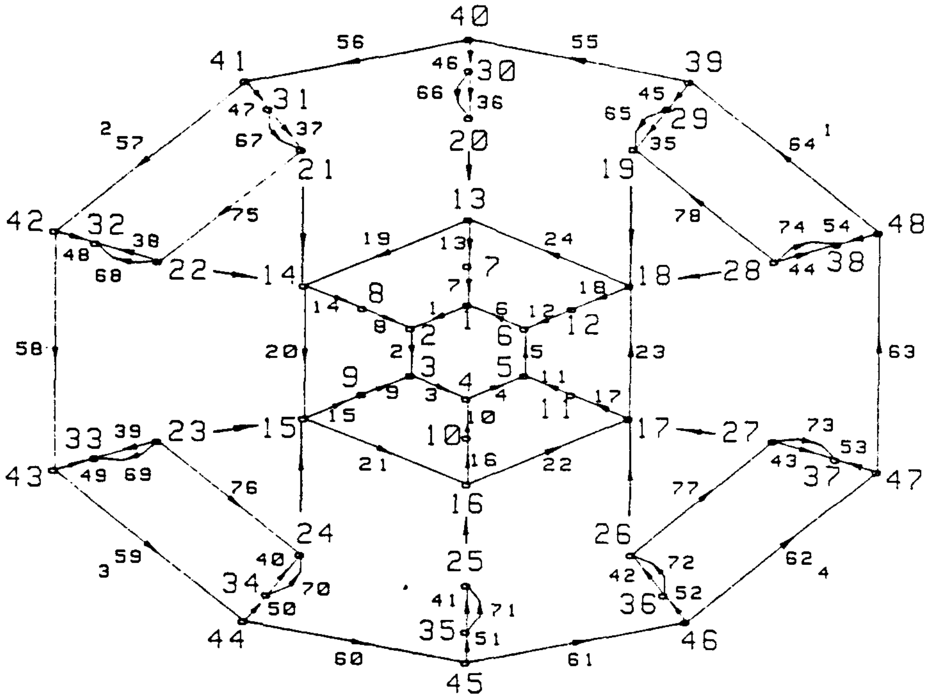
40
56
55
41
46
30
39
31
66
36
45
47
37
65
29
2
57
67
20
35
64
1
21
19
42
32
75
13
78
74
54
48
38
19
13
24
48
22
14
7
18
28
44
38
68
8
7
18
14
1
6
12
12
8
2
6
58
20
2
5
23
63
9
3
4
5
11
9
3
4
17
33
39
23
15
15
10
11
17
27
73
43
49
69
10
53
21
16
22
43
37
47
76
16
77
24
26
59
3
40
25
62
34
70
41
42
72
4
50
71
36
52
35
51
44
46
60
61
45

Fig. A.2: The oriented graph for a spindle DC motor

A.2 The equivalent magnetic circuit

The equivalent magnetic circuit is defined by all the parts j of the motor where the induction can be considered as homogeneous. The geometry of a typical three phases spindle DC motor is shown in Fig. A.3. It has eight permanent magnets at the rotor and twelve stator teeth on which the phase windings are wound.

The equivalent circuit of the spindle DC motor is shown in Fig. A.1. Fig. A.2 shows the oriented graph which is associated with the scheme of Fig. A.1. As shown in Fig. A.2, each branch of the permanent magnetic scheme represents a particular part of the motor.

- branches 1 to 6 characterize the stator yoke
- branches 7 to 12 characterize the stator teeth
- branches 13 to 18 characterize the stator tooth feet
- branches 19 to 24 characterize the tooth to tooth leakage flux
- branches 25 to 34 characterize the airgap
- branches 35 to 44 characterize the rotor permanent magnets
- branches 45 to 54 characterize the airgap between rotor permanent magnets and the rotor yoke
- branches 55 to 64 characterize the rotor yoke

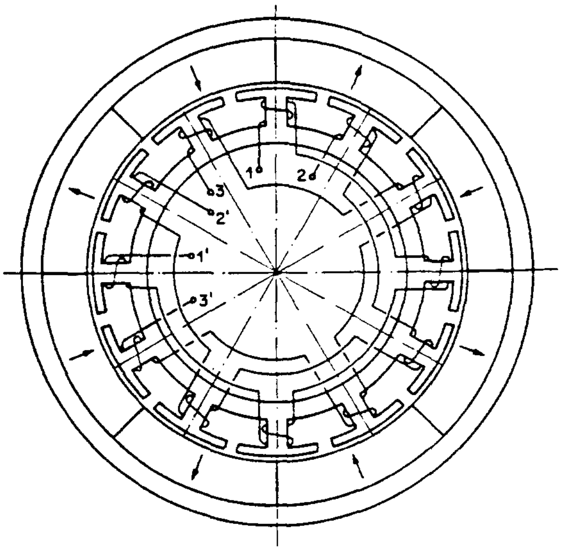

Fig. A.3: A spindle DC motor

- branches 65 to 74 characterize the permanent magnet leakage flux
- branches 75 to 78 characterize the permanent magnet to permanent magnet leakage flux

The permeance of saturable parts, the permeance of the airgap and the permanent magnet equivalent scheme will now be discussed more fully.

A.2.1 The permeance of the saturable parts

For a saturable element on the stator or the rotor k the permeance can be defined, according to [4], as:

$$\Upsilon_k = \mu_0 \cdot \mu_k \cdot \frac{A_k}{l_k} \tag{A.1}$$

Υ_k : permeance of element k $[H \text{ (henry)} = \frac{V \cdot s}{A}]$
μ_k : relative permeability of the material (non-linear) [-]
A_k : area of element k $[m^2]$
l_k : length of element k $[m]$.

An average surface and an average length are defined for each saturable element. To apply equation A.1 in practice the relative permeability μ_k must be known. The flux density B_k, and the magnetic field H_k always satisfy:

$$B_k = \mu_0 \cdot \mu_k \cdot H_k \tag{A.2}$$

B_k : the flux density (induction) $[T \text{ (tesla)} = \frac{Wb}{m^2} = \frac{V \cdot s}{m^2}]$
H_k : the magnetic field $[\frac{A}{m}]$.

Because equation A.2 is a non-linear relation (μ_k is non-linear), a numerical approximation of the B–H curve is needed. In [4] the magnetic field H_k is chosen as the variable, so if the magnetic fields are known, the relative permeabilities μ_k are known from equation A.2. Using equation A.1 the permeances Υ_k are also determined.

A.2.2 The permeance of the airgap

We now consider Fig. A.4 which represents the magnetic motoric force MMF of the permanent magnet in the airgap by the function $F(x - \varepsilon)$ and the distribution of the airgap by the function $G(x)$. These two functions have been determined in reference [16].

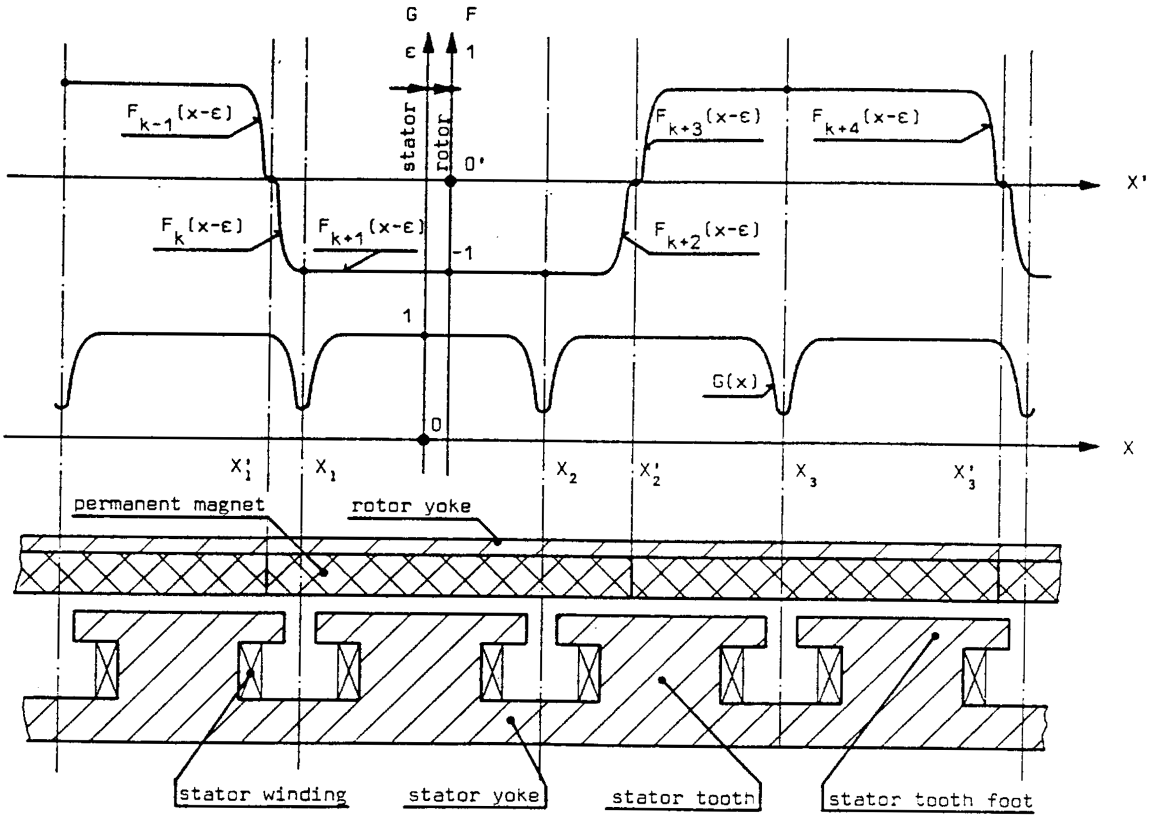
G
F
ε
1
stator
rotor
0'
X'
-1
$F_{k-1}(x-\varepsilon)$
$F_k(x-\varepsilon)$
$F_{k+1}(x-\varepsilon)$
$F_{k+2}(x-\varepsilon)$
$F_{k+3}(x-\varepsilon)$
$F_{k+4}(x-\varepsilon)$
1
G(x)
0
X
X_1'
X_1
X_2
X_2'
X_3
X_3'
permanent magnet
rotor yoke
stator winding
stator yoke
stator tooth
stator tooth foot

Fig. A.4: The MMF in the airgap

The following functions are defined:

$F_k(x - \varepsilon)$: the MMF of the considered permanent magnet in the airgap (per unit) [-]
$G(x)$: the airgap distribution (per unit) [-].

Coordinates used in Fig. A.4:

x : position in the stator referential frame $[m]$
ε : position of the rotor versus the stator $[m]$.
α : angular position of the rotor versus the stator $[rad]$
R_e : equivalent radius of the stator $[m]$.

$$\alpha = \frac{\varepsilon}{R_e} \tag{A.3}$$

The airgap can be described as follows:

$$\frac{1}{\delta(x)} = \frac{G(x)}{\delta_0} \tag{A.4}$$

δ_0 : the nominal airgap $[m]$
$\delta(x)$: the distribution of the airgap expressed in the stator referential frame $[m]$.

According to [4] the MMF of a magnet can be written as:

$$\Theta_k(x, \varepsilon) = \Theta_k(\varepsilon) \cdot F_k(x - \varepsilon) \tag{A.5}$$

$\Theta_k(x - \varepsilon)$: the MMF distribution in the airgap due to a permanent magnet $[A]$
$\Theta_k(\varepsilon)$: the equivalent MMF distribution in the airgap of the considered section $[A]$.

In [16] the permanent magnet distribution function $F_k(x)$ has been determined on the basis of a finite element method. The results were approximated by a hyperbolic function:

$$F_k(x) = \frac{cosh\left[b \cdot (x - \frac{\tau_{pp}}{2})\right] - 1}{cosh\left[b \cdot \frac{\tau_{pp}}{2}\right] - 1} \tag{A.6}$$

τ_{pp} : pole pitch
b : coefficient depended of $\frac{\delta(x)}{\tau_{pp}}$

Figure A.5 shows the accuracy of the approximation and the the finite element results (∘).

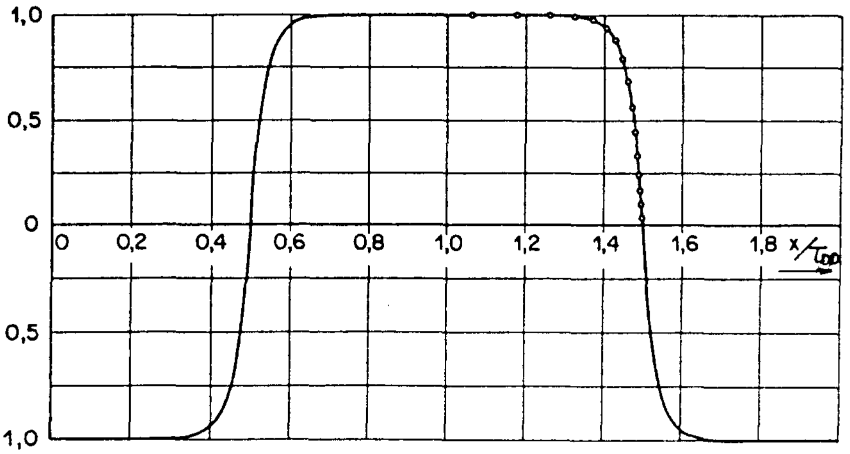

Fig. A.5: The approximation of the permanent magnet MMF function

The gap permeance function $G(x)$ is also described in [16]. Consider Fig. A.6:

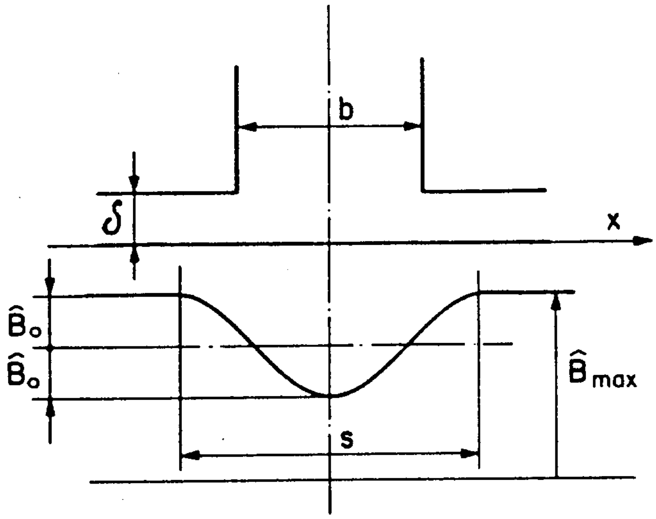

Fig. A.6: The permeance function

β : $\hat{B}_0$ / $\hat{B}_{max}$, relative flux density pertubation
s : pertubation width

The parameters β and s are calculated as follows:

$$u = \frac{b}{2\delta_0} + \sqrt{1 + (\frac{b}{2\delta_0})^2} \tag{A.7}$$

$$\beta = \frac{(1-u)^2}{2(1+u^2)} \tag{A.8}$$

$$\gamma = \frac{4}{\pi}\left[\frac{b}{2\delta_0} arctan(\frac{b}{2\delta_0}) - ln\sqrt{1 + (\frac{b}{2\delta_0})^2}\right] \tag{A.9}$$

$$s = \gamma \cdot \delta_0 \cdot \beta \tag{A.10}$$

The relative permeance function $G(x)$ now becomes:

$$G(x) = 1 - \beta\left[1 + \cos(\frac{2 \cdot \pi \cdot x}{s})\right] \tag{A.11}$$

When considering Fig. A.4 the assumption could be made that the flux density B_k is homogeneous between the limits X_1 and X_2. Then it is possible to express the flux in the airgap as follows:

$$d\Phi_{j+1}(x,\varepsilon) = \frac{\mu_0 \cdot \Theta_{k+1}(x,\varepsilon) \cdot l \cdot dx}{\delta(x)}. \tag{A.12}$$

Here l is the useful length of the motor $[m]$. From equation A.5 we know:

$$\Theta_{k+1}(x,\varepsilon) = \Theta_{k+1}(\varepsilon) \cdot F_{k+1}(x-\varepsilon) \tag{A.13}$$

This means that the flux between the limits X_1 and X_2 now can be calculated resulting in:

$$\Phi_{j+1}(\varepsilon) = \frac{\mu_0 \cdot l \cdot \Theta_{k+1}(\varepsilon)}{\delta_0} \int\limits_{X_1}^{X_2} F_{k+1}(x-\varepsilon) \cdot G(x) \cdot dx \tag{A.14}$$

The equivalent permeance Υ_{j+1} of the airgap can now be expressed as:

$$\Upsilon_{j+1}(\varepsilon) = \frac{\Phi_{j+1}(\varepsilon)}{\Theta_{k+1}(\varepsilon)} = \frac{\mu_0 \cdot l}{\delta_0} \int\limits_{X_1}^{X_2} F_{k+1}(x-\varepsilon) \cdot G(x) \cdot dx \tag{A.15}$$

Again considering Fig. A.4 the resulting airgap permeances of the permanent magnet between the limits X_1' and X_2' can be defined as:

$$\Upsilon_j(\varepsilon) = \frac{\mu_0 \cdot l}{\delta_0} \int\limits_{X_1'}^{X_2} F_k(x-\varepsilon) \cdot G(x) \cdot dx \tag{A.16}$$

$$\Upsilon_{j+1}(\varepsilon) = \frac{\mu_0 \cdot l}{\delta_0} \int\limits_{X_1}^{X_2} F_{k+1}(x-\varepsilon) \cdot G(x) \cdot dx \tag{A.17}$$

$$\Upsilon_{j+2}(\varepsilon) = \frac{\mu_0 \cdot l}{\delta_0} \int\limits_{X_2'}^{X_2} F_{k+2}(x-\varepsilon) \cdot G(x) \cdot dx \tag{A.18}$$

The equations A.16, A.17 and A.18 are all functions of the rotor position. Because $G(x)$ is not a function of ε the following equation can be derived:

$$\begin{aligned} \frac{d\Upsilon_j(\varepsilon)}{d\varepsilon} &= \frac{\mu_0 \cdot l}{\delta_0} \left[\int\limits_{X_1'}^{X_1} G(x) \cdot \frac{\delta F_k(x-\varepsilon)}{\delta\varepsilon} \cdot dx + F_k(X_1-\varepsilon) \cdot G(X_1) \cdot \frac{dX_1}{d\varepsilon} \right. \\ &- \left. F_k(X_1'-\varepsilon) \cdot G(X_1') \cdot \frac{dX_1'}{d\varepsilon} \right] \end{aligned} \tag{A.19}$$

For a given rotor position ε the limits where the induction can be considered as homogeneous are defined. When the above expressions are used the airgap permeances and their derivatives versus the rotor position ε can be calculated. Those values can be introduced in the equivalent magnetic scheme.

A.2.3 The permanent magnet equivalent scheme

A permanent magnet can be simulated by introducing an internal source of MMF and an equivalent permeance function of the B-H curve and the geometry of the permanent magnet. Those parts where the equivalent MMF in the airgap is constant are considered for the same permanent magnet. Again considering Fig. A.4 and more particularly the permanent magnet defined by the limits X_1' and X_2', it is assumed that the equivalent airgap MMF is constant between the limits:

- from X_1' and X_1
- from X_1 and X_2
- from X_2 and X_2'

This means that the permanent magnet defined by the limits X_1' and X_2' must be divided in three parts:

- from X_1' and X_1, first part
- from X_1 and X_2, second part
- from X_2 and X_2', third part

The geometrical permanent magnet surface is defined as

$$A_a = (X_2' - X_1') \cdot l \tag{A.20}$$

Flux is conservative, so the flux in the airgap between the limits X_1' and X_1 is equal to the flux in the permanent magnet. The airgap flux is

$$\Phi_j(\varepsilon) = \frac{\mu_0 \cdot l \cdot \Theta_k(\varepsilon)}{\delta_0} \int_{X_1'}^{X_1} F_k(x-\varepsilon) \cdot G(x) \cdot dx \tag{A.21}$$

so the equivalent surface of the airgap is defined as

$$A_j(\varepsilon) = l \cdot \int_{X_1'}^{X_1} F_k(x-\varepsilon) \cdot G(x) \cdot dx \tag{A.22}$$

and corresponding to the equivalent length of the airgap

$$L_j(\varepsilon) = \delta_0 \tag{A.23}$$

The airgap permeance is defined, see (A.16) as

$$\Upsilon_j(\varepsilon) = \mu_0 \cdot \frac{A_j(\varepsilon)}{L_j(\varepsilon)} \tag{A.24}$$

It seems that the equivalent airgap surface is not a physical surface but a mathematical representation. The equivalent length of the airgap L_j has been chosen to be the nominal airgap δ_0. This equivalent airgap surface cannot represent the equivalent permanent magnet surface.

The choice of the equivalent permanent magnet surface is based on following considerations:

- The MMF distribution in the airgap due to the permanent magnet is not constant, see the functions $F_k(x-\varepsilon)$, $F_{k+1}(x-\varepsilon)$ and $F_{k+2}(x-\varepsilon)$ in Fig. A.4.
- It appears that the equivalent surface where the induction could be considered as homogeneous will be smaller or equal to the corresponding geometrical surface.
- The function $F_k(x-\varepsilon)$ and the function $G(x)$ are independent from each other.

Consider the geometrical surface of the permanent magnet at the level of the airgap $A_{a\delta k}$:

$$A_{a\delta k} = (X_1 - X_1') \cdot l \tag{A.25}$$

The flux that crosses this surface is

$$\Phi_j(\varepsilon) = \int_{X_1'}^{X_1} B_k(x,\varepsilon) \cdot l \cdot dx \tag{A.26}$$

Here $B_k(x,\varepsilon)$ is the flux density at the surface of the permanent magnet. We now define :

$$B_k(x,\varepsilon) = F_k(x-\varepsilon) \cdot \frac{\mu_0 \cdot \mu_d \cdot \Theta_k(\varepsilon)}{\delta_0} \tag{A.27}$$

The equivalent permanent magnet surface for the first part of the magnet can be defined as:

$$A_k(\varepsilon) = \int_{X_1'}^{X_1} F_k(x-\varepsilon) \cdot l \cdot dx. \tag{A.28}$$

Define the function F_{sk} as:

$$F_{sk} = \frac{1}{X_1 - X_1'} \cdot \int_{X_1'}^{X_1} F_k(x-\varepsilon) \cdot dx. \tag{A.29}$$

The function F_{sk} is the average value of the function $F_k(x-\varepsilon)$ between the limits X_1' and X_1. The equivalent surface can now be written as:

$$A_k = F_{sk} \cdot A_{a\delta k}. \tag{A.30}$$

The derivative of the surface versus the rotor position can be written as

$$\frac{dA_k}{d\varepsilon} = \frac{dF_{sk}}{d\varepsilon} \cdot A_{a\delta k} + F_{sk} \cdot \frac{dA_{a\delta k}}{d\varepsilon}. \tag{A.31}$$

Similar mathematical developments can be done for the other two parts of the magnet surface.

Now the equivalent permanent magnet can be defined. Each part will be replaced by the equivalent internal MMF of the permanent magnet and the equivalent permanent magnet permeance. The following expressions for the permeances can be written:

$$\Upsilon_k = \mu_0 \cdot \mu_d \cdot \frac{A_k(\varepsilon)}{l} \tag{A.32}$$

$$\Upsilon_{k+1} = \mu_0 \cdot \mu_d \cdot \frac{A_{k+1}(\varepsilon)}{l} \tag{A.33}$$

$$\Upsilon_{k+2} = \mu_0 \cdot \mu_d \cdot \frac{A_{k+2}(\varepsilon)}{l} \tag{A.34}$$

μ_d : relative permeability of the magnet (non-linear) [-]

According to [2] after one complete turn of the rotor the following relation exists:

$$\Theta_k = \Theta_{k+1} = \Theta_{k+2} \tag{A.35}$$

Θ_k : internal MMF of the permanent magnet, first part
Θ_{k+1} : internal MMF of the permanent magnet, second part
Θ_{k+2} : internal MMF of the permanent magnet, third part

The equivalent magnetic circuit is now completely defined. It is the simplest circuit which takes saturation into account.

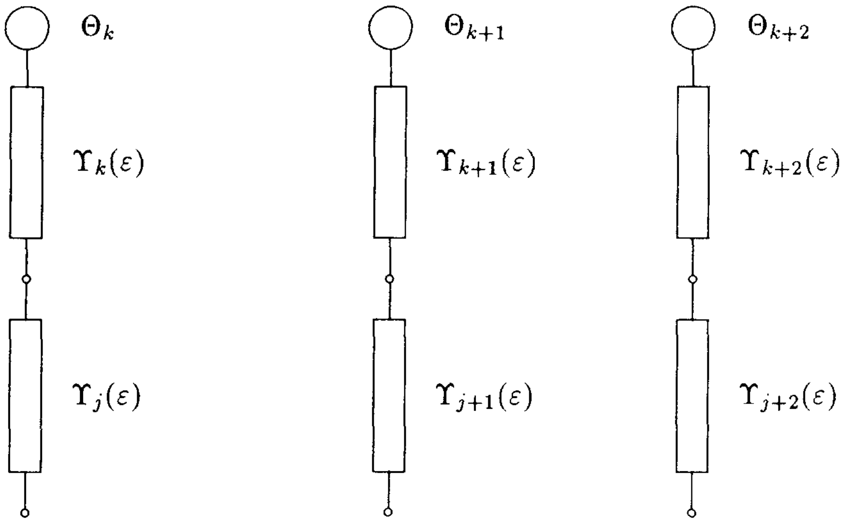
Θ_k
$\Upsilon_k(\varepsilon)$
$\Upsilon_j(\varepsilon)$
Θ_{k+1}
$\Upsilon_{k+1}(\varepsilon)$
$\Upsilon_{j+1}(\varepsilon)$
Θ_{k+2}
$\Upsilon_{k+2}(\varepsilon)$
$\Upsilon_{j+2}(\varepsilon)$

Fig. A.7: The equivalent magnetic circuit for the permanent magnet and the airgap.

A.3 Equations of flux

After the equivalent magnetic circuit has been defined, the equations for the flux can be written. The flux Φ_j of branch j is defined when the angular position α and all magnetic potential forces are known. Therefore Φ_j must be expressed as:

$$\Phi_j = \Phi_j(\alpha, \Theta_1, \Theta_2, \ldots, \Theta_k, \ldots, \Theta_n\ ) \tag{A.36}$$

with $j = 1, 2, \ldots, n$
where

Θ_k : magnetic potential of source k; if branch k has no source then $\Theta_k = 0$;
if branch k represents a permanent magnet, then Θ_k is equal to the internal MMF
n : number of branches of the equivalent magnetic circuit

The equation A.36 can be written as:

$$\Phi_j = \sum_{k=1}^{n} C_{kj} \cdot \Upsilon_{kj} \cdot \Theta_k \qquad j = 1, 2, \ldots, n \tag{A.37}$$

where

Υ_{kj} : permeance between branches k and j
C_{kj} : coupling factor between branches k and j, +1 or -1

For saturable part Φ_j can be expressed as a function of the flux density B_j and the cross sectional area A_j of the element j. The following equation can now be written:

$$\Phi_j = B_j \cdot A_j \tag{A.38}$$

A.4 Determination of the motor torque

It has been shown in [23] that the torque can be expressed as:

$$T_e = \frac{1}{2} \sum_{j=1}^{n'} \frac{d\Upsilon_{\delta j}}{d\alpha} \cdot \Theta_{\delta j}^2 \tag{A.39}$$

Here are :

$\Upsilon_{\delta j}$: airgap permeance j
$\Theta_{\delta j}$: equivalent MMF across the airgap permeance j
n' : number of airgap permeances

From subsection A.2.3 it appears that the equivalent internal permanent magnet permeances are also a function of the rotor position so (A.39) must be completed as follows:

$$T_e = \frac{1}{2} \sum_{j=1}^{n'} \frac{d\Upsilon_{\delta j}}{d\alpha} \cdot \Theta_{\delta j}^2 + \frac{1}{2} \sum_{k=1}^{n''} \frac{d\Upsilon_{\rho k}}{d\alpha} \cdot \Theta_{\rho j}^2 \tag{A.40}$$

Here are :

$\Upsilon_{\rho k}$: equivalent permanent magnet permeance k

$\Theta_{\rho k}$: equivalent MMF across the equivalent permanent magnet permeance k

n'' : number of permanent magnet permeances

Equation (A.40) shows that not only airgap permeances but also equivalent permanent magnet permeances are part of the torque determination. According to [2] this is a key point of this approach.

A.5 Determination of the inductances

The average inductances can be expressed according to [4] as a linear function of the permeances Υ_{ij}:

$$L_{KP} = \sum_{i=1}^{n} \sum_{j=1}^{n} S_{KP,ij} \cdot C_{ij} \cdot \Upsilon_{ij} \tag{A.41}$$

with:

$K = 1, 2, \ldots, m$

$P = 1, 2, \ldots, m$

where:

m : number of phases

$S_{KP,ij}$: coupling factor between phase K and phase P in relation with branch i and branch j of the equivalent magnetic scheme.
$S_{KP,ij} = -N_K N_P$, negative coupling.
$S_{KP,ij} = 0$, non coupling.
$S_{KP,ij} = N_K N_P$, positive coupling.

N_K : number of winding turns of branch i or j belonging to phase K

N_P : number of winding turns of branch i or j belonging to phase P

m : number of phases

C_{ij} : coupling factor between branch i and branch j of the equivalent magnetic scheme (+1 or -1).

Υ_{ij} : permeance between the phases i and j

The incremental (or differential) inductance L'_{KP} is defined in [5] as:

$$L'_{KP} = L_{KP} + \sum_{y=1}^{m} \frac{\delta L_{Ky}}{\delta i_y} \cdot i_y \tag{A.42}$$

where i_y is the current in phase y.

Appendix B

Spindle DC motor

B.1 Spindle DC motor with radial gap

Rotor:

Outside diameter	: 71.9	[mm]
Inside diameter	: 69.9	[mm]
Material	: steel	

Permanent magnet:

Outside diameter	: 69.9	[mm]
Inside diameter	: 60.8	[mm]
Number of poles	: 8	
Material	: ferrite	

Stator:

Outside diameter	: 60.1	[mm]
Number of teeth	: 12	
Useful length	: 2.28	[mm]
Thickness	: ?	[mm]
Material lamination	: insulated electrical	

Phases:

Number of phases	: 3
Configuration	: star

Dynamics:

Nominal speed	: 3600	[rpm]

B.2 Spindle DC motor with axial gap

Rotor:

Outside diameter	: 69.3	[mm]
Inside diameter	: 22.6	[mm]
Thickness	: 1	[mm]
Material	: steel	

Permanent magnet:

Outside diameter	: 69.3	[mm]
Inside diameter	: 22.6	[mm]
Number of poles	: 8	
Thickness	: 1.52	[mm]
Material	: plastic ferrite	

Stator return path:

Outside diameter	: 69.3	[mm]
Inside diameter	: 22.6	[mm]
Thickness	: 1.52	[mm]
Material	: steel	

Phases:

Number of phases	: 3
Number of coils	: 6
Configuration	: star

Dynamics:

Nominal speed	: 3600	[rpm]

Bibliography

[1] J.Bahlmann, *A Full-wave Drive IC based on the Back-EMF Sensing Principle*, Proceedings IEEE International Conference on Consumer Electronics, pages 515–420, 1989.

[2] A.Cassat, *Determination of the Step Motor Performances through Torque and Inductance Computations*, Proceedings 7th Annual Symposium on Incremental Motion Control Systems and Devices, B.C.Kuo (editor), pages 261–277, 1978.

[3] A.Cassat, M.Jufer, *Effect on the Damping Circuits due to Eddy Current Losses on the Dynamic Characteristics of PM Stepping Motors*, Proceedings 13th Annual Symposium on Incremental Motion Control Systems and Devices, B.C.Kuo (editor), pages 251–258, 1984.

[4] A.Cassat, *Brushless DC Motors - Torque and Inductance Determination*, Proceedings 16th Annual Symposium on Incremental Motion Control Systems and Devices, B.C.Kuo (editor), pages 27–37, 1987.

[5] A.Cassat, *Brushless DC Motor - Influence of Changes in Mechanical, Electrical and Magnetic Parameters on Motor Performances*, Proceedings 17th Annual Symposium on Incremental Motion Control Systems and Devices, B.C.Kuo (editor), pages 45–55, 1988.

[6] A.Cassat, *Brushless DC Motor with Axial Airgap - Influence of Changes in Mechanical, Electrical and Magnetic Parameters on Motor Performances*, Proceedings 18th Annual Symposium on Incremental Motion Control Systems and Devices, B.C.Kuo (editor), pages 135–142, 1989.

[7] A.Cassat, J.Dunfield, *Brushless DC Motor: Permanent Magnet Magnetisation and its Effect on Motor Performances*, Proceedings 20th Annual Symposium on Incremental Motion Control Systems and Devices, B.C.Kuo (editor), pages 64–73, 1991.

[8] R.Colby, *Classification of Inverter Driven Permanent Magnet Synchronous Motors*, Conference Record of the 1988 IEEE Industry Applications Society Annual Meeting, Part 1, pages 1–6, 1988.

[9] J. van Diepen, *Modelling and Control of Permanent Magnet Brushless DC Motortypes*, Literature survey, Report number S–539 Laboratory for measurement and control Technical University Delft, 1991.

[10] A.Draper, *Electrical Machines*, Longmans, Green and Co LTD London, Electrical Engineering Series, second edition, 1967.

[11] N.Hemati, M.C.Leu, *Accurate Modelling of Brushless DC Motors for High Performance Applications, Part I,* Proceedings 18th Annual Symposium on Incremental Motion Control Systems and Devices, B.C.Kuo (editor), pages 79–88, 1989.

[12] N.Hemati, M.C.Leu, *Accurate Modelling of Brushless DC Motors for High Performance Applications, Part II,* Proceedings 18th Annual Symposium on Incremental Motion Control Systems and Devices, B.C.Kuo (editor), pages 89–96, 1989.

[13] P.Kovacs, *Transient Phenomena in Electrical Machines,* Studies in electrical and electronic engineering 9, Elsevier 1984.

[14] G.Döring, W.Radziwill, *Sensorloser Elektronischer Dreiphasen-Kommutator,* Laborbericht Nr.678, Philips GmbH Forschungslaboratorium Aachen, 1985. (In German).

[15] A.Jack, P.Acarnley, P.Jowett, *The Design of Small High Speed Brushless DC Drives with Precise Speed Stability,* Proceedings IEEE IAS Annual Meeting, pages 500–506, 1988.

[16] M.Jufer, *Gap Permeance and PM-MMF Distribution Analyses,* Proceedings 16th Annual Symposium on Incremental Motion Control Systems and Devices, B.C.Kuo (editor), pages 21–25, 1987.

[17] M.Jufer, R.Osseni, *Brushless DC Motor and Driver Modelling with Iron Losses Effect,* Proceedings 17th Annual Symposium on Incremental Motion Control Systems and Devices, B.C.Kuo (editor), pages 37–44, 1988.

[18] T.Kenjo, S.Nagomori, *Permanent-Magnet and Brushless DC Motors,* Oxford University Press, Monographs in Electrical and Electronic Engineering, no.18, 1985.

[19] R.Müller, *DC Motors for Special Applications,* Proceedings of the third Motorcon Conference, pages 299–309, 1992.

[20] P.Pillay, R.Krishnan, *An Investigation into the Torque Behavior of a Brushless DC Motor Drive,* Proceedings IEEE IAS Annual Meeting, pages 201–208, 1988.

[21] C.Taft, R.Gauthier, *Brushless Motor Torque Speed Curves,* Proceedings 14th Annual Symposium on Incremental Motion Control Systems and Devices, B.C.Kuo (editor), pages 73–89, 1985.

[22] T.Undeland, A.Petterteig, G.Hauknes, A.K.Ådnanes, S.Garberg, *Diode and Thyristor Turn-off Snubbers Simulation by Krean and an easy to use Design Algorithm,* Conference Record of the 1988 IEEE Industry Applications Society Annual Meeting, Part 1, pages 647–654, 1988.

[23] D.White, H.Woodson, *Electomechanical Energy Conversion,* J.Wiley & Sons New York, 1959.

[24] *DC Motors Speed Controls Servo Systems, an Engineering Handbook* Electro-craft Corporation, USA, 1978.

[25] X.Wang, *Wye & Delta Circuit Comparison and Waveform Simulation for Brushless Motors,* Proceedings 18th Annual Symposium on Incremental Motion Control Systems and Devices, B.C.Kuo (editor), pages 115–134, 1989.

[26] *Full-wave Sensorless Drive ICs for Brushless DC Motors* Philips Technical Publication, 1989.

[27] *Brushless DC Motor Drive Circuit* Philips Technical Publication, 1989.

List of Symbols

α	mechanical rotor angle	$[rad]$
β	relative flux density pertubation	$[-]$
ε	position of the rotor versus the stator	$[m]$
δ_0	the nominal airgap	$[m]$
$\delta(x)$	distribution of the airgap expressed in the stator referential frame	$[m]$
η	efficiency	[%]
$\kappa_{mj}(\alpha)$	gradient of the flux linkage between the permanent magnet and phase j	$[Wb/rad]$
λ_j	total flux linkage of phase j	$[Wb]$
λ_d	direct component of the flux linkages	$[Wb]$
λ_q	quadratic component of the flux linkages	$[Wb]$
$\vec{\Lambda}(\vec{I}(t),\alpha)$	flux linkage vector as function of phase currents and mechanical rotor angle	$[Wb]$
$\vec{\Lambda}_m(\alpha)$	vector of total flux linkages	$[Wb]$
$\Lambda_{mj}(\alpha)$	flux linkage between the permanent magnet and phase j	$[Wb]$
μ_0	permeability of vacuum	[H/m]
μ_d	relative permeability of the permanent magnet	[-]
μ_k	relative permeability of the material of an element k	[-]
Φ_j	The airgap flux	$[Wb]$
Θ_j	the MMF in the airgap due to a permanent magnet	$[A]$
Θ_k	internal MMF of the permanent magnet	$[A]$
$\Theta_{\delta j}$	equivalent MMF across the airgap permeance j	$[A]$
$\Theta_{\rho j}$	equivalent MMF across the equivalent permanent magnet permeance j	$[A]$
τ	soft recovery time constant	$[s]$
$\Upsilon_{\delta j}$	airgap permeance j	$[H]$
Υ_k	permeance of element k	$[H]$
$\Upsilon_{\rho j}$	equivalent permanent magnet permeance j	$[H]$
$\omega_e(t)$	electrical rotor speed (angular velocity)	$[rad/s]$
$\omega_m(t) = \frac{d\alpha}{dt}$	mechanical rotor speed (angular velocity)	$[rad/s]$
$\omega_0(t)$	natural frequency of snubber circuit	$[rad/s]$

$A_{a\delta k}$	geometrical surface of the permanent magnet at the level of the airgap	$[m^2]$
$A_j(\varepsilon)$	equivalent airgap surface	$[m^2]$
A_k	area of element k	$[m^2]$
B	flux density of a permanent magnet	$[T]$
B_k	flux density in an element k	$[T]$
$\hat{B}$	peak flux density in the iron	$[T]$
B_{mot}	damping constant of the motor	$[Ns/rad]$
C_{base}	base capacity	$[F]$
C_e	eddy current losses coefficient	$[Nms/T^2kg]$
C_{ij}	coupling factor between branch i and branch j of the equivalent magnetic scheme	$[-]$
C_h	hysteresis losses coefficient	$[Nms/T^2kg]$
C_s	snubber capacity	$[F]$
CT	torque modification coefficient	$[-]$
$e_{fj}(t)$	back-EMF of the iron phase j	$[V]$
$e_j(t)$	back-EMF across phase j	$[V]$
E_p	back-EMF amplitude	$[V]$
$F_k(x-\varepsilon)$	function representing the distribution of the MMF in the airgap	$[-]$
f	frequency	$[Hz]$
F_z	axial force	$[N]$
F_δ	radial force	$[N]$
$G(x)$	function representing the distribution of the airgap	$[-]$
H_k	magnetic field applied to an element k	$[A/m]$
$i_j(t)$	stator current in phase j	$[A]$
$i_d(t)$	direct component of the phase currents	$[A]$
$i_D(t)$	diode current	$[A]$
i_{line}	current applied to the inverter	$[A]$
$i_q(t)$	quadratic component of the phase currents	$[A]$
$I_{line,av}$	the average line current	$[A]$
$i_{Tindex}(t)$	the transistor current	$[A]$
I_o	load current	$[A]$
I_p	current amplitude	$[A]$
I_{rr}	peak reverse recovery current	$[A]$
I_{Trms}	the root mean square value of the transistor current	$[A]$
J	moment of inertia of all rotating masses	$[kgm^2]$
ke	average back-EMF constant of a phase, 0 to peak value	$[Wb]$
KE	average back-EMF constant of the whole motor	$[Wb]$
KT	average torque constant of the motor	$[Wb]$
KT_t	the ratio of the average torque $T_{e,av}$ to the rms value of a transistor current I_{Trms}	$[Wb]$
l	useful length of the motor	$[m]$
l_k	length of element k	$[m]$
L	self inductance of phases when phases are identical	$[H]$

$[L(\alpha)]$	inductance matrix	$[H]$
L_{ij}	mutual inductance between phases i and j $(i \neq j)$	$[H]$
L_{jj}	self inductance of phase j	$[H]$
L_l	stray inductance	$[H]$
m	number of phases	$[-]$
M_f	mass of iron parts	$[kg]$
M	mutual inductance between phases when phases are identical	$[H]$
n	number of pole pairs	$[-]$
n_p	total number of permeances	$[-]$
n'	number of airgap permeances	$[-]$
$n"$	number of permanent magnet permeances	$[-]$
P_e	eddy current losses	$[W]$
P_h	hysteresis losses	$[W]$
Q_{rr}	reverse recovery charge	$[C]$
r_j	stator resistance of phase j	$[\Omega]$
R	resistance of stator phases when phases are identical	$[\Omega]$
R_a	coil surface radius	$[m]$
R_e	equivalent radius of the stator	$[m]$
R_f	equivalent resistance of one iron phase	$[\Omega]$
R_s	snubber resistance	$[\Omega]$
R_{sopt}	optimum value snubber resistance which minimizes v_{Dmax}	$[\Omega]$
R_{base}	base resistance	$[\Omega]$
R_m	motor resistance	$[\Omega]$
s	pertubation width	$[-]$
t	time	$[s]$
t_{rr}	time needed for soft recovery	$[s]$
$T_d(t)$	detent torque	$[Nm]$
$T_e(t)$	electromagnetic torque of the motor	$[Nm]$
$T_{e,av}$	average electromagnetic torque of the motor	$[Nm]$
$T_h(t)$	hysteresis torque	$[Nm]$
$T_L(t)$	load torque	$[Nm]$
T_{rpl}	torque ripple	$[\%]$
v_{C_s}	snubber capacitor voltage	$[V]$
v_D	voltage across the diode	$[V]$
v_d	direct component of the phase voltages	$[V]$
v_{Dmax}	maximum diode voltage	$[V]$
$v_{Cs,max}$	maximum snubber capacitor voltage	$[V]$
$v_j(t)$	motor applied voltage across phase j	$[V]$
$v_q(t)$	quadratic component of the phase voltages	$[V]$
V_d	diode supply voltage	$[V]$
V_s	supply voltage	$[V]$
V_m	motor applied voltage when looking from the outside	$[V]$
$\vec{V}(t)$	motor applied voltage vector	$[V]$
W_{Rs}	energy loss in the snubber resistor	$[W]$
W_{Cs}	energy loss in the snubber capacity	$[W]$
x	position in the stator referential frame	$[m]$

Auteur(s): E.J.A. Konings

Titel: **Modelling of Three Phase Brushless DC Motors**
A Survey of Literature

Kopie naar directie-archieven:

PI Research	WB5	
Nat.Lab.	WB5	
PRL	Redhill, UK	
PL-NAP	Briarcliff Manor, USA	
LEP	Limeil-Brévannes, France	
PFA	Aachen, BRD	
Patent. Dept.	WAH	
Directeur	dr. J.P. Hurault	WB5
Adjunct-directeur	dr. G.E. Thomas	WY7
Groepsleider	ir. B. Sastra	WYp

Kopie volledig rapport naar:

Haasen, R.L.E. van	Nat.Lab.	WY-p
Kamerbeek, E.M.H.	Nat.Lab.	WY-p
Ceton, C.	Nat.Lab.	WY-p
Groos, P.J.M. v.	Nat.Lab.	WY-p
Konings, E.J.A.	Nat.Lab.	WY-p
Sperling, F.B.	Nat.Lab.	WY-p
Steinbuch, M.	Nat.Lab.	WY-p
Wortelboer, P.M.R.	Nat.Lab.	WY-p
Bosgra, O.H. (6 ex.)	T.U.-Delft	Mekelweg 2 2628 CD Delft
Huisman, H.	T.U.-Delft	Mekelweg 2 2628 CD Delft